Resonantly Assisted Silicon Photonics Transceivers for Medium-Reach Interconnects

Von der Fakultät für Elektrotechnik und Informationstechnik der Rheinisch-Westfälischen Technischen Hochschule Aachen zur Erlangung des akademischen Grades einer Doktorin der Ingenieurwissenschaften genehmigte Dissertation

vorgelegt von

Jovana Nojić M.Sc.
aus Sarajevo, Bosnien und Herzegowina

Berichter
Univ.-Professor Dr. Jeremy Witzens, Ph. D.
Univ.-Professorin Dr.-Ing. Marina Petrova

Tag der mündlichen Prüfung: 24.03.2022

To my family

Abstract

Motivation, Goal and Task of the Dissertation

Mobile data traffic is on a constant rise, with emerging 5G technologies having to service a broad range of applications that require high throughput, low latency, and high reliability communication. Fiber optic links, based on standard single mode fibers (SMF), are one of the main candidates for transporting data from 5G cell sites to central offices, and further to remote data centers. To reduce infrastructure costs, silicon photonics (SiP) presents itself as the technology of choice for the necessary electro-optical transceivers, with its low per-unit cost for high-volume production, owing to its large degree of compatibility with the well-established complementary metal oxide semiconductor (CMOS) fabrication. Moreover, low power, frequency selective resonantly assisted SiP devices ease the implementation of multi-channel, wavelength division multiplexed (WDM) transceiver systems that increase parallelization. Furthermore, to meet the growing demands for data throughput, flexible, robust modulation schemes that rely on inexpensive direct detection (DD) are of great interest. The single-sideband orthogonal frequency multiplexing (SSB-OFDM), with its high tolerance to dispersion-mediated signal distortion, flexibility in spectral loading, and high spectral efficiency fits well the stated requirements. In that context, we investigate the feasibility and performance of SSB-OFDM links that rely on SiP ring resonator assisted modulation, while carefully taking other typical link components (lasers and amplifiers) into consideration. On the receiver side, we study a SiP WDM receiver system based on optical add-drop multiplexers (OADM) that handles polarization scrambling present in SMF data links.

Major Scientific Contributions

In this work, we present, to the best of our knowledge, for the first time a detailed analytical model for the laser phase noise to intensity noise conversion in resonant ring modulator (RRM) assisted DD data transmission. To validate the model, we perform a set of SSB-OFDM transmission experiments using a SiP RRM assisted mod-

ulator. Moreover, we numerically model the same link, including all imperfections associated with individual link components, with the laser phase noise introduced at the link end through the derived analytical expressions. Excellent agreement of experimental and modeling results confirms the validity of our analytical model. Additionally, we study how the optimal biasing point of the RRMs depends on the laser source characteristics, as well as the influence of component nonlinearities on the SSB signal. Lastly, we present a high-speed 10-channel polarization-diverse SiP WDM receiver with a reduced number of OADMs per channel and balanced group delays for orthogonal polarization states and experimentally benchmark the performance of each of the receiver channels.

Acknowledgments

First of all, I would like to thank my supervisor Prof. Jeremy Witzens for the opportunity to do research at IPH, for sharing his invaluable scientific insights and practical, systematic approach to solving complex problems, and, most of all, for his unwavering support on all fronts.

I would also like to extend my gratitude to:

Doro Pawelzick, for being the glue that keeps the institute together, for her care, support and advice.

Anne Schröder, for her help with administrative issues, patience and kindness.

Heijo Ehlen, for resisting the urge to hide every time I showed up at his door with the strangest IT issues, and solving them promptly and with a laugh.

Florian Merget, for all the pro tips and tricks, and introducing me to new musical gems.

Alvaro Moscoso-Martir, for his encouragement and levelheadedness in moments of crisis.

Saeed Sharif Azadeh, for countless discussions and his infectious excitement about science.

Johannes Hauck, for showing by example that a sense of magic and rigor are equally important and essential when doing research.

Jens Richter, for introducing me to priceless tools for data and time management (time-turner always comes in handy).

Bin Shen, for his help in the lab, his calm and precise manner, and that invaluable extra dB.

Ibrahim Ghannam, for his readiness to share valuable resources, be it computational or delicious ones.

Alireza Tabatabaei Mashayekh, for bringing song into the lab and always keeping things under control.

Andrea Zazzi, for ego-boosting morning greetings and always being ready to lend a helping hand.

Manuel Ackermann, for being a great travel buddy and always open for discussion.

Dominik Schoofs, for doing a great job in his Master thesis work and helping with the measurements of the receiver systems.

Juliana Müller, for making me feel welcome from the get-go, her openness, kindness, understanding, and surprise warm cookies in cold winter evenings.

Bahareh Marzban, my partner in "crime", for being there for all the ups and downs, for all the laughs and new perspectives during our lengthy discussions that span all the imaginable topics (plus some unimaginable ones).

To all other IPH members, past and present, for helping make the institute a great place to learn and grow.

Also, a big thanks to Bahareh, Juliana, Bin, Andrea, Ibrahim and Manuel for proof-reading this manuscript.

To Marija Trajković, for being the best life companion a person could ask for.

Last, yet quite the opposite of least, I am immensely grateful to my family for their love. To my mom Stana and sisters Jelena and Gaga, for being perfect role models and tolerating my propensity for drama. To my husband Miloš, for his immeasurable patience and support in this challenging journey.

List of Abbreviations

5G	fifth generation mobile
AC	alternating current
ADC	analog-to-digital converter
ADSL	asymmetric digital subscriber line
ASE	amplified spontaneous emission
BER	bit error ratio
BtB	back-to-back
CMOS	complementary metal-oxide semiconductor
CO-OFDM	coherent optical orthogonal frequency division multiplexing
CPO	co-packaged optics
CP	cyclic prefix
DAB/DVB	digital audio/video broadcasting
DAC	digital-to-analog converter
DCF	dispersion compensating fiber
DC	direct current
DD	direct detection
DFB	distributed feedback
(I)DFT	(inverse) discrete Fourier transform
DMT	discrete multi-tone
ECL	external cavity laser
EDC	electronic dispersion compensation
EDFA	erbium doped fiber amplifier
EO	electro-optical
ER	extinction ratio
EVM	error vector magnitude
(I)FFT	(inverse) fast Fourier transform

FSR	free spectral range
FWHM	full width half maximum
FWM	four-wave mixing
GC	grating coupler
GSG	ground-signal-ground
HD-FEC	hard-decision forward error correction
I/O	input/output
ICI	inter-carrier interference
IL	insertion loss
IoT	internet-of-things
ISI	inter-symbol interference
LE	lumped element
LSB	lower frequency sideband
LTE	long-term evolution
M2M	machine-to-machine
MCM	multi-carrier modulation
MLL	mode-locked laser
MMF	multi-mode fiber
MMI	multi-mode interferometer
MPW	multi-project wafer
NRZ	non-return-to-zero
OADM	optical add-drop multiplexer
OBPF	optical band-pass filter
ODL	optical delay line
OFDM	orthogonal frequency division multiplexing
OMA	optical modulation amplitude
OOK	on-off keying
P/S	parallel-to-serial
PAPR	peak-to-average power ratio
PCB	printed circuit board
PDGC	polarization-diverse grating coupler
PD	photodetector
PIC	photonic integrated circuit
PNA	programmable network analyzer
PPG	programmable pattern generator
PRBS	pseudo-random bit sequence

PSD	power spectral density
PSR	polarization splitter-rotator
QAM	quadrature amplitude modulation
QPSK	quadrature phase shift keying
RA-MZI	resonantly assisted Mach-Zehnder interferometer
RA-SSB	resonantly assisted single-sideband
RF	radio frequency
RIN	relative intensity noise
RoF	radio-over-fiber
RRM	resonant ring modulator
RX	receiver
SiP	Silicon Photonics
SNR	signal-to-noise ratio
SOA	semiconductor optical amplifier
SSB	single-sideband
SSR	sideband suppression ratio
TE	transverse electric
TiN	titanium-nitride
TM	transverse magnetic
TW	traveling-wave
USB	upper frequency sideband
WDM	wavelength division multiplexing
WLAN	wireless local area network

Contents

Abstract **i**

Acknowledgments **iii**

List of Abbreviations **v**

1 Motivation and prior work **1**

2 Ring assisted single-sideband modulator **5**
2.1 Theoretical introduction 5
2.1.1 OFDM basics 5
2.1.2 Modulation in Silicon 11
2.1.3 Resonant ring modulators 12
2.2 Experimental results 20
2.2.1 Passive characterization 21
2.2.2 DC characterization 23
2.2.3 High-speed characterization 25
2.2.4 RA-SSB modulator 26

3 Laser Phase Noise in Ring Resonator Assisted Direct Detection Data Transmission **29**
3.1 Introduction 29
3.2 Analytical model of phase to intensity noise conversion 30
3.3 Link transmission: measurements and modeling 38
3.3.1 Measurement setup 38
3.3.2 Measurement and data post-processing methodology 41
3.3.3 Link model 46
3.3.4 Results and discussion 54
3.4 Summary 60

4 Full capacity measurements **61**
4.1 Results 61
4.2 Sideband suppression 65
4.3 Summary 71

5 Polarization diverse WDM receiver with a reduced number of OADMs **73**
5.1 Introduction 73
5.2 Component characterization 75
5.2.1 Ge waveguide photodiode 75
5.2.2 Optical add-drop multiplexers 76
5.3 System measurements 79
5.4 Summary 82

6 Conclusions and Outlook **83**

A More on derivation of Equations 3.12 and 3.13 **87**

Bibliography **91**
List of publications 100

Chapter 1

Motivation and prior work

According to last year's (2020) Cisco annual internet report [1], by 2023 over 70% of the global population will have mobile connectivity, with over 10% of all devices and connections being serviced by the fifth generation (5G) mobile technologies. Among the different categories, the fastest growing one will be mobile machine-to-machine (M2M) communication, followed by smartphones. At the same time, the 5G speed will sky-rocket, reaching up to 575 Mb/s, a level 13 times higher than the average mobile speed. In order to support a broad range of applications, from bandwidth-hungry high-quality video streaming and large-scale M2M communication between the devices that make up the internet-of-things (IoT), to mission-critical applications such as autonomous vehicles and telemedicine, 5G technologies will have to meet very stringent requirements of high throughput, low latency, and ultra-high reliability. Although the term "5G" is most commonly used in relation to mobile and wireless networks, fiber optic links will continue to play a crucial role as the backbone of the data-transport network. Due to its unprecedented bandwidth, fiber is being considered as a solution not only for mobile backhaul, which connects central offices to the core network and remote datacenters, but also for the fronthaul segment of the mobile network, connecting central offices to the 5G cell sites. It is also expected that 5G will push fiber optics closer to homes in Europe and North America, where currently only 15% of them are connected to fiber [2]. The infrastructure costs will therefore be shared between these two technologies, addressing the issue often raised in relation to use of fiber in 5G, given that other technological solutions such as millimeter-microwave and free space optic links come at a lower infrastructure price [3].

The 5G networks will therefore require a vast number of electro-optical (EO) transceivers to keep the nodes of the network running [4]. Silicon Photonics (SiP) emerges as a natural candidate for the underlying transceiver technology. Due to its large compatibility with complementary metal-oxide semiconductor (CMOS) pro-

cesses, it can leverage the mature fabrication facilities perfected over the past decades by the electronics industry, to offer high-yield, low-cost, high-volume production of photonic integrated circuits (PICs). The high index contrast of the platform enables high on-chip density of devices which, among others, include high-speed modulators [5, 6], high-speed and high-responsivity germanium (Ge) photodiodes [7, 8], splitters, combiners, de-/multiplexers [9, 10], filters [11–13], polarization-handling components [14–18], enabling thereby a wide variety of functionalities. However, the optical source remains a puzzle piece missing in SiP due to Silicon's indirect bandgap, which hinders efficient lasing in the material. Nevertheless, great progress has been made in integrating other material systems into the SiP platform to achieve lasing, either by bonding or selectively growing III-V materials on Si [19–21], or by exploring group IV materials which can more readily be introduced into the CMOS flow [22, 23]. Moreover, with increasing bandwidths and growing concerns of power management, transceiver trends are moving toward co-packaged optics (CPO) [24], where electronic switching circuitry and optics are brought into the same package. With a larger wafer size compared to alternative integration platforms, SiP enables 2.5D and 3D integration of electronic ICs and PICs, thus making use of modern packaging which only exists at the 300 mm wafer level [25]. All these ingredients in turn allow for fabrication of compact, high-speed transceiver systems.

Furthermore, to efficiently exploit the wide bandwidth of the optical fiber, wavelength division multiplexing (WDM) has been widely employed in optical communications. In WDM, multiple optical carriers at different wavelengths are used for parallel transmission of multiple high-speed signals. Frequency selective, integrated resonant devices can address individual channels discriminately and are therefore easily assembled into WDM systems. More specifically, in the transmitter, resonant ring modulators (RRMs) can simultaneously perform multiplexing and modulating tasks. Their small footprint and low power consumption allow for realization of compact, energy efficient, high-speed multi-channel systems [26–34]. For these reasons, they remain in the focus of both researchers and industrial players.

Apart from the modulator type, other equally important, closely linked decisions must be made when designing an optical link. These are the modulation format and the detection scheme of choice. Adaptable, scalable and robust modulation schemes that rely on inexpensive direct detection (DD) are of great importance for flexible, future-proof standards and networks that can follow the trends of growing throughput.

Orthogonal frequency division multiplexing (OFDM) uses a set of spectrally overlapping, but orthogonal frequency sub-carriers for data transmission. It is a spectrally efficient modulation format, that offers adaptive spectral loading tailored specifically to the frequency characteristics of the channel [35]. Algorithms for optimal spectrum

allocation have been developed and widely employed, both for the radio frequency (RF) [36] and optical communications [37, 38]. OFDM intrinsically incorporates electronic dispersion compensation (EDC) into its implementation [39], representing an effective and scalable solution to inter-symbol interference (ISI) caused by the dispersive channel. In contrast, for conventional serial modulation schemes, such as non-return to zero (NRZ) or quadrature amplitude modulation (QAM), the complexity of time domain based equalization schemes rises rapidly with the increasing signaling speeds [35, 40]. Since its initial formulation [41] and subsequent refinements in 1960s and 70s, OFDM has become a standard in many of today's RF networks, such as wireless local area networks (WLAN), asymmetric digital subscriber line (ADSL), digital audio and video broadcasting (DAB and DVB), and long-term evolution (LTE). Nonetheless, it wasn't until early 2000s that it started being considered for use in optical communications, initially in multi-mode fiber (MMF) links to combat modal dispersion [38, 42]. Since then it has been utilized in optical wireless [43], plastic fiber [44, 45], and SMF links [46], also employing SiP integrated components [47–49]. Among its many variants, the single sideband OFDM (SSB-OFDM) relies on direct detection, thus meeting well the above-stated modulation scheme requirements [50]. Recently, SiP based SSB modulation solutions have also been proposed for 5G optical access networks [51–53], including millimeter-wave radio over fiber (RoF) applications [54].

In this work, we aim to combine the RRM-based WDM parallelization with the SSB-OFDM technique to simultaneously boost throughput and reach in our system. To this end, we study the performance of a three-channel, resonantly assisted single sideband modulator (RA-SSB), fabricated in SiP integrated platform, in back-to-back (BtB) and fiber transmission.

Moreover, resonant integrated devices also have a role in the direct detection WDM receivers. Here, they are utilized as wavelength-specific filters for channel dropping. The optical add-drop multiplexers (OADMs) are the first order filters, which comprise of a single resonant structure. In our study, we look at the performance of a ten-channel, integrated SiP WDM receiver, which relies on resonant OADMs for filtering. In this receiver, we employ a novel approach to enable polarization insensitive detection of intensity modulated, high-speed signals.

Outline of this work

This thesis is structured as follows:

- Chapter 2 first introduces the most important theoretical concepts related to OFDM and modulation in SiP, with the focus on RRMs. It then discusses experimental characterization of the RRMs and thermal tuners that comprise the RA-SSB modulator system.

- Chapter 3 represents the core of this thesis. It deals with a phenomenon occurring in resonant devices when the optical signal at the input has phase noise, namely the conversion of phase to intensity noise by the resonator. We explore in great detail the statistical and spectral properties of this noise source, presenting for the first time, to the best of our knowledge, their full analytical descriptions. We run two sets of experiments with two optical sources that differ in their noise performance, in order to test our analytical predictions. In the experiments, the SSB-OFDM data is modulated onto the optical carrier by an integrated SiP RA-SSB. The full link is also modeled numerically, where the phase to intensity noise conversion is introduced through the analytical expressions. Direct comparison of experimental and modeled data then offers an insight into the validity of the analytical model.

- Sinusoidal [55] and single-channel data transmission [56] have already been demonstrated using an RA-SSB modulator implemented in SiP platform. In Chapter 4, we expand on that by pushing the performance of a three-channel RA-SSB integrated modulator system to its full capacity. Here, we define it as the maximum throughput of each channel that allows for transmission of data over up to 20 km of SMF with the bit error ratio below the 20% hard-decision forward error correction limit. We also study how different component nonlinearities and other non-idealities of the system influence the suppression of the unused sideband, and through that, the achievable spectral efficiency in multi-channel transmission.

- Chapter 5 describes our novel approach to handling polarization scrambling at the multi-channel receiver system, based on double-sided OADMs, double-sided integrated waveguide Ge photodiodes and integrated optical delay lines. System components are described and characterized, followed by the dual-polarization high-speed data detection by the ten-channel integrated receiver system.

- Finally, in Chapter 6 we summarize the most important conclusions of our study and give a short outlook for the future work.

Chapter 2

Ring assisted single-sideband modulator

In this chapter we first present theoretical foundations of OFDM and modulation using RRMs in SiP integrated platform (Section 2.1). We then show the experimental device-level characterization results of the integrated three-channel RA-SSB modulator system (Section 2.2).

2.1 Theoretical introduction

2.1.1 OFDM basics

Orthogonal frequency division multiplexing (OFDM) is a multi-carrier modulation (MCM) technique which uses a set of lower rate, mutually overlapping, yet orthogonal frequency sub-carriers for data transmission. Unlike in other MCM schemes where substantial spectral overhead is required to enable cross-talk-free filtering and detection of individual carriers at the receiver, the orthogonality condition of OFDM allows for a tighter carrier packing and better use of the available spectrum (Figure 2.1).

To compose an OFDM signal, we start from a stream of information symbols. Generally speaking, these symbols are complex numbers that correspond to constellation points of different modulation formats. They can, therefore, in themselves carry more than two bits of information. The initial stream is then split into N parallel streams, each of which modulates a separate frequency sub-carrier. Therefore, the symbol rate is reduced N times compared to the initial value.

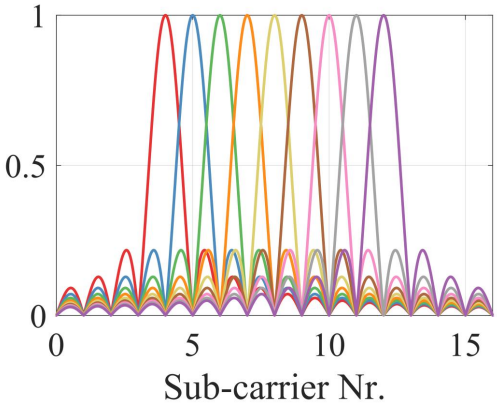

Figure 2.1: OFDM signal spectrum. Each color represents the spectral shape of another sub-carrier.

Mathematically, the OFDM signal can be described as [35]

$$s(t) = \sum_{i=-\infty}^{+\infty} \sum_{k=0}^{N-1} c_{ki} s_k(t - iT_s) \tag{2.1}$$

$$s_k(t) = \Pi(t) e^{i2\pi f_k t} \tag{2.2}$$

$$\Pi(t) = \begin{cases} 1, & 0 \le t \le T_s \\ 0, & \text{otherwise.} \end{cases} \tag{2.3}$$

Here, c_{ki} is the i-th information symbol at the k-th sub-carrier, $s_k(t)$ is the waveform of the k-th sub-carrier, N is the number of sub-carriers, f_k is the frequency of the k-th sub-carrier, $\Pi(t)$ is the pulse shaping function, and T_s is the symbol duration. In this notation, i signifies the counter for OFDM symbols.

For optimal detection of the sub-carriers, a correlator matched to each sub-carrier can be employed at the receiver. In this case, a received OFDM symbol at the correlator output is given by

$$c'_{ki} = \frac{1}{T_s} \int_0^{T_s} r(t - iT_s) s_k^* dt = \frac{1}{T_s} \int_0^{T_s} r(t - iT_s) e^{-i2\pi f_k t} dt, \tag{2.4}$$

where $r(t)$ is the received time-domain signal. The correlation between two sub-carriers is further given as

$$\delta_{kl} = \frac{1}{T_s} \int_0^{T_s} s_k s_l^* \, dt = \frac{1}{T_s} \int_0^{T_s} exp\big(i2\pi(f_k - f_l)t\big) dt = e^{i\pi(f_k - f_l)} \frac{sin\big(\pi(f_k - f_l)T_s\big)}{\pi(f_k - f_l)T_s}. \tag{2.5}$$

From this, it simply follows that the orthogonality condition is fulfilled if the following relationship holds

$$f_k - f_l = p\frac{1}{T_s}, \tag{2.6}$$

where p is an integer, i.e. if the sub-carrier frequency spacing corresponds to the inverse of the symbol duration.

Furthermore, if we focus on a single symbol of the OFDM signal and assume we sample it at every time interval of T_s/N, the m-th signal sample can be written as

$$s_m = \sum_{k=1}^{N} c_k e^{i2\pi f_k \frac{(m-1)T_s}{N}}. \tag{2.7}$$

Based on the orthogonality condition and a convention

$$f_k = \frac{k-1}{T_s}, \tag{2.8}$$

this can further be written as

$$s_m = \sum_{k=1}^{N} c_k e^{i2\pi f_k \frac{(m-1)T_s}{N}} = \sum_{k=1}^{N} c_k e^{i2\pi \frac{(k-1)(m-1)}{T_s}} = \mathscr{F}^{-1}\{c_k\}, \tag{2.9}$$

where $\mathscr{F}^{-1}$ represents the inverse discrete Fourier transform. Similarly, at the receiver end, the k-th received information symbol ($c_k^{'}$) can be written as

$$c_k^{'} = \mathscr{F}\{r_k\}, \tag{2.10}$$

where r_k are samples of the received signal, sampled at every interval T_s/N.

The mathematical formulation of the OFDM signal, therefore, has a form of the inverse discrete Fourier transform (IDFT) of the information symbols. Correspondingly, at the receiver the information symbols can be retrieved by calculating the discrete Fourier transform (DFT) of the sampled received signal. With the development of the fast Fourier transform (FFT) algorithm, the generation and detection of OFDM symbols has been hugely simplified and accelerated. More notably, the complex and demanding task of creating and isolating a large number of tightly stacked sub-carriers was lifted from the collections of analog oscillators and filters used in other MCM schemes, and moved to the more flexible and easily scalable digital domain. The compact nature of the OFDM spectrum enables minimal spacing between channels in WDM transmission, increasing the overall spectral efficiency.

The general schemes for OFDM signal generation and detection are shown in Figure 2.2(a) and (b), respectively. At the transmitting end, the input bit stream is first mapped onto complex information symbols of quadrature phase shift keying (QPSK) or QAM constellations. A group of N symbols, each one acting as a scaling factor to the corresponding frequency sub-carrier, is further sent to the the inverse FFT (IFFT) block of size N. The complex values at the IFFT output correspond to the time samples of the OFDM signal.

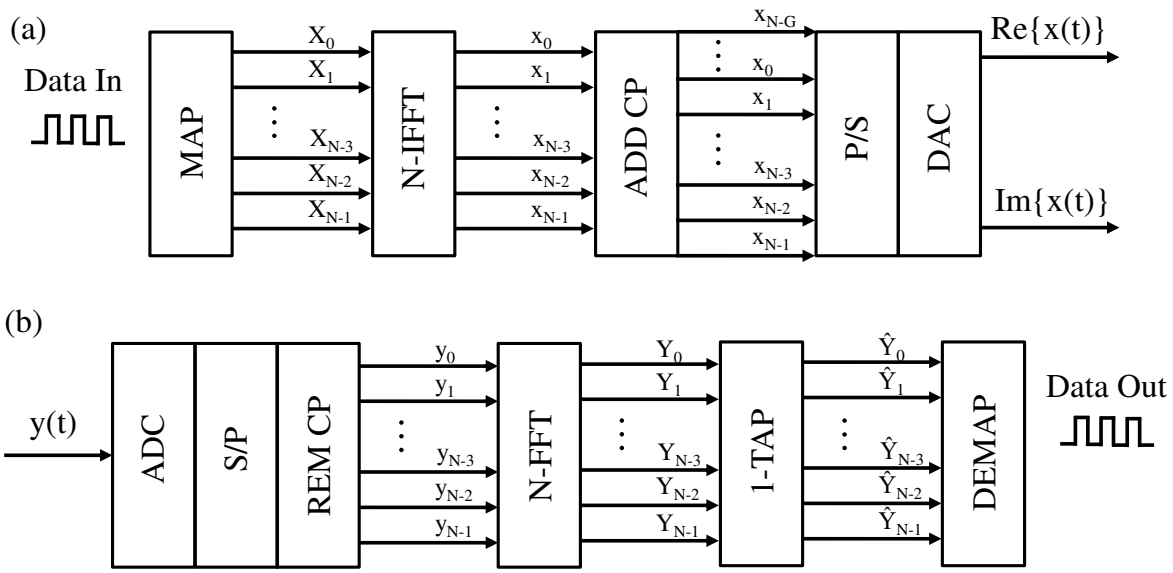

Figure 2.2: Block diagram of OFDM signal (a) generation and (b) demodulation.

Even though the duration of the individual OFDM symbols is much longer than, for example, the NRZ symbols of the same aggregate bit rate, some residual inter-carrier (ICI) and inter-symbol interference (ISI) can still affect the signal after its propagation through a dispersive fiber channel. In OFDM, this issue is handled by the introduction of a guard interval, called cyclic prefix (CP). To better illustrate the idea behind the CP implementation, we take a look at how the dispersive channel, modeled by a time spread t_d, affects two different sub-carriers (SC1 and SC2) in two consecutive OFDM symbols (Figure 2.3). At the transmitter, the sub-carriers are aligned and orthogonal to one another during one DFT observational period (Figure 2.3(a)). Upon propagation, however, due to a slower speed of SC1, the sub-carriers get misaligned and the orthogonality is lost, causing ICI (Figure 2.3(b)). Moreover, SC1 corresponding to one symbol enters the observational period of the other symbol causing ISI. To prevent this from happening, each symbol is extended for the time interval Δ_G, and a snippet of the symbol in duration of Δ_G from the trailing edge - blue fragment for the first symbol, green one for the second - is inserted before the symbol's leading edge (i.e. before the start of the original symbol, Figure 2.3(c)). If the dispersive spread is less than the guard interval ($t_d < \Delta_G$), by a suitable choice of the DFT observational window the orthogonality of the sub-carriers is preserved (Figure 2.3(d)). What remains is a linear phase shift introduced to each sub-carrier by the dispersive channel, which can be readily compensated for through proper channel estimation. The real part of an OFDM symbol is shown in Figure 2.4, with the CP marked in blue. The introduction of CP, on the other hand, lowers the overall throughput and widens the OFDM spectrum, requiring also a larger channel sepa-

ration in WDM transmission. This is illustrated in Figure 2.5, on the example of an SSB-OFDM signal with a 3% CP.

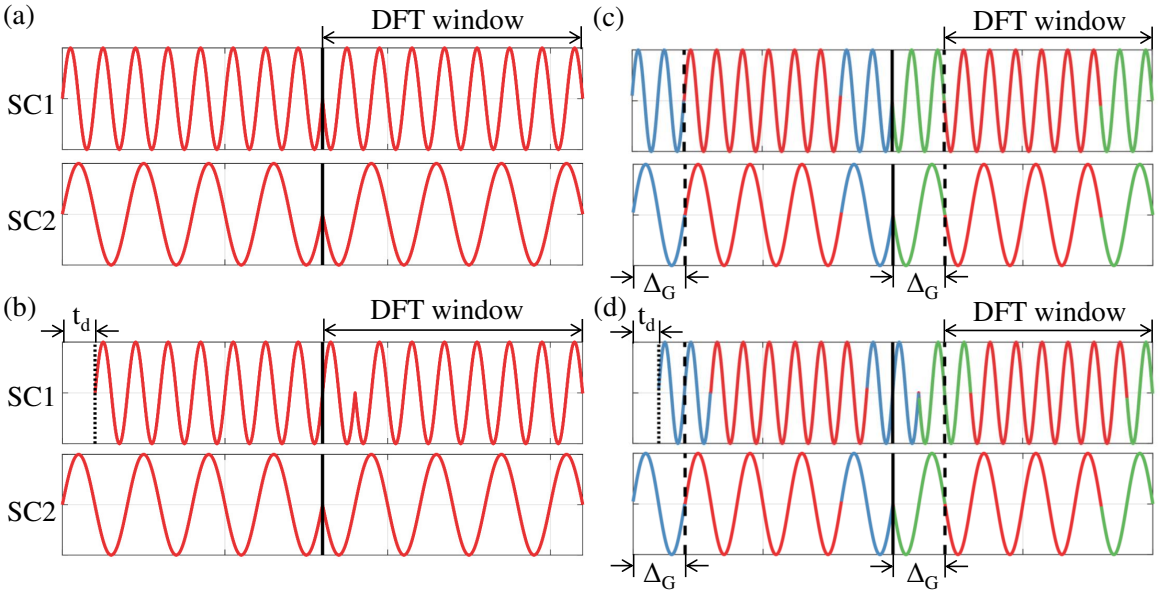

Figure 2.3: OFDM symbols (a) at the transmitter without the cyclic prefix; (b) after propagation without the cyclic prefix; (c) at the transmitter with the cyclic prefix; (d) after propagation with the cyclic prefix. In (c) and (d) blue/green fragment from the trailing edge of SC1/SC2 is inserted before its trailing edge as a cyclic prefix.

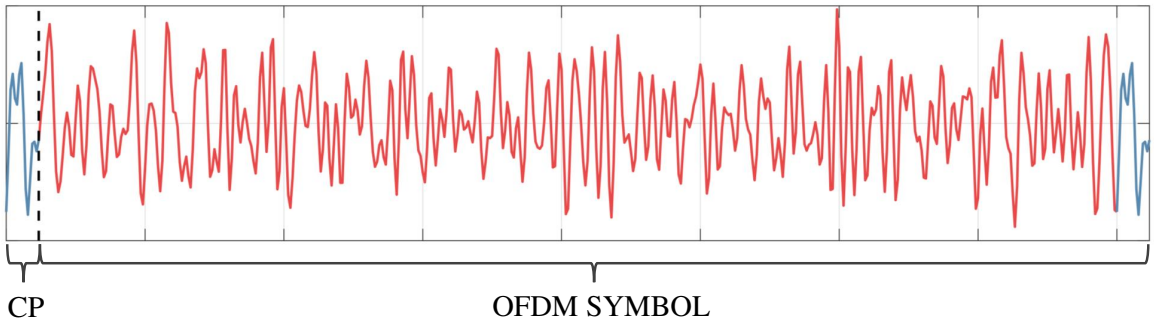

Figure 2.4: Time domain OFDM symbol with an appended CP.

Let us now continue with further steps of OFDM signal generation (Figure 2.2(a)). After the CP insertion, the time domain symbols are sent to a parallel-to-serial (P/S) unit and further to the digital-to-analog (DAC) converter.

At the receiver, the complementary steps are performed in the reverse order: the signal is sampled by an analog-to-digital (ADC) converter, serialized, the CP is removed and an FFT is performed on the remaining samples (Figure 2.2(b)). Based on the training sequence transmission and channel estimation, the channel trans-

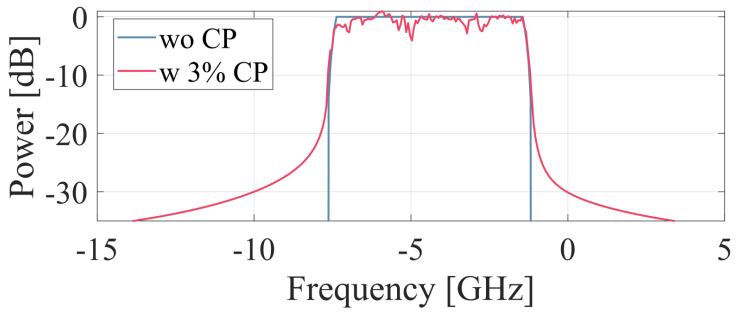

Figure 2.5: Influence of the insertion of CP on the signal spectral width on the example of the SSB-OFDM signal.

fer function is recorded and further utilized for single-tap (1-tap) equalization, the next block in the detection sequence. This operation is a single complex number division, which in effect re-scales and rotates the information symbols on individual sub-carriers to remove the effects of the channel. Lastly, the complex symbols are remapped onto the final bit sequence.

In the single-sideband OFDM, SSB-OFDM, only half of the sub-carriers, corresponding to one of the frequency sidebands, is loaded with data. This variant relies on direct detection, which reduces the complexity of the receiver and relaxes the performance requirements for the optical source, when compared to the coherent optical OFDM (CO-OFDM) transmission. It also offers improved tolerance to channel dispersion relative to other DD-OFDM schemes, such as digital multi-tone (DMT). Namely, when high-speed, high-bandwidth signals are transmitted through a dispersive medium, lower and upper frequency sidebands accumulate different phase shifts. This can lead to frequency fading upon direct detection, where signal is completely suppressed at certain frequencies, determined by the overall dispersive spread [40]. The SSB-OFDM signal can be generated in the optical domain either by filtering out the undesired sideband, by using an intermediate RF carrier to offset the signal relative to the optical carrier, or as in our case, by employing an IQ modulator [50]. In such a scheme, real and imaginary parts of the OFDM signal form a Hilbert pair. The real part is then applied to the I-arm and the imaginary part to the Q-arm, thus forming a single-sideband signal at the modulator output.

The main disadvantages of OFDM include high peak-to-average power ratio (PAPR) and its sensitivity to frequency and phase noise. Extensive research is being done on these topics, where, for example, the first challenge is being tackled by the implementation of signal clipping techniques [57].

2.1.2 Modulation in Silicon

Modulation in SiP platform relies on the plasma dispersion effect, the change of the refractive index (n) of the material with electrical carrier concentration. At the same time, the imaginary part of the complex refractive index (n_i) changes, as dictated by Kramers-Kronig material relations. This in turn causes a change of the absorption coefficient α, related to n_i at a given wavelength λ as $\alpha = 4\pi/\lambda \cdot n_i$. These dependencies for Si are [58]

$$\Delta n = -8.8 \times 10^{-22} \Delta N - 8.5 \times 10^{-18} \Delta P^{0.8} \tag{2.11}$$

$$\Delta \alpha = 8.5 \times 10^{-18} \Delta N + 6 \times 10^{-18} \Delta P [cm^{-1}], \tag{2.12}$$

where ΔN and ΔP are the electron and hole densities, respectively.

Refractive index of Si also has a strong temperature dependence, with a thermo-optic coefficient at 1.5 µm of $dn/dT = 1.87 \cdot 10^{-4} K^{-1}$ [59]. However, this effect is slow and is therefore more commonly used for control purposes, rather than in high-speed modulation.

Phase shifters in SiP platform are formed by embedding a PN junction inside of a waveguide, typically in a form of a rib structure to allow for electrical contacting. Carrier distribution is shown in Figure 2.6(a) for two different voltages applied to the diode. With the voltage change, carriers redistribute and the effective index of the waveguide mode changes, leading to phase modulation. This is followed by a small amplitude modulation, due to the simultaneous change in the absorption. Normalized E-field magnitude of the optical waveguide mode is shown Figure 2.6(b). Here, the mode profile is asymmetric because we are considering a bent waveguide, relevant for our later discussion about RRMs.

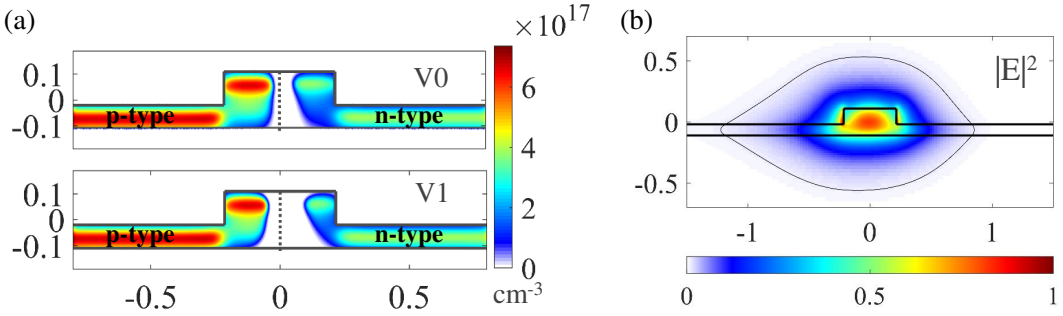

Figure 2.6: (a) Electrical carrier distribution in an Si rib waveguide for two different applied voltages. (b) Normalized E-field magnitude of the optical mode in a bent Si rib waveguide.

High speed operation up to 50 Gb/s has been demonstrated [60, 61] for modulators that work in the forward biased regime. However, to achieve this, complex

pre-emphasis schemes are required. Therefore, depletion-based devices operated in reverse bias remain the most prominent both in research and commercial applications due to higher achievable speeds [5, 6, 62]. Although the trends in high-speed integrated modulators in SiP platform are moving towards the hybrid integration of materials that exhibit a strong Pockel's effect [5, 63], pure Si modulators remain an attractive field of research due to their compatibility with the existing CMOS technology.

2.1.3 Resonant ring modulators

Steady-state model

RRMs are formed by evanescently coupling a waveguide loop with an embedded PN junction to one or two bus waveguides, depending on whether they are used in an all-pass or add-drop configuration, respectively. The add-drop ring resonator topology is shown in Figure 2.7(a). Here, "1" in the bottom left corner marks the input port, where a unit-amplitude optical signal is incident to the structure. Steady-state expressions for the field transmission coefficients at the through (THRU) and drop (DROP) ports of the depicted resonator are

$$T_{THRU} = \frac{t_1 - t_2 A e^{-i\beta L}}{1 - t_1 t_2 A e^{-i\beta L}}, \tag{2.13}$$

$$T_{DROP} = -\frac{\kappa_1 \kappa_2 \sqrt{A} e^{-i\beta L/2}}{1 - t_1 t_2 A e^{-i\beta L}}. \tag{2.14}$$

Here, t_1 and κ_1 are electric field transmission and coupling coefficients between the THRU waveguide and the ring. Similarly, t_2 and κ_2 represent field transmission and coupling coefficients between the ring and DROP waveguide. For lossless directional couplers relationship $|t_i|^2 + |\kappa_i|^2 = 1$ holds. β is the propagation constant, related to the effective index (n_{eff}) of the mode propagating in the ring at wavelength λ as

$$\beta = \frac{2\pi}{\lambda} n_{eff}. \tag{2.15}$$

Furthermore, field attenuation due to the ring's intrinsic losses (free carrier absorption, scattering and bending losses) after a single round-trip is given by

$$A = e^{-\alpha/2 \cdot L}, \tag{2.16}$$

where α is the modal power loss in units of $1/m$ and R is the radius of the ring, with the circumference of $L = 2\pi R$.

At certain wavelengths, the optical signal accumulates a phase shift equal to 2π (or its multiples) during a round-trip in the ring. This signal then interferes de-

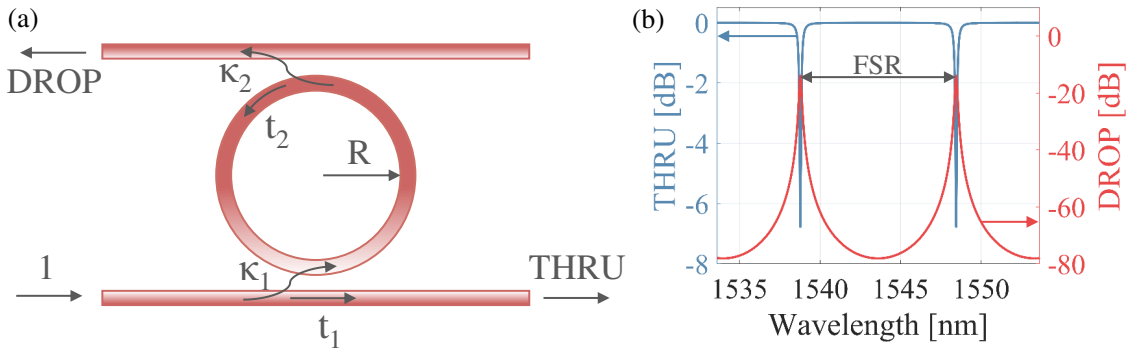

Figure 2.7: (a) Add-drop resonator structure; (b) spectra at the THRU (in blue, left axis) and DROP (in red, right axis) ports.

structively with the light in the THRU waveguide, forming intensity drops (i.e. resonances) in the spectrum at the THRU port (Figure 2.7(b)). These wavelengths fulfill the resonance condition, given as

$$\frac{n_{eff}L}{\lambda_0} = m, \tag{2.17}$$

where m is an integer.

On the other hand, light intensity builds up in the ring through constructive interference when the resonant condition holds. Therefore, the DROP spectrum exhibits peaks at the resonant wavelengths.

The resonator supports a multitude of resonances. The spectral separation between the two adjacent resonant wavelengths is called the free spectral range (FSR) and is given by

$$FSR = \frac{\lambda_0^2}{L \cdot n_g}, \tag{2.18}$$

with L the ring circumference, and $n_g = n_{eff} - \lambda \cdot \frac{dn_{eff}}{d\lambda}$ the group index of the propagating mode. In WDM systems, the FSR along with the channel spacing determines how many wavelengths can be used in parallel.

Coupling regime

Depending on the relationship between the coupling and intrinsic losses of the ring, we differentiate between the under-coupled, over-coupled and the critically coupled regime of the resonator.

In the critically coupled case, the power at the THRU port is completely extinguished and the relationship $t_1 = t_2 A$ holds. In the add-drop structure, the interference of the fields happens only in the THRU waveguide. Therefore, the power

coupled to the DROP waveguide can be simply interpreted as an additional source of the "intrinsic" resonator loss. With this in mind, the above relationship states that the full extinction can be achieved when the coupling loss equals the intrinsic loss of the resonator.

The over-coupled regime happens when $t_1 < t_2 A$, while the inverse is true for the under-coupled case. For these two regimes the resonance has a finite extinction.

The amplitude and phase transfer functions for all three regimes are shown in Figure 2.8(a) and (b), respectively.

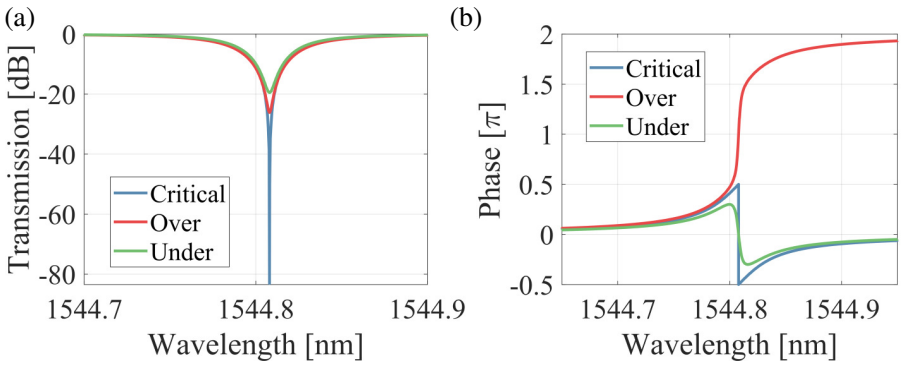

Figure 2.8: Resonator (a) amplitude and (b) phase transfer functions for different coupling regimes.

Modulation in RRMs

The modulation principle of RRMs is illustrated in Figure 2.9. In our RRMs, we focus on the modulation of the signal at the THRU port, which we will refer to as the modulator output in the following. As the applied voltage changes, the resonant wavelength shifts due to the refractive index change (see Equation 2.17). Since the optical carrier wavelength stays fixed (dashed line in Figure 2.9), the amplitude at the modulator output changes (Figure 2.9(a)).

Moreover, amplitude modulation in RRMs is always followed by phase modulation (Figure 2.9(b)). The chirped signal gets distorted after propagating through a dispersive fiber, thus limiting the reach when RRMs are used for modulation. To address this, resonantly assisted Mach-Zehnder interferometers (RA-MZIs) and push-pull dual-ring modulators [64, 65] that allow for chirp-free operation have been demonstrated. This, however, comes with a drawback of the increased modulator complexity.

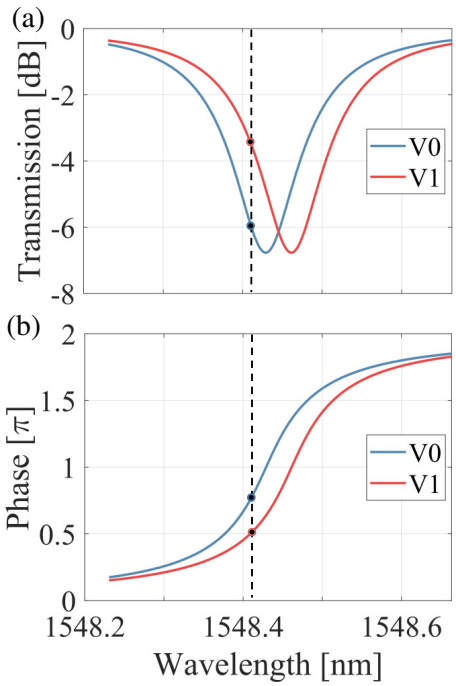

Figure 2.9: Change of resonance wavelength with the applied voltage causes (a) amplitude and (b) phase modulation of the signal at the RRM output. Dashed line marks the position of the optical carrier.

Efficiency metrics

Commonly used efficiency metrics for amplitude modulation are the static extinction ratio (ER), insertion loss (IL) and the optical modulation amplitude (OMA), that encompasses both the modulation efficiency and the insertion losses into a single metric. They are defined by the following expressions:

$$ER = 10 \cdot \log_{10}\left(\frac{P_1}{P_0}\right) \; [dB] \tag{2.19}$$

$$IL = 10 \cdot \log_{10}\left(\frac{P_{in}}{P_1}\right) \; [dB] \tag{2.20}$$

$$OMA = 10 \cdot \log_{10}\left(\frac{P_1 - P_0}{P_{in}}\right) \; [dB]. \tag{2.21}$$

Here, $P_{0/1}$ is the optical power of the logical "0"/"1" levels in the case of on-off keying (OOK) modulation, and P_{in} is the input power.

In RRM mediated modulation these metrics are wavelength/detuning dependent.

Device bandwidth

The bandwidth of RRMs is dictated by two factors: the RC constant of the phase shifter and the spectral width of the resonance.

The RC part is determined by the diode capacitance C_l in F/m and resistance R_l in $\Omega \cdot m$, making the time constant determined solely by the PN junction independent of the device length L. However, the impedance of the driving circuit R_D must also be taken into account (50 Ω in a standard test environment), which additionally penalizes the RC dictated cutoff

$$f_{-3dB,RC} = \frac{1}{2\pi(R_l/L + R_D) \cdot C_l L}. \tag{2.22}$$

Due to their small footprints, RRMs represent point loads from the RF perspective and can therefore be driven as lumped elements (LE). By definition, a device can be considered an LE when its length is on the order $< \lambda_{RF}/10$, where λ_{RF} is the wavelength of the RF wave. Their small size also leads to small capacitance, making them suitable for co-integration (hybrid [66] or monolithic) with high-speed, low output impedance CMOS drivers. This also improves the device's RC dictated cutoff, which is largely influenced by the driver impedance.

The optical cutoff is however usually the limiting one in these structures. Its value varies with the relative position of the optical carrier and the ring resonance, as it results from the peaking in the modulator transient response [67]. The closed form expression that describes this effect can be derived starting from the dynamic relations of the resonator [68]

$$\frac{da(t)}{dt} = \left(i\omega_0 - \frac{1}{\tau_a}\right) a(t) + i\mu E_{in}(t) \tag{2.23}$$

$$E_{THRU}(t) = E_{in}(t) + i\mu a(t), \tag{2.24}$$

where $a(t)$ is the field circulating in the ring, E_{in} the input field, τ_a the cavity photon lifetime, and $\mu^2 = \kappa_1^2 c_0/(n_g L)$ the time domain field coupling coefficient between the ring and the bus waveguide.

By assuming a small periodic perturbation of the resonant frequency $\overline{\delta\omega_0} cos(\omega_m t)$ caused by a modulating signal at angular frequency ω_m, the small-signal response (S_{21}) of the RRM can be calculated as [67]

$$S_{21} = -\mu Re\left\{\left[\frac{(E_0 + i\mu\overline{a})^* \overline{\delta\omega_0}\,\overline{a}}{i\omega_m + i(\omega - \omega_0) + 1/\tau_a} + \frac{(E_0 + i\mu\overline{a})\overline{\delta\omega_0}^*\,\overline{a}^*}{i\omega_m - i(\omega - \omega_0) + 1/\tau_a}\right] e^{i\omega_m t}\right\}. \tag{2.25}$$

Here, E_0 and ω are the amplitude and the angular frequency of the input optical field $E_{in}(t) = E_0 exp(i\omega t)$. Consequently, a also oscillates at the input frequency as

$\overline{a}exp(i\omega t)$, with the complex amplitude

$$\overline{a} = \sqrt{\frac{n_g L}{c_0}} \frac{i\kappa_1}{1 - t_1 t_2 e^{(-i\beta - \alpha/2)L}}. \tag{2.26}$$

Furthermore, $\overline{\delta\omega_0} = \delta\omega_0 - i\delta(1/\tau_a)$ in Equation 2.25 is the change of the resonant frequency with modulation. It can have a complex value, when both the effective index and the modal loss change with voltage, as in the case of Si RRMs. From the above expression we can see that when the optical carrier is biased away from the ring resonance (i.e. the detuning $\Delta\omega = \omega - \omega_0 \neq 0$) one of the sidebands gets amplified, giving rise to the peaking response of the resonator. This in turn extends the bandwidth of the RRM at larger detunings beyond the one dictated by the cavity photon lifetime.

Quality factor and finesse

Resonant cavity is often characterized by its quality factor (Q), which is the measure of the sharpness of the resonance relative to its central frequency. It can therefore be calculated as

$$Q = \frac{\omega_0}{FWHM}, \tag{2.27}$$

where FWHM is the full width at half maximum of the resonant curve.

It is also defined as the ratio of the stored energy circulating in the resonator to the energy lost per optical cycle

$$Q = \omega_0 \frac{Stored\ energy}{Power\ loss}, \tag{2.28}$$

and it can be related to overall resonator power loss per unit length α_{dis} as

$$Q = \frac{\omega_0 \cdot n_g}{\alpha_{dis} \cdot c_0}. \tag{2.29}$$

It is often differentiated between the intrinsic (Q_{int}) and the loaded (Q_{load}) quality factor of the RRMs. Q_{int} encompasses only the internal resonator losses, such as absorption and bending losses, described in our notation by α

$$Q_{int} = \frac{\omega_0 \cdot n_g}{\alpha \cdot c_0}. \tag{2.30}$$

In addition, Q_{loaded} takes into account the power lost from the resonator through waveguide coupling. To express this, it is more convenient to consider coupling losses to be distributed over the whole resonator length. The loaded Q factor can then be written as

$$Q_{loaded} = \frac{\omega_0 \cdot n_g}{\left(\alpha + \frac{2ln(t_1)}{L} + \frac{2ln(t_2)}{L}\right) \cdot c_0}. \tag{2.31}$$

Through constructive interference and feedback, resonators enhance the effective path length of the fields traversing them and, with that, the accumulated phase shift. This enhancement is captured in the factor called the finesse $\mathscr{F}$. It represents the sharpness of the resonances relative to their separation and is given by [69]

$$\mathscr{F} = \frac{FSR}{FWHM}. \tag{2.32}$$

Finesse has a close relationship with the Q factor. Physically, the Q factor represents the number of oscillations of the field inside of the resonator that occur before the circulating energy reduces to $1/e$ of the initial value. Similarly, finesse represents, within a factor of 2π, the number of round-trips made by light in the ring until reaching the same reduction in energy. For an add-drop structure and a resonance of order m, they are related as

$$Q = m\mathscr{F}. \tag{2.33}$$

Furthermore, Q can be related to the cavity photon lifetime τ_a. By solving Equation 2.23 when the input field is turned off ($E_{in} = 0$), we arrive at the expression for the optical energy inside of the ring

$$|a|^2 \propto exp(-2t/\tau_a). \tag{2.34}$$

This shows that during the time $\tau_a/2$ power in the ring reduces by a factor $1/e$. From the above definition for Q, the two quantities are therefore related as

$$\tau_a = \frac{2Q}{\omega_0}. \tag{2.35}$$

Power consumption

Another crucial performance metric is the power consumption of the device. RRMs dissipate power only when switched, with the energy per bit given as

$$E_{bit} = \frac{1}{4}CV^2, \tag{2.36}$$

where C is the junction capacitance, and V the applied voltage. The additional factor $1/2$ reflects the fact that the switching on average happens 50% of the time. According to [70, 71], LE devices show a five-fold improvement in power consumption compared to the well-designed traveling wave (TW) structures of the same length, which makes them more suitable for low-energy applications. In addition to that, the phase shift efficiency of RRMs is boosted through resonant enhancement. Assuming the same drive voltage, the equivalent phase shift can therefore be achieved with a shorter phase shifter in a form of a resonator, i.e. with a device that has a

smaller capacitance. Thus, the power consumption in rings is improved by a factor proportional to finesse compared to the linear LE phase shifter [67].

As already noted, RRMs are frequency selective and can simultaneously be used as modulating and multiplexing elements, which makes them very suitable for WDM applications. However, resonant wavelengths can deviate from the standard WDM grid points due to the fabrication induced effective index variation and must be adjusted using on-chip thermal tuners. This adds substantially to the overall power consumption of the component. Additionally, due to their narrow optical bandwidth, changes in the environment, as well as fluctuations of other system components, can change the operating point and significantly influence the performance of the modulator. Therefore, an active control system that tracks and adjusts the operating point of the device must be implemented [72, 73] for their reliable application in real links, adding to the complexity of the transmitter. To tackle the thermal sensitivity, resonantly enhanced structures in which multiple over-coupled resonators that all address the same WDM channel are coupled to the arms of the interferometer have been used to increase the operating wavelength span while still maintaining the LE operation [74–76].

2.2 Experimental results

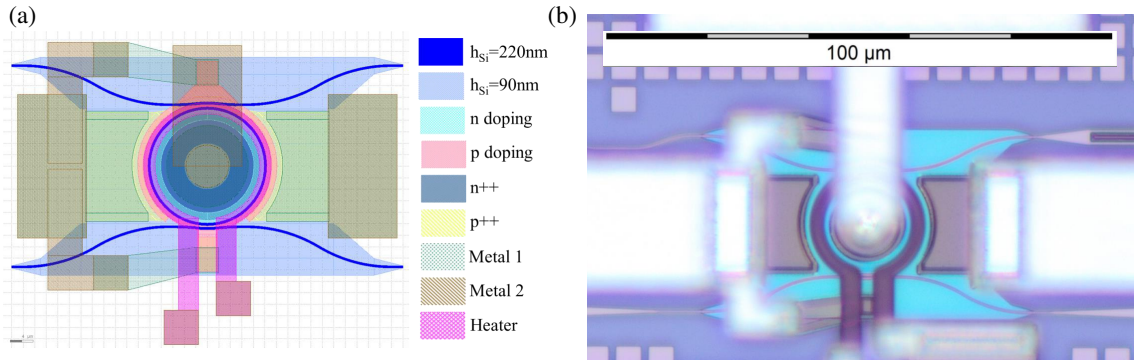

Figure 2.10: (a) Layout and (b) micrograph of a standalone RRM

RRMs used in this work are depletion-based devices. The layout of the structure and a micrograph of a fabricated device are shown in Figure 2.10(a) and (b), respectively. The devices have an add-drop configuration, where a small percentage of the optical power is sent to the DROP port to be used for monitoring and control purposes. The 430 nm wide rib waveguides, comprised of a 220 nm thick Si core and 90 nm thick Si slab, make up both the bus and the ring section. The chips were fabricated at the Institute of Microelectronics, IME, Singapore, in a standard multi-project wafer (MPW) run.

The geometry of the directional coupler between the ring and the bus waveguides has a structure shown in Figure 2.11. A larger radius ($RBUS$) bus waveguide wraps around the ring section of radius R in a small angular span (ΘBUS). The bus waveguide is then gradually distanced from the ring through a straight waveguide ($Lstr$), followed by a bent waveguide section with a radius $ROUT$ and an angular span of ΘOUT. Relevant geometrical parameters are summarized in Table 2.1. This coupler structure shows better tolerance to fabrication induced variations of the geometry, including waveguide width and slab height, when compared to conventional, straight bus waveguide couplers. The improved tolerance comes in part from the smaller variance of the phase matching condition between the modes of the bus and ring waveguides with the changing waveguide width [77]. To a lesser degree, it is a result of a less variant overlap between the modes of the two bent waveguides when the geometry varies, when compared to the scenario where one waveguide is straight and the other one is bent [78, 79]. These phenomena lead to a less variant coupling strength at the coupler section. In an RRM, coupling strength is one of the main parameters that determine the device performance, influencing both the efficiency and the bandwidth of the modulator. The new coupler design therefore ensures that the performance of the fabricated devices is close to the targeted one.

wBUS	wRing	R	Lstr	RBUS	ΘBUS	ROUT	ΘOUT	Gap THRU	Gap DROP
430 nm	430 nm	10 μm	2 μm	16 μm	10°	16 μm	10°	295 nm	475 nm

Table 2.1: Geometrical parameters of the RRM.

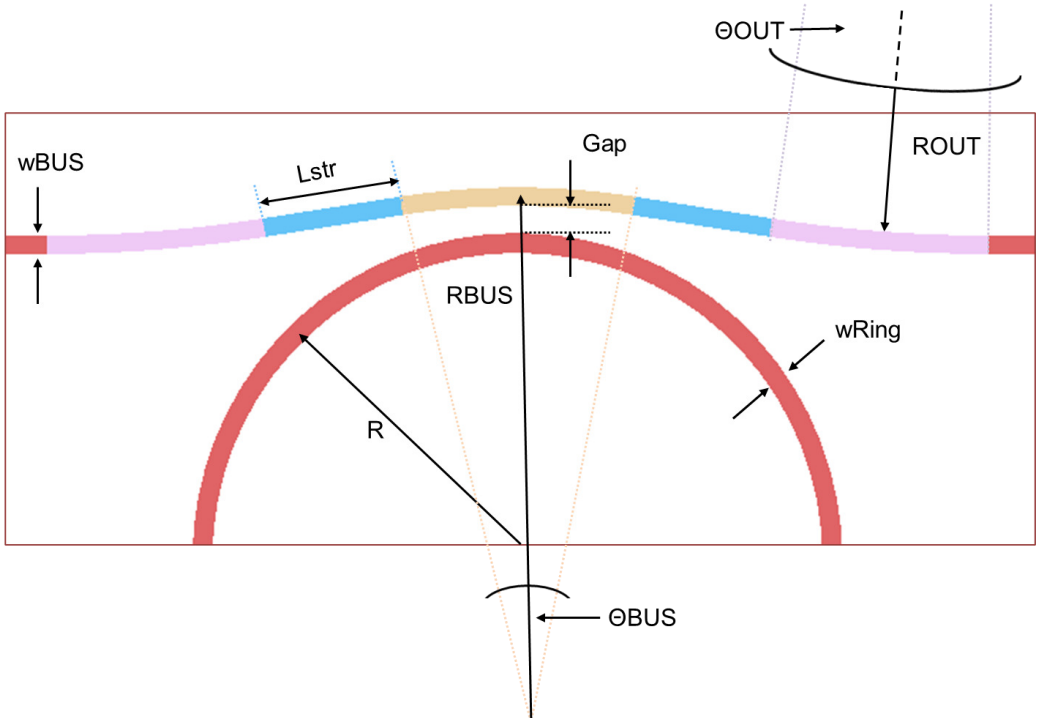

Figure 2.11: Geometry of the directional coupler between the bus and ring waveguides in RRM.

2.2.1 Passive characterization

First, passive device characterization is performed to determine the device losses and coupling strengths between the ring and the bus waveguides.

To determine the resonator's intrinsic loss and coupling strength between the ring and the THRU waveguide, we first measure a test structure which does not feature a DROP waveguide, but is otherwise identical to the final device (Figure 2.12(a)). The optical input/output (I/O) to this and all the following structures is realized through a pair of vertically emitting grating couplers (GCs), where light is coupled into the chip through one and coupled out from the chip through the other GC. Transmission of the first test structure is shown in Figure 2.12(b). Here, the envelope of the curve corresponds to the GC-pair spectrum, with an IL of $\sim 8\ dB$ at maximum transmission. Coupling coefficient and the intrinsic loss parameter were determined by fitting of

multiple resonances with a Lorentzian function, after normalizing out the GC spectrum [80] (Figure 2.12(c)). The fitting function's coefficients are interchangeable, so to assign one to the coupling and the other to the propagation loss, we must plot them versus wavelength. The absorption coefficient does not change notably across the span of several FSRs, while the coupling strength shows significant wavelength dependence. In Figure 2.12(d) the field transmission coefficient (t_1) of the directional coupler and the the power remaining in the ring after a single round trip ($A = exp(-\alpha/2 \cdot L)$) are plotted as a function of wavelength.

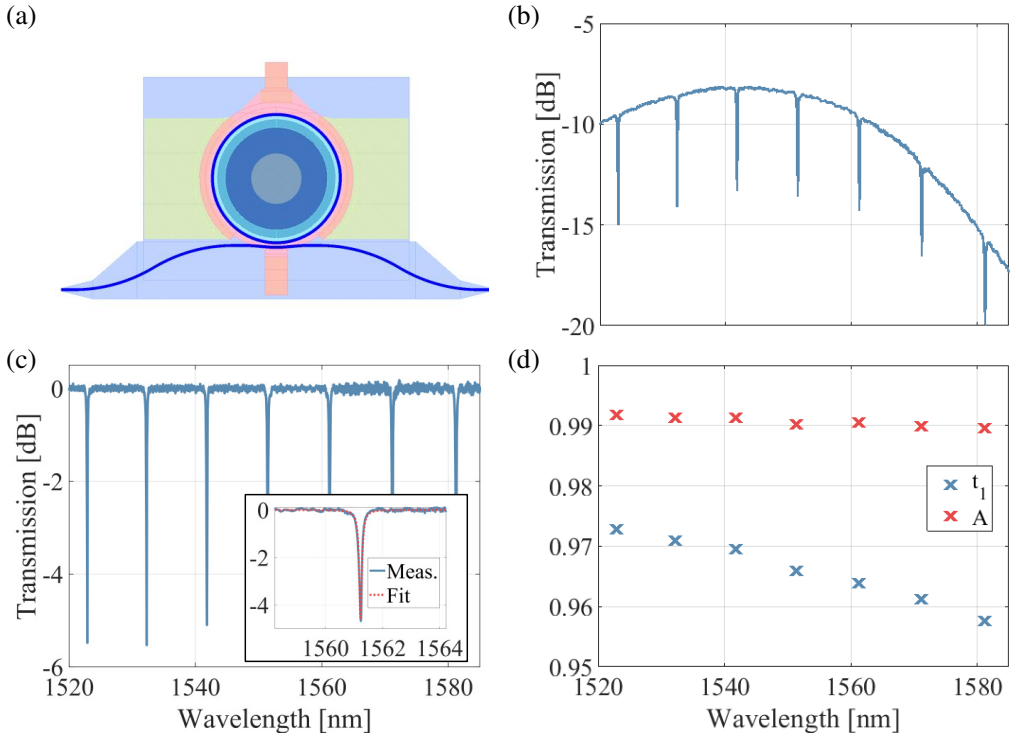

Figure 2.12: (a) Layout of the characterized test structure; (b) Transmission; (c) Normalized transmission and fitted resonance. (d) Extracted t_1 and A parameters from multiple resonance fits.

In addition to coupling and intrinsic loss, parameters such as FSR and n_g can be extracted from the resonance fits. From measurements of numerous structures on multiple chips we calculate the average values of all these quantities and summarize them in Table 2.2, for the resonance nearest to 1550 nm. Here, $\alpha_{dB} = \alpha \cdot 10 \cdot log_{10}(e)$.

Next, we measure the transmission of the full modulator identical to the ones used in our system and depicted in Figure 2.10. With the same approach of resonance fitting, we extract the coupling strength between the ring and the THRU waveguide and the loss of this structure. The loss, however, now includes both the intrinsic losses and the loss due to the presence of the DROP waveguide. Therefore,

κ_1	α_{dB}	FSR	n_g
0.258	12.8 dB/cm	9.8 nm	3.87

Table 2.2: Average values of extracted RRM parameters.

A in the fitting function is replaced by At_2. The quantities extracted from fits of multiple resonances are plotted in Figure 2.13. The loss term has a stronger wavelength dependence compared to Figure 2.12(d) because of the inclusion of DROP waveguide coupling. Nevertheless, this dependence is weaker than the one for t_1 due to the weaker coupling to the DROP port and the corresponding lowered sensitivity to wavelength. Given that $t_1 < At_2$ holds for the wavelength span of interest, our RRMs are over-coupled. By knowing the value of intrinsic losses A from the characterization of the first test structure type, these measurements allow us to extract κ_2. The average value of κ_2 is finally calculated to be 0.071.

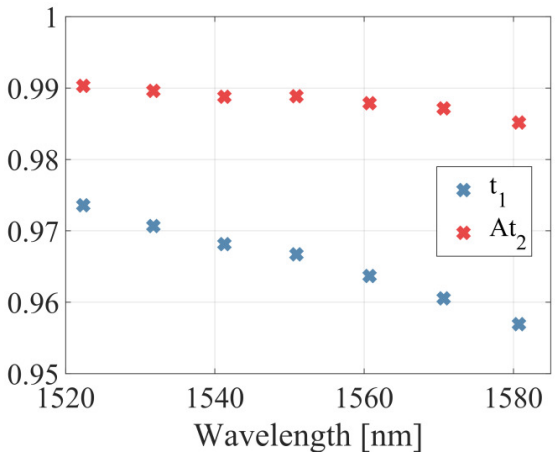

Figure 2.13: Extracted t_1 and At_2 parameters from multiple resonance fits of the full RRM structure.

2.2.2 DC characterization

To extract the tuning efficiency in terms of effective index change and wavelength shift, we measure full RRM transmission for different reverse bias voltages applied to its terminals. The exemplary resonance shift with the applied voltage is shown in Figure 2.14(a). Wavelength tuning efficiency ($\Delta\lambda$) can be directly read from the resonance shift, while the effective index change can be calculated as

$$\Delta n_{eff} = \frac{\lambda_0 \Delta\lambda}{FSR \cdot L}. \tag{2.37}$$

These are extracted from a number of measurements of full RRM structures and shown in Figure 2.14(b) and (c). The median values of Δn_{eff} and wavelength tuning efficiency are $6.8 \cdot 10^{-5}$ and 13.5 pm/V, respectively, between 0 and -2 V reverse bias.

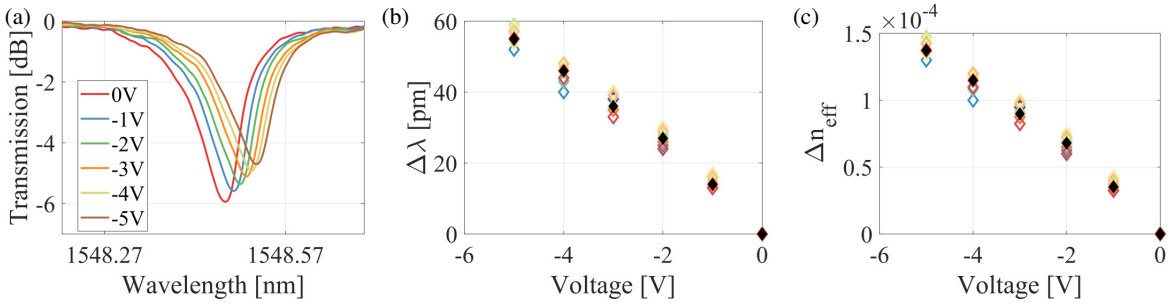

Figure 2.14: (a) RRM transmission for different applied reverse bias voltages. (b) Resonance shift and (c) change of the modal effective index for different applied voltages, relative to 0V; black markers specify the median value.

The coupling regime can also be determined from the spectra recorded for different applied voltages. Namely, as we increase the reverse bias of the RRMs, the carriers are removed from the center of the waveguide. The overlap of the optical mode with the free carriers reduces, thus reducing the intrinsic loss of the resonator. If the ring is initially under-coupled (for the applied voltage of 0 V), reduction of the intrinsic loss will bring its value closer to that of the coupling loss, i.e. closer to the critical coupling condition. The extinction of the resonance will therefore increase. Conversely, in the initially over-coupled structure, resonance extinction will reduce with the increased reverse bias voltage, as in the case of our devices in Figure 2.14(a).

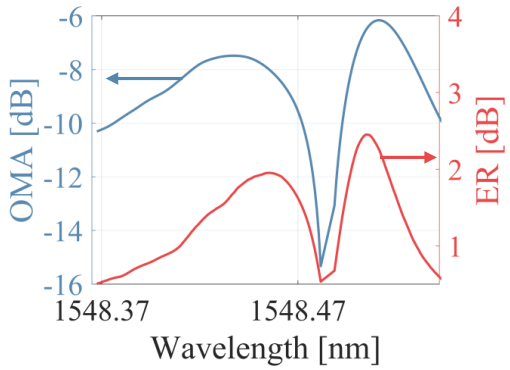

Figure 2.15: Amplitude modulation efficiency metrics: OMA (in blue, left axis) and ER (in red, axis) between 0 and 2 V reverse bias.

Moreover, the amplitude modulation efficiency metrics can be extracted from the voltage sweeps. Assuming a bias voltage of -1 V and a modulating voltage swing of 2 V peak-to-peak, we calculate the wavelength dependent OMA and ER (Figure 2.15).

Furthermore, RRMs feature thermal tuners that allow for adjustment of their resonant wavelengths. Tuners are 200 μm wide on-chip titanium nitride (TiN) patches that cover 95% of the ring's circumference. By applying voltage to the tuner's terminals, heat is dissipated in the waveguide, changing the effective index of the propagating mode. With this, resonant wavelegths shift, as can be seen in Figure 2.16(a). The wavelength shift is proportional to the dissipated power. On average, for a 2π phase shift, equivalent to a wavelength shift ($\Delta\lambda$) of one FSR, 110 mW of power is needed (Figure 2.16(b)).

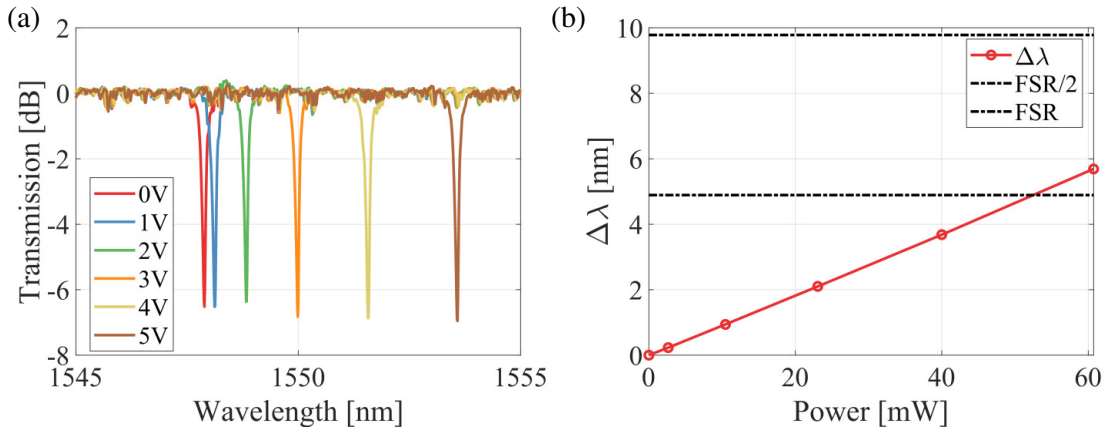

Figure 2.16: (a) RRM transmission for different voltages applied to its tuner. (c) Dependence of the resonant shift on the power dissipated by the tuner.

2.2.3 High-speed characterization

High-speed characterization measurement setup is shown in Figure 2.17(a). The sinusoidal RF signal at frequencies up to 50 GHz is generated by a programmable network analyzer (PNA) and applied using ground-signal-ground (GSG) high-speed probes to the modulator contact pads, along with a DC bias of -1 V to ensure operation in the depletion mode. Optical signal is supplied by a tunable external cavity laser, coupled through a fiber array to the on-chip GCs. Coupled out light is routed to the high-speed commercial photodetector (PD) and the resulting electrical signal is routed back to one of the ports of the PNA. The experiments are repeated for the varying optical carrier to ring resonance detuning. Optical power is monitored before the PD. Calibrated S_{21} response for several detunings is shown in Figure 2.17(b). The -3 dB cutoff frequency (f_{-3dB}), calculated relative to 1 GHz, is shown in Figure

2.17(c) versus wavelength. The position of the ring resonance is indicated by the dotted gray line. The asymmetry of the small-signal response relative to the resonant wavelength, mirrored in the asymmetric dependency of the f_{-3dB}, can be attributed to loss modulation present in Si RRM devices, as given by Equation 2.25.

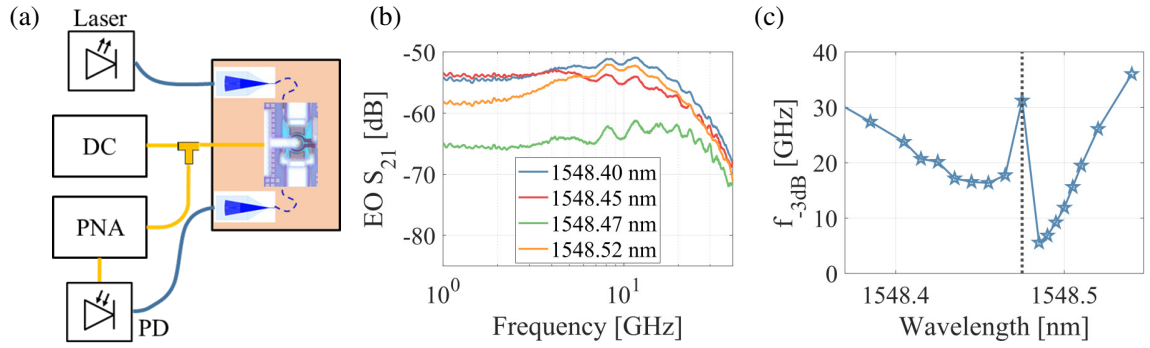

Figure 2.17: (a) Measurement setup for high-speed characterization of RRMs; (b) Electro-optical S_{21} at several detuning points; (c) 3 dB cutoff frequency versus optical carrier wavelength; dotted gray line marks the RRM resonance.

2.2.4 RA-SSB modulator

The single-sideband modulator is formed by coupling two identical RRMs each to an arm of an MZI. The arm lengths are balanced and the 90-degree phase shift between the arms, ensuring the quadrature condition, is introduced passively through a 2-by-2 multi-mode interferometer (MMI) used as a power splitter at the input of the interferometer. To correct for fabrication induced phase offset from the quadrature point, on-chip TiN thermal tuners are implemented in the MZI arms. As before, the optical signal is coupled in and out of the chip through surface emitting GCs. The three-channel system is simply formed by adding two more sets of RRMs along each arm of the MZI, each tuned to a different wavelength to address an additional WDM channel.

Schematic and layout of the system are shown in Figure 2.18(a) and (b), respectively. Optical transmission of the system is shown in Figure 2.19(a), where resonances of the RRMs belonging to each channel are indicated (the obscured resonances belong to the unused channel [1]).

[1]Initially, a four-channel system was taped out. However, one of the channels on the measured chip could not be addressed due to the damage on the heater pads. It was therefore impossible to align the resonances of the I and Q RRMs, rendering the channel unusable in the SSB configuration. This is why in this work we refer to a three-channel system.

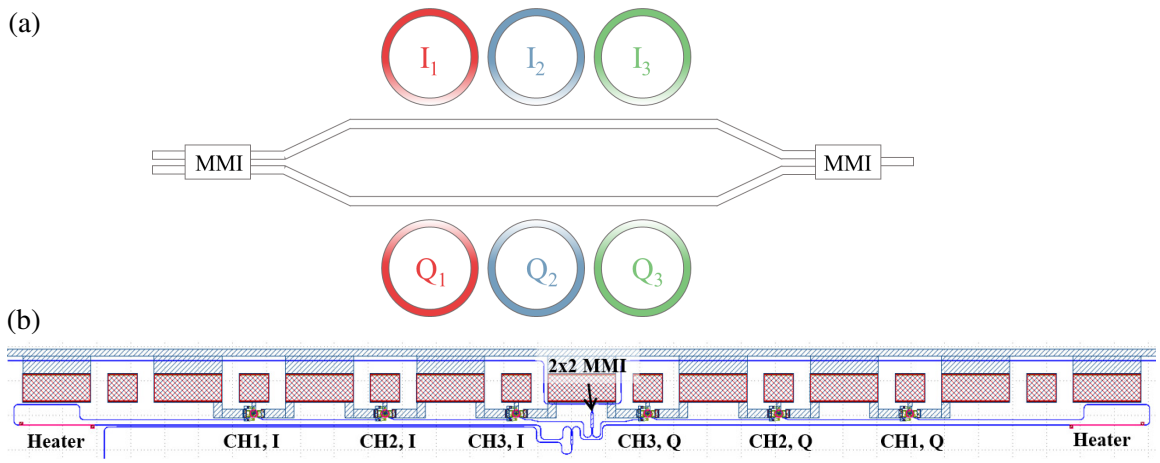

Figure 2.18: (a) Schematic and (b) layout of the 3-channel RRM assisted SSB modulator.

The phase shifters used to bias the MZI are 2 μm wide, 200 μm long TiN resistors (1 $k\Omega$), located above the waveguides. By applying different voltages to the tuners and monitoring the out-of-resonance optical power, we can determine how much electrical power is needed for a 2π phase shift (Figure 2.19(b)). This amount of phase shift allows us to reach the quadrature condition from any bias point at the system start-up. The electrical power consumption required to achieve a 2π phase shift is therefore 25 mW. The RRM tuners show higher power consumption due to the presence of RF metal lines in the device vicinity. They conduct a part of the heat away, making it more difficult to heat up the device.

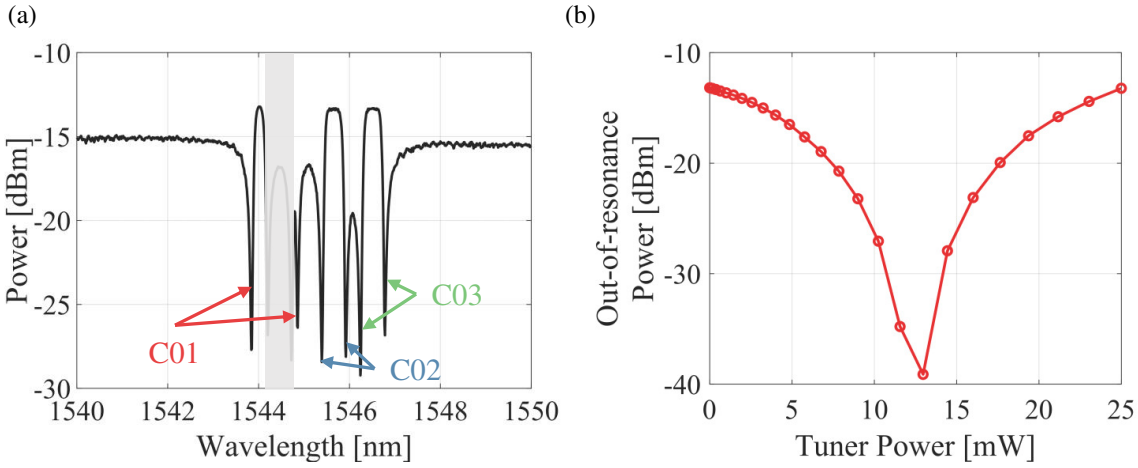

Figure 2.19: (a) Transmission of the RA-SSB system. (b) Performance of the tuner in MZI arms.

Chapter 3

Laser Phase Noise in Ring Resonator Assisted Direct Detection Data Transmission

This chapter covers the results published in [81], Sections I, II and III A&B. The analytical modeling was the joint work of Prof. Jeremy Witzens and the author. The numerical modeling, design and execution of experiments, and data analysis was performed by the author.

3.1 Introduction

To properly determine the required power budget for a given link scenario, a good understanding of all the noise sources that contribute to the overall signal-to-noise ratio (SNR) is essential. In our study, we put the focus on the noise sources associated with the optical source, primarily on the laser phase noise. In ring assisted modulation, laser phase fluctuations get translated into optical intensity variations at the device output [82]. Although small in magnitude, they can become significant when a high-linewidth source is employed and/or when a modulation format characterized by a small signal standard deviation, such as OFDM, is applied, and can therefore deteriorate the directly detected signal's quality. A use case of great interest in the context of increased parallelization is the utilization of semiconductor mode-locked lasers (MLL) as optical sources [83, 84]. A single MLL can provide multiple optical carriers for different WDM channels, eliminating the need for banks of bulky, discrete sources and multiplexers. Its noise characteristics, including linewidth in the order of 5 MHz and relative intensity noise (RIN) in the order of -120 dBc/Hz [85], however, may pose a limitation to the system. For this reason, it is crucial to understand how phase noise of the optical source affects system performance when

RRMs are used for modulation.

In this chapter, we first derive the analytical expressions that describe the statistical and spectral properties of the laser phase noise induced intensity noise at the output of a ring resonant modulator (Section 3.2). We further describe a set of experiments, in which SSB-OFDM signals are transduced to the optical domain using an RA-MZM, specifically designed to test the validity of our model. This includes a description of the experimental setup and the data processing methodology (Sections 3.3.1 and 3.3.2). Finally, by combining our analytical model of phase to intensity noise conversion with the numerical simulations of the rest of the optical link (described in detail in Section 3.3.3), we compare the measurements with the modeling results (Section 3.3.4). It should be noted that although here we focus on SSB-OFDM data transmission, the analytical model of phase noise conversion is not specific to this case and is applicable whenever RRMs are used for modulation, and can therefore be applied to a wide variety of optical links.

3.2 Analytical model of phase to intensity noise conversion

Ring resonator modulators act as light storing elements. During the time the light is stored in the cavity the phase of the input optical signal walks off, as dictated by the non-zero phase noise of the optical source. This in turn changes the interference condition between the two signals, one coupled back from the waveguide loop and the other transmitted at the directional coupler in the bus waveguide, which leads to a change in intensity at the resonator output.

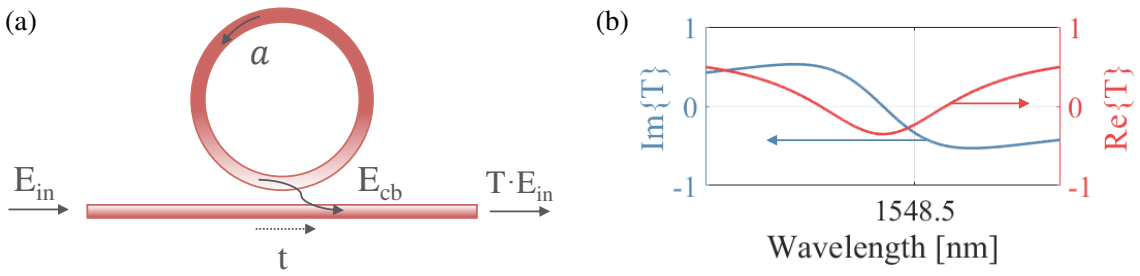

Figure 3.1: (a) All-pass resonator configuration; (b) imaginary (in blue, left axis) and real (in red, right axis) parts of the field transmission coefficient T.

To describe this process analytically, we consider an all-pass resonator structure depicted in Figure 3.1(a). We start our derivation from the differential equation that

describes the time evolution of the field circulating in the ring, a [68]:

$$\frac{da}{dt} = i\omega_0 a - \frac{a}{\tau_a} + i\mu E_{in}, \tag{3.1}$$

where ω_0 is the angular resonance frequency, τ_a the cavity lifetime associated to the E-field, μ the time domain coupling coefficient between the ring and the bus waveguide, and E_{in} the field input to the bus waveguide in the absence of noise. The presence of another bus waveguide in the add-drop configuration can be simply included in the analysis through an additional time constant associated with the coupling coefficient at the ring-bus coupler section. In this calculation, the time constants add as a sum of inverse values, i.e. $1/\tau_{tot} = \sum_i 1/\tau_i$. The input field, oscillating at the angular frequency ω, can be written as

$$E_{in} = E_0 exp(i\omega t). \tag{3.2}$$

An infinitesimal phase increment in the input field acts as a step perturbation $i\delta\varphi E_0 e^{i\omega t}$, after linearization ($E_0 e^{i\omega t + i\delta\varphi} \simeq E_0 e^{i\omega t}(1 + i\delta\varphi)$). The response of the ring, δa, further satisfies the differential equation

$$d(\delta a)/dt = i\omega_0 \delta a - \delta a/\tau_a - \mu\delta\varphi E_0 e^{i\omega t} \tag{3.3}$$

with the solution given as

$$\delta a = K e^{i\omega t}\left[1 - e^{-t/\tau_a - i(\omega-\omega_0)t}\right], \tag{3.4}$$

where

$$K = -\frac{\mu\delta\varphi E_0}{1/\tau_a + i(\omega - \omega_0)}. \tag{3.5}$$

The response of the ring approaches its new steady-state value $Kexp(i\omega t)$ with a time constant τ_a. Once this value has been reached, the phase of the field inside of the ring is fully tracking the phase of the field in the bus waveguide, $\delta\varphi$, which is evident when comparing the unperturbed amplitude a and the new steady state expression. The transient deviation of the field amplitude inside of the ring is therefore given by

$$\delta a - K e^{i\omega t} = -K e^{-t/\tau_a + i\omega_0 t}. \tag{3.6}$$

This translates in turn into a deviation of the field coupled back from the ring to the bus waveguide

$$\frac{i\mu^2\delta\varphi E_0}{1/\tau_a + i(\omega - \omega_0)} e^{-t/\tau_a + i\omega_0 t} = -i\delta\varphi E_{cb} e^{-t/\tau_a - i(\omega-\omega_0)t} = E_{cb}(\delta\eta + i\delta\theta), \tag{3.7}$$

where $E_{cb} = -\mu^2 E_0 exp(i\omega t)/(1/\tau_a + i(\omega - \omega_0))$ corresponds to the field coupled back from the ring in the absence of phase noise. This field deviation can further be decomposed into the components in-phase and out-of-phase with the unperturbed coupled-back field E_{cb}, where $\delta\eta$ is the relative amplitude noise and $\delta\theta$ is the phase error, as per notation in Equation 3.7.

Assuming that the laser phase noise follows a Wiener process, with the corresponding Lorentzian linewidth $\Delta\nu$, the variance of the phase increment $\delta\varphi$ can be written as $2\pi\Delta\nu dt$, where dt denotes the time step. The effects of the individual phase jumps are independent of each other and thus add as a sum of variances, after being weighed by the step response of the ring, $-i \cdot exp(-t/\tau_a - i(\omega - \omega_0)t)$. This results in the variance of the phase term given by

$$\sigma_{\delta\theta}^2 = \int_0^\infty \left[Re\left\{-e^{-t/\tau_a - i(\omega-\omega_0)t}\right\}\right]^2 2\pi\Delta\nu dt = 2\pi\Delta\nu\frac{\tau_a}{4}\left(1 + \frac{1}{1+\tau_a^2(\omega-\omega_0)^2}\right), \quad (3.8)$$

and the variance of the amplitude term by

$$\sigma_{\delta\eta}^2 = \int_0^\infty \left[Im\left\{e^{-t/\tau_a - i(\omega-\omega_0)t}\right\}\right]^2 2\pi\Delta\nu dt = 2\pi\Delta\nu\frac{\tau_a}{4}\left(1 - \frac{1}{1+\tau_a^2(\omega-\omega_0)^2}\right). \quad (3.9)$$

In addition to that, the co-variance of the two terms is non-zero in certain cases, and is given by

$$\begin{aligned}\sigma_{\delta\theta\delta\eta} &= \int_0^\infty Re\left\{-e^{-t/\tau_a - i(\omega-\omega_0)t}\right\} \cdot Im\left\{e^{-t/\tau_a - i(\omega-\omega_0)t}\right\} 2\pi\Delta\nu dt \\ &= 2\pi\Delta\nu\frac{\tau_a^2}{4}\frac{\omega-\omega_0}{1+\tau_a^2(\omega-\omega_0)^2}.\end{aligned} \quad (3.10)$$

The total power at the resonator output P_{out} can then be written as

$$\begin{aligned}P_{out}/P_{in} &= \left|E_{in} + E_{cb}(1+\delta\eta)e^{i\delta\theta}\right|^2/P_{in} \\ &\approx \left|TE_{in} + E_{cb}\delta\eta + iE_{cb}\delta\theta\right|^2/P_{in} \\ &\approx |T|^2 - 2Im\{T\}\delta\theta + 2\Big(Re\{T\}Re\{T-1\} + Im\{T\}^2\Big)\delta\eta \\ &= |T|^2 + \delta I,\end{aligned} \quad (3.11)$$

where P_{in} is the power at the input, $T = 1 + E_{cb}/E_{in}$ is the resonator field transmission coefficient at the optical carrier frequency ω, and δI is the relative intensity noise at the resonator output. In this derivation we used the equality $2Re\{T \cdot (iE_{cb}/E_{in})^*\} = 2Im\{T \cdot (T-1)^*\}$.

The overall amplitude transfer function of the ring at the carrier frequency can be written as $T = 1 - \mu^2\tau_a/(1 + i(\omega - \omega_0)\tau_a)$. Here, $(\omega - \omega_0)\tau_a = 2Q_{loaded}(\omega - \omega_0)/\omega_0$ and $\mu\sqrt{\tau_a}$ are normalized frequency detuning from the ring resonance and the normalized coupling coefficient, respectively. The normalized coupling coefficient can

be interpreted as follows: $\mu\sqrt{\tau_a} = 1$ holds for the critically coupled ring, where the intrinsic losses equal the coupling losses. On the other hand, for our over-coupled ring, $\mu\sqrt{\tau_a} > 1$ holds. The variance of the overall intensity noise at the resonator output is, based on previous expressions, given as

$$\begin{aligned}\sigma_{\delta I}^2 =& 4\Big[\big|Im\{T\}\big|^2\sigma_{\delta\theta}^2 \\ &+ \big|Re\{T\}Re\{T-1\} + Im\{T\}^2\big|^2\sigma_{\delta\eta}^2 \\ &- 2Im\{T\}\big(Re\{T\}Re\{T-1\} + Im\{T\}^2\big)\sigma_{\delta\theta\delta\eta}\Big].\end{aligned} \tag{3.12}$$

The first two terms correspond to the variance of the phase and amplitude noise of E_{cb}, respectively, and they add up. The third term is their co-variance, which takes a negative value in the case of our over-coupled resonator, reducing thus the overall RIN. The imaginary and real parts of the field transmission coefficient T are shown in Figure 3.1(b).

After applying some algebraic manipulations, the above expression can be more compactly written as

$$\sigma_{\delta I}^2 = 2\pi\Delta\nu\tau_a \cdot (\omega-\omega_0)^2\tau_a^2 \cdot \mu^4\tau_a^2 \cdot \left[\frac{1}{\big(1+(\omega-\omega_0)^2\tau_a^2\big)^2} + \frac{(2-\mu^2\tau_a)^2}{\big(1+(\omega-\omega_0)^2\tau_a^2\big)^3}\right]. \tag{3.13}$$

Equation 3.13 gives a closed form expression for the standard deviation of the laser phase noise induced intensity noise at the resonator output, as a function of the source linewidth ($\Delta\nu$), the cavity photon lifetime (τ_a), the carrier to resonance frequency detuning ($\omega-\omega_0$), and the ring to bus waveguide coupling strength (μ). As expected, the induced intensity noise is proportional to $2\pi\Delta\nu\tau_a$, the walk-off of the phase of the input field which occurs in the time interval equal to the average field lifetime in the resonator. Detailed derivations of Equations 3.12 and 3.13 can be found in Appendix A.

To verify these results numerically, we implemented a simple stochastic model and compared its outputs to the analytical predictions. The laser phase noise is modeled as a Wiener process and the propagation through the resonator is simulated by solving the resonator dynamic equation (Equation 3.3), with the field amplitude at the resonator output, E_{out}, calculated as

$$E_{out} = E_{in} + i\mu a. \tag{3.14}$$

All other noise sources, including the laser RIN, are not considered here, in order to isolate the effect of the laser phase noise. The source linewidth is assumed to be 1 MHz, and the power input to the ring is set to 2.2 dBm. This corresponds to the receiver referred power level of an experiment described in the next section in which

the output power of the distributed feedback laser (DFB) source is 6 dBm, and the total link amplification and attenuation are taken into account when scaling the power level. Finally, to convert to voltage units, a 150 V/W receiver conversion gain is assumed, the same as in our experiments. The modeled RRM also has characteristics of the fabricated devices used in the experiments. These include the loaded Q factor of 11000, intrinsic Q factor of 52500, the coupling strength given by $\mu^2 = 82.5\ ns^{-1}$, and the photon storage time by $\tau_a = 18\ ps$.

The numerical calculations show that the phase noise induced intensity noise at the resonator output follows Gaussian statistic, with zero mean value and wavelength dependent standard deviation, closely matching the theoretical predictions. Figure 3.2(a) shows histograms of the recorded noise samples for various biasing points of the optical carrier, overlaid with the corresponding Gaussian fits. In Figure 3.2(b) we show separately the standard deviations of the amplitude noise term (in red), phase noise term (in blue), and the total induced intensity noise (in green) as given by the analytical (solid lines) and numerical (lines with markers) models. The close to perfect matching of the analytical and numerical results for all the individual terms gives us therefore a higher confidence in our analytical predictions.

Moreover, the above results indicate that when the optical carrier and the resonant frequency coincide (i.e. $\omega - \omega_0 = 0$) the induced RIN vanishes. In this case the transient field coupled back from the ring ($E_{cb}(\delta\eta + i\delta\theta)$) is in quadrature with the resonator output field when no noise is present ($T \cdot E_{in}$). The interference term between the two fields is, therefore, zero and does not create amplitude noise at the resonator output. While biasing at resonance would not be beneficial when the RRM is used for amplitude modulation, since the electro-optical S_{21} is zeroed in this case, in our RA-MZM structure RRMs are used as phase shifters whose efficiency is at the maximum at resonance. We can thus exploit this fact to, at the same time, minimize the phase noise induced RIN in our experiments.

Another way of reaching the above conclusion is by focusing on the transfer function of the resonator, rather than on its light storing functionality. Apart from affecting the signal amplitude, the resonator also inflicts a phase change which is wavelength dependent. This changes the phase relationship between the upper and lower noise frequency sidebands, converting a portion of the phase noise to intensity noise, and vice versa. This is similar to the phase to intensity noise conversion which occurs during signal propagation over long stretches of dispersive optical fibers [86]. The resonator dispersion is zero at resonance, due to the anti-symmetricity of the phase transfer function, leading to the mentioned nulling of the induced RIN. A similar effect is also present in lasers that use atomic-like gain media that exhibit symmetric gain spectra [87]. For these devices, the linewidth broadening factor, that in essence describes phase to intensity noise conversion, vanishes at the resonant frequency.

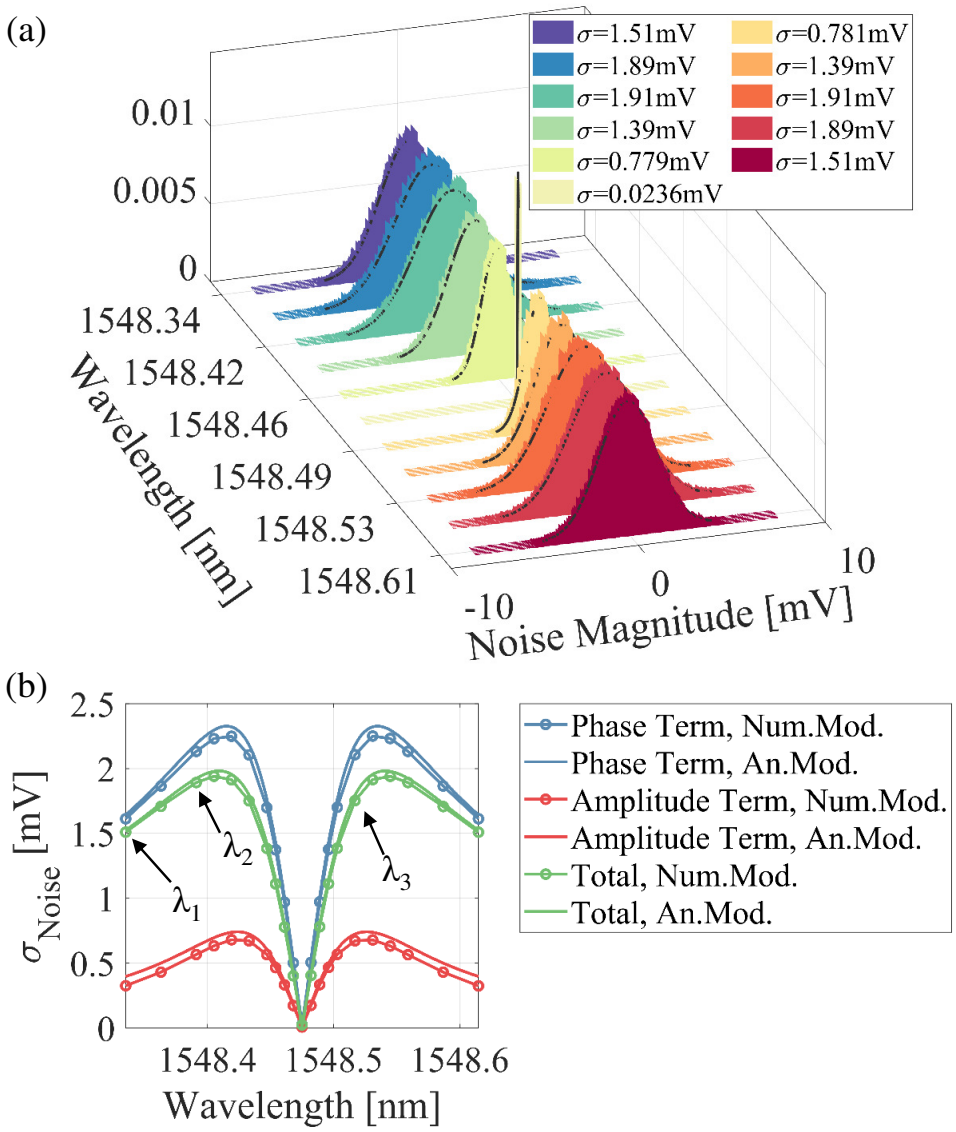

Figure 3.2: (a) Histograms of phase noise induced intensity noise for different waveleghts, for laser linewidth of 1 MHz, conversion gain of 150 V/W and input power of 2.2 dBm, conditions equivalent to the experiment with 6 dB output power of the DFB laser; Gaussian fits are overlayed. (b) Phase noise induced intensity noise standard deviation vs wavelength: analytical model in solid, and numerical results in lines with markers.

Now, let us focus on spectral properties of phase noise induced intensity noise at the RRM output. The noise power spectral density (PSD) at several carrier to resonance detuning points, indicated by arrows in Figure 3.2(b), is shown in Figure 3.3 (dashed lines, right axis). It follows the shape of the detuning dependent small signal EO S_{21} at the same carrier bias points, as described by Equation 2.25, when the loss modulation is disregarded (i.e. $\overline{\delta\omega_0} = \delta\omega_0$ in Equation 2.25 is real). The EO S_{21} curves are shown in solid lines, with their scale indicated on the right axes of

Figure 3.3. The EO S_{21} is normalized to correspond to the variance of the output signal, divided by the squared average optical power at the resonator output, when the device is driven by 2 V peak-to-peak signal, a default setup for our experiments. This normalization is chosen to facilitate a comparison with the noise magnitude, which is given as a standard deviation normalized to squared optical power, as per standard definition for RIN. Interestingly, the signal-to-noise ratio limited by this noise source is independent of detuning and frequency, if the RRM is used as a standalone amplitude modulator and the laser follows a Wiener process. In the RA-MZM structure, however, RRMs serve as phase modulators, so in this context this effect is used purely to illustrate the coincidence of the induced intensity noise PSD and RRM's EO S_{21}.

Following a similar derivation as for the variance of this noise source, the observed spectral behavior can be explained as follows. The phase increment $\delta\varphi$ occurring in the input field in the bus waveguide is subjected to the filtering by the resonator, with a step response proportional to $exp(-t/\tau_a - i(\omega-\omega_0)t)$. Let us assume a phase noise component at the offset frequency from the carrier ω_{off}, oscillating as $exp(i\omega_{off}t)$. The phase increments are proportional to the derivative $i\omega_{off}exp(i\omega_{off}t)$, so that the resulting filtered response is proportional to

$$\begin{aligned} &\int e^{-t/\tau_a - i(\omega-\omega_0)t} e^{i\omega_{off}t} i\omega_{off} dt \\ &\propto \frac{i\tau_a\omega_{off}}{1+i\tau_a(\omega-\omega_0-\omega_{off})}. \end{aligned} \tag{3.15}$$

Since for a Wiener process the noise PSD scales as $1/\omega_{off}^2$, the overall single-sided PSD of the induced intensity noise scales as

$$\propto \frac{1}{1+\tau_a^2(\omega-\omega_0-\omega_{off})^2} + \frac{1}{1+\tau_a^2(\omega-\omega_0+\omega_{off})^2}, \tag{3.16}$$

featuring the expected enhancement at noise frequencies equal to the frequency offset between the carrier and the ring resonance, equivalent to the EO S_{21} of the modulator.

There is an intuitive, complementary way of reaching the above conclusion. We first note that the Wiener process features a white frequency noise spectrum, with a PSD which is constant for all frequencies. Furthermore, regardless of whether the optical carrier frequency or the RRM resonant frequency are dithered around the steady state value, the power fluctuations at the output of the RRM are identical in both cases. Since the carrier phase noise can be modeled by the former and the amplitude modulation by the latter, the equivalence between the PSD of the induced intensity noise and the S_{21} directly follows. This interpretation is particularly useful when the optical source does not follow the Wiener process. In this case, the PSD

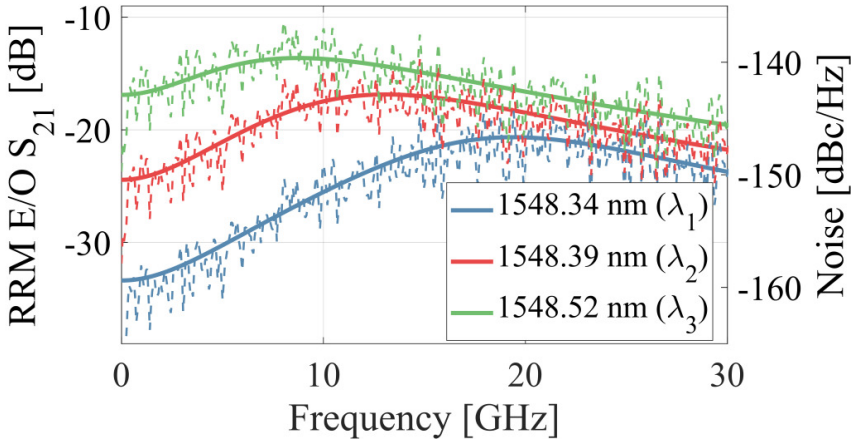

Figure 3.3: Small signal S_{21} (left axis, solid lines) and PSD of the laser phase noise induced intensity noise at the resonator output (right axis, dashed lines) for different carrier to ring resonance detunings. For all curves the enhancement occurs at the frequencies close to the detuning itself.

of the induced intensity noise will be shaped both by the initial frequency noise PSD and the RRM's S_{21}.

We further confirmed the validity of this interpretation by verifying that the simulated noise, in dBc/Hz, is below the calculated S_{21} by an amount

$$\left| 10log_{10}\left(\frac{h_0\lambda_0^2}{\nu_0^2\xi^2V_{rms}^2}\right)\right|, \tag{3.17}$$

where h_0 is the frequency noise PSD given as $\Delta\nu/\pi$ for the Wiener process, λ_0 and ν_0 are the carrier wavelength and frequency, ξ is the high-speed wavelength tuning efficiency of the RRM (in pm/V), and $V_{rms} = V_{pp}/2\sqrt{2}$ is the drive voltage expressed as a root-mean-square value.

3.3 Link transmission: measurements and modeling

In this section we describe a set of experiments specifically designed to test the validity of the derived analytical predictions for the laser phase to intensity noise conversion at the resonant modulator output. For this, we opt for transmission of directly detected SSB-OFDM data, modulated onto the optical carrier using an RA-MZM. In an otherwise identical link configuration, we perform the experiments using two different optical sources that mainly differ in their noise characteristics. Comparison between the two sets of experiments lets us determine the influence that laser noise has on signal quality at different modulator bias points.

Moreover, we numerically model these two link scenarios. Here, the influence of the phase to intensity noise conversion is included through our analytical model at the link end. Direct comparison of simulated signal and noise properties with the experimental results offers thus an insight into the validity of our analytical model.

This section is structured as follows. In Subsection 3.3.1 we describe in detail the experimental setup. Subsection 3.3.2 covers the methodology used for data post-processing and extraction of relevant signal quality metrics that facilitate the comparison of experimental with the modeled results. Subsection 3.3.3 summarizes models of all the constituting components used in the numerical link simulations. Lastly, comparison of experimental and simulated data and the results' discussion follows in Subsection 3.3.4.

3.3.1 Measurement setup

The block diagram of the measurement setup is shown in Figure 3.4(a). The Si chip that contains the three-channel RA-SSB modulator is mounted on and wirebonded to a printed circuit board (PCB). This eases the application of modulating signals, as well as DC signals used for thermal tuning of on-chip components (Figure 3.4(b)). For optical I/O, a fiber array is aligned to on-chip GCs and permanently attached to the chip (Figure 3.4(c)). The chip is not externally thermally stabilized during the measurements.

The OFDM signals are generated using a 512 elements IFFT, in which one half of the sub-carriers is loaded with zeroes to create a single-sideband signal. An additional gap of 20 sub-carriers is introduced next to the optical carrier, keeping the signal out of the region most affected by sub-carrier interference [50]. In a link scenario including semiconductor MLLs, for example, this gap would prove doubly beneficial, since it also offsets the signal spectrum away from the low frequency region where laser RIN dominates [88]. Moreover, when optical signals are amplified by a semiconductor optical amplifier (SOA), the signal is displaced from the range

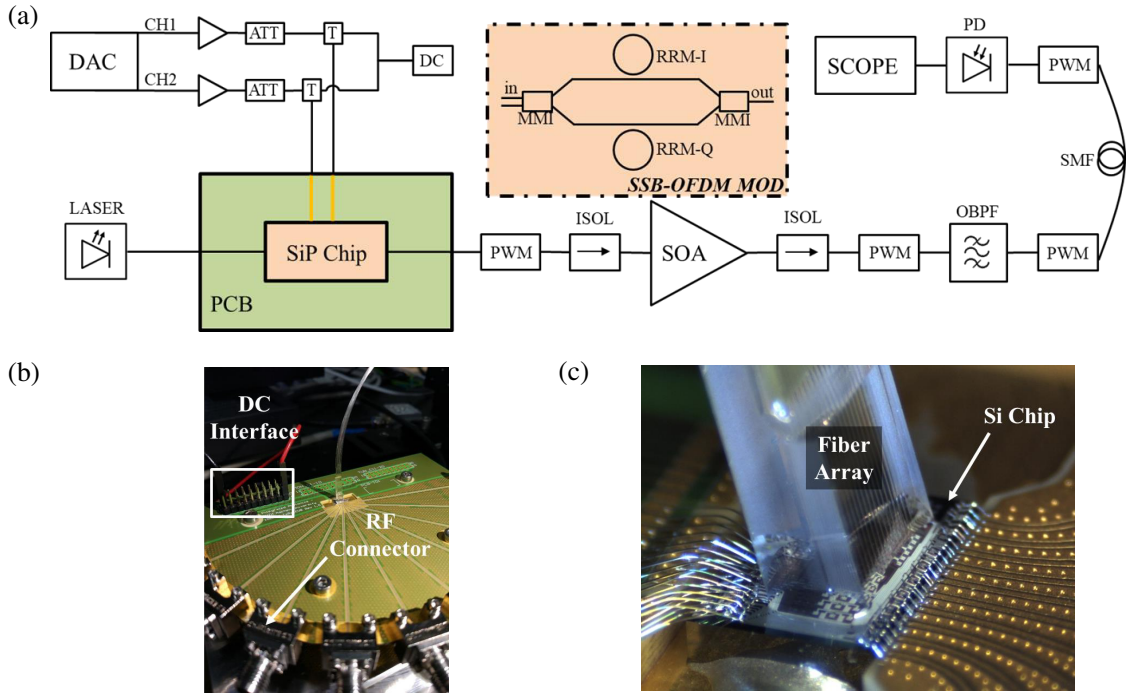

Figure 3.4: (a) Measurement setup; the inset shows a single-channel RRM assisted SSB modulator; (b) Fan-out PCB with the DC and RF interfaces; (c) Si chip mounted and wire-bonded to the fan-out PCB with the attached fiber array for optical input-output.

of frequencies in which SOA induced signal distortion is the worst [89]. The guard band is followed by 100 sub-carriers, each loaded with randomly generated QPSK symbols, starting from a $2^{15}-1$ bits long pseudo-random bit sequence (PRBS). Based on the bandwidth limitation of the RRMs, we allocated the frequency band up to 16 GHz for the transmission of up to 256 subcarriers spaced by 62.5 MHz. Consequently, the signal covers the frequency span from 1.25 to 7.5 GHz for the 100 loaded sub-carriers investigated in this section. A block of 128 OFDM symbols, each appended with a 3% CP, is then transmitted through the link. It should be mentioned that in these experiments the overall throughput was not maximized, since their main purpose was to examine the noise present in the system. We extend the performance to higher limits in the full capacity experiments reported in the next chapter. The modulating signals are then upsampled, converted by a 2-channel DAC, and amplified by fixed gain high-speed amplifiers. To adjust the amplifier gain, a 6-dB attenuator (ATT) is added at the amplifier output in both signal paths. A -1.5 V DC bias is added to the AC signals using bias-tees, before finally routing them to the PCB. Ultimately, with the loss of the PCB traces included, ~2 V peak-to-peak (Vpp) signals reach the RRMs.

The real part of the OFDM signal is routed to the RRM in one RA-MZI arm, while

Component	Model	Parameter	Value
RRM		Radius	$10.1\mu m$
		Tuning Efficiency	13.5 pm/V
		Loaded Quality Factor	11000
		Resonance ER	6.3 dB
DFB Laser	Thorlabs PRO8	Linewidth	1 MHz
		Power Range	3 to 13 dBm
ECL Laser	Keysight 81642A	Linewidth	100 kHz
		Maximum Power	6 dBm
SOA	Thorlabs S7FC1013S	Gain	30.5 dB
		Noise Figure	7 dB
		Ouput Saturation Power	14.4 dBm
		Carrier Lifetime	0.17 ps
Optical Bandpass Filter	JDSU VCF050	IL	1.9 dB
		1 dB Optical Bandwidth	24 GHz
		3 dB Optical Bandwidth	40 GHz
Photodetector	Finisar XPRV2021(A)	3 dB Bandwidth	40 GHz
		Conversion Gain	150 V/W
		Input Referred Noise	30 pA/$Hz^{-1/2}$
		Input Power Range	-10 to 3 dBm
		Responsivity	0.64 A/W
DAC	Socionext Corellian DK	Sampling Rate	96 GS/s
		Ouput Voltage Swing	0.3 V_{pp}
RF Amplifier	SHF 807	Gain	24 dB
		3 dB Bandwidth	40 GHz
PCB & Connector		IL @ 10 GHz	2.8 dB
GC		IL @ Max. Transmission	4.1 dB
Fiber	Corning SMF-28	Dispersion	17 ps/nm/km
		Loss @ 10 km	3.3 dB
		Loss @ 20 km	5.2 dB
Oscilloscope	Agilent DSA-X 92004A	Bandwidth	21 GHz
		Sampling Rate	80 GS/s

Table 3.1: Link component specifications

the imaginary part is routed to the RRM in the other arm, thus creating an SSB signal in the optical domain. The optical signal from the chip output is further routed to a single polarization SOA, with isolators (ISOLs) inserted both at the input and output of the amplifier to suppress back-reflections. The out-of-band amplified spontaneous emission (ASE) is removed by means of an optical bandpass filter (OBPF) placed after the SOA (40 GHz -3dB optical passband). The signal is converted back to the electrical domain using a commercial high-speed photodetector (PD) and captured by a real-time sampling oscilloscope (SCOPE). The optical power levels are moni-

tored by in-line power meters (PWMs) at the output of the chip, SOA output, filter output, as well as after propagation through standard single mode fiber (SMF) in long distance transmission experiments. The monitor at the SOA output is also used as an attenuator, reducing the amplified signal by 11.6 dB, to keep the power reaching the PD within its operating bounds (-10 to 3 dBm). The relevant component parameters are summarized in Table 3.1.

3.3.2 Measurement and data post-processing methodology

To determine the influence of laser noise, primarily frequency/phase noise, on data transmission in the previously described link we perform the experiments in two link configurations, with two different lasers as optical sources. Moreover, for both link scenarios, the experiment is repeated for different laser output powers and varying optical carrier to ring resonance detunings. This allows us to better benchmark our models.

The first source we employ is a laboratory-grade tunable external cavity laser (Keysight Technologies 81642A), denoted as ECL in the following. It exhibits RIN in the order of -150 dBc/Hz for all the investigated power levels and a linewidth in the order of 100 kHz. The second is a DFB laser module (Thorlabs PRO8) intended for WDM applications. It features a higher, pump current dependent RIN, as well as a higher linewidth in the order of 1 MHz. The RIN measurements for both sources are shown in Figure 3.5 for the power levels of interest. The experiments in back-to-back (BtB) configuration are performed for varying laser output power levels, namely -3, 0, 3 and 6 dBm. The experiments with the DFB for 0 and -3 dBm were both performed with a 3 dBm laser power and additional external attenuation, as the laser output power could not be set below 3 dBm. Therefore, the RIN PSD shown for the 3 dBm DFB output power (blue line in Figure 3.5) is also representative for these other measurements.

Synchronization and equalization

After the data has been captured by the oscilloscope, further post-processing is necessary to extract relevant signal quality metrics. To describe the analog-like, time-domain OFDM signal prior to demodulation we use the standard deviation of the average received signal as a measure of the signal strength. To construct this final signal, we find the mean value of total of 11 signal traces recorded by the sampling oscilloscope. The noise traces are then calculated as a difference between the recorded and averaged signals. Similarly to the signal strength, the noise is described in terms of its standard deviation.

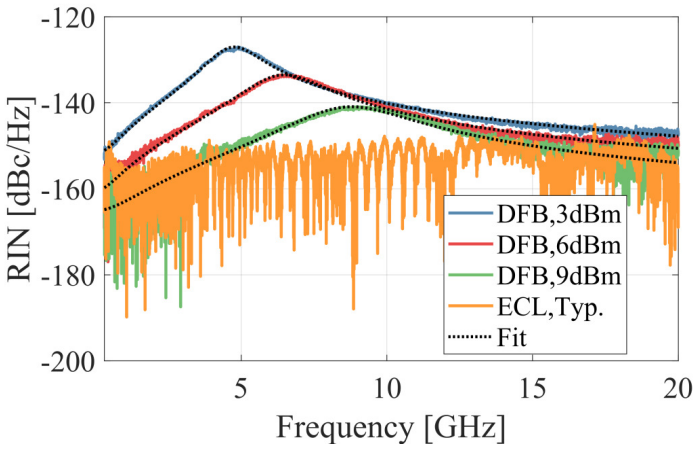

Figure 3.5: Measurements of RIN PSD. DFB measurements are overlaid with fits according to Eq. 3.3.3, with fitting parameters listed in Table 3.2

In addition to sampling at the specified rate (see Table 3.1), the oscilloscope also performs a 16-point sinc interpolation of the received data, leading to a total of $2097151 \cdot 16 = 33554416$ recorded data points. To directly compare it with the transmitted sequence, the received data is first resampled. Once their sampling rates are identical and equal to 32 GS/s, the transmitted and received sequences are cross-correlated for synchronization. The result of this cross-correlation features a set of peaks, marking the starting positions of the individual traces in the full recorded sequence. For a good synchronization that does not introduce additional data distortion, it is often necessary to upsample both of the sequences 2-6 times. This additionally increases the data-processing time, thus limiting the number of symbols we can send/receive and still maintain reasonable post-processing computational times.

For illustration, we look at the results of an experiment in which the DFB is used as the optical source, its output power is set to 6 dBm and information is loaded onto the lower frequency sideband. A single received time-domain OFDM symbol (symbol 64 out of 128) is shown for three different carrier to ring resonance detuning points in Figure 3.6(b). The real part of the corresponding initial OFDM symbol, before DAC conversion, is overlaid with received signals (black dashed lines in all subplots) for comparison. The initial signal amplitude is scaled between -1 and 1, as per the requirement posed on the input signal of the DAC used in the setup. The exact detuning points are labeled with colored markers in Figure 3.6(a), which shows the measured power at the chip output versus wavelength. The same measurement configurations are further used for illustrative purposes in the rest of this subsection.

Given the memory depth of the oscilloscope used here, as well as the length of the initial sequence, we in the end record 11 traces that can be used for further analysis.

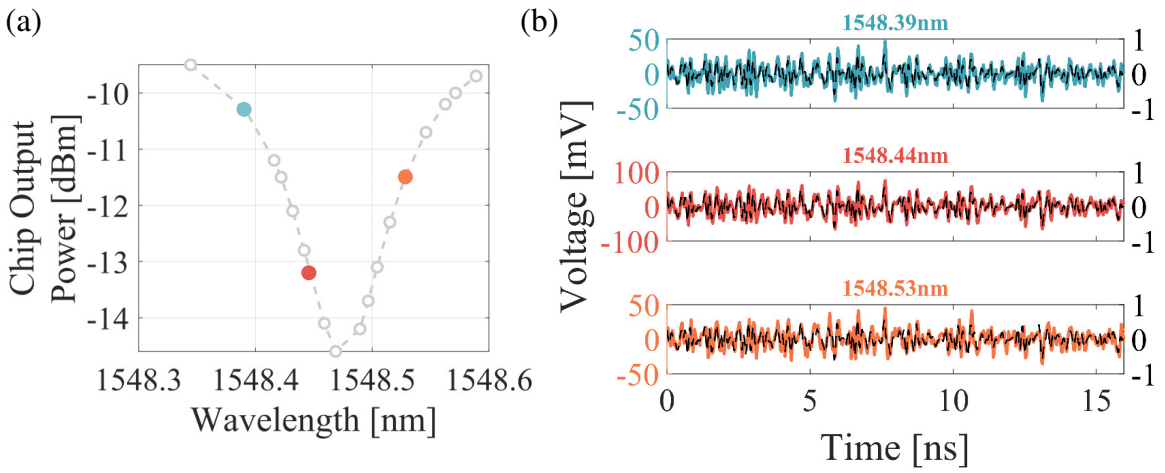

Figure 3.6: (a) Power at chip output; colored markers show carrier bias points used for illustration in the following panel and the rest of the subsection; (b) received symbol 64 in time domain for the three detunings, in an experiment with the DFB as the optical source, 6 dBm ouput power setting and LSB loaded transmission; the received symbols are overlaid with the real part of the corresponding transmitted SSB symbol (black dashed line)

The average signal is then calculated as the mean of these 11 traces, while the noise represents the difference between the recorded traces and the average signal. Figure 3.7 shows the evolution of the average signal and noise standard deviation with the number of averaged traces (M). It can be seen that the standard deviation of noise has a growing tendency, plateauing for a very large number of traces. Therefore, the resulting noise standard deviation calculated for $M = 11$ is additionally scaled to represent its asymptotic value, σ_∞, as

$$\sigma_\infty = \frac{\sigma_M}{\sqrt{1-\frac{1}{M}}} = \sqrt{\frac{11}{10}}\sigma_{11}, \tag{3.18}$$

which is the value reported in all the noise descriptions further on in this work.

Once accurately identified through synchronization, the individual traces are split into constituting OFDM symbols, and the CP is removed from each of them. Since in the OFDM scheme the information symbols are encoded onto individual frequency sub-carriers, for further demodulation and processing we move to the spectral domain. As a reference signal we use again the real part of the OFDM signal before the DAC conversion and we focus on a single symbol in the sequence (here, once again, symbol 64 out of 128). Spectra of the chosen symbol in the average received sequences are shown in Figure 3.8(a)-(c) for the detuning points marked in Figure 3.6, overlaid with the spectrum of the corresponding symbol in the reference sequence (black dashed lines).

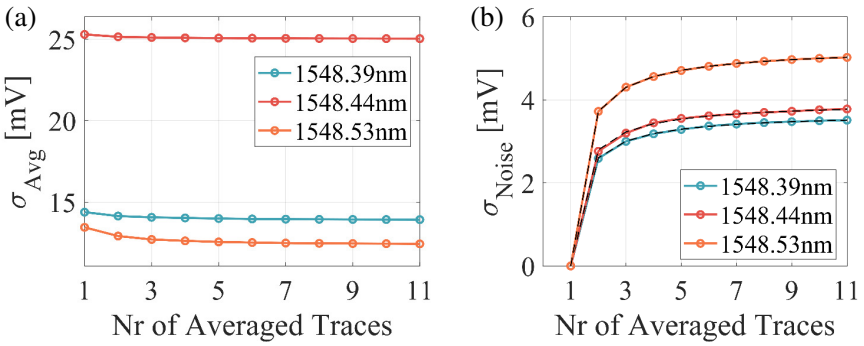

Figure 3.7: Effect of number of averaged traces on signal metrics (a) std.dev. of the average signal and (b) noise at the link end versus the number averaged traces

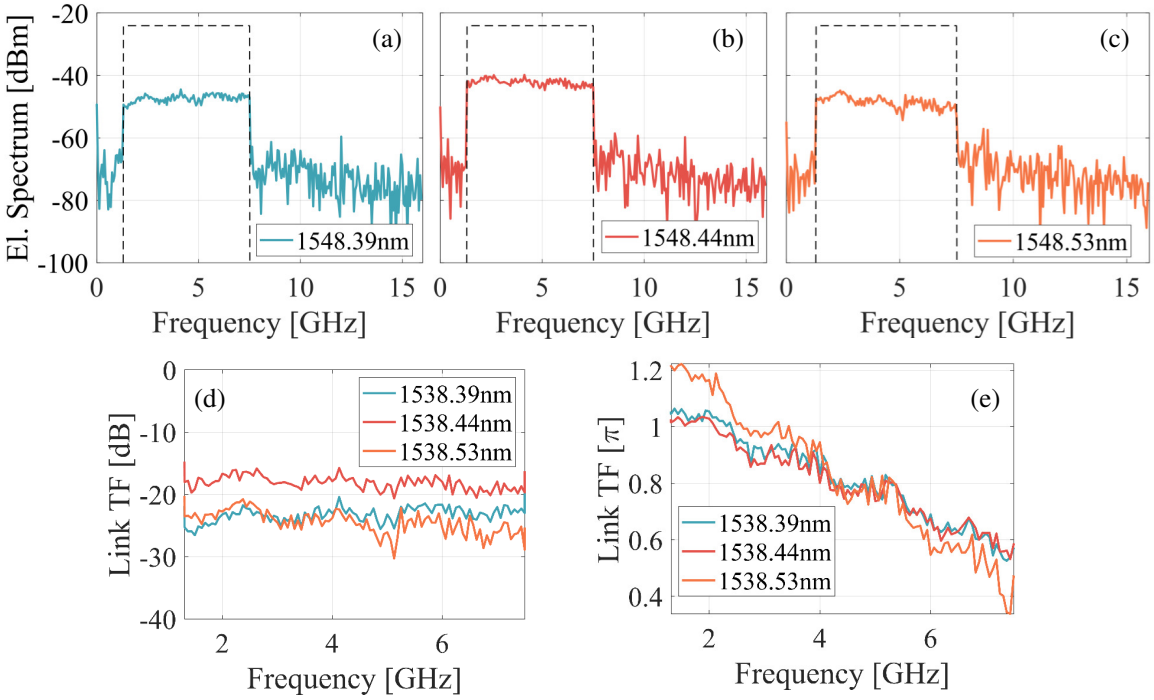

Figure 3.8: Received electrical spectra for different optical carrier biases

The ratio of the spectra of the average received and the corresponding reference symbol represents the link transfer function at the given detuning. It can therefore be used for single-tap equalization of all the transmitted OFDM symbols. Through this, the information symbols modulated onto each sub-carrier are rotated and rescaled according to the value of the link transfer function at that frequency. The magnitude and phase link transfer functions at the same detuning points are shown in Figure 3.8(d) and (e), respectively. As an example, an unequalized (left panel) and single-tap equalized (right panel) constellation diagrams for the carrier biased at 1538.44 nm are shown in Figure 3.9.

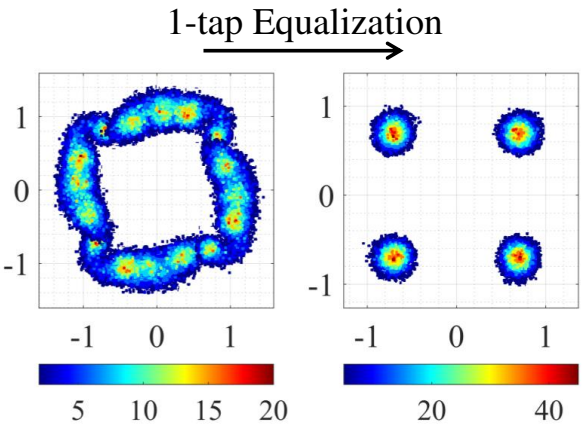

Figure 3.9: The unequalized (left panel) and 1-tap equalized (right panel) constellation diagrams for optical carrier biased at 1538.44 nm

Signal quality metrics

Once the data is demodulated and equalized, we quantify the quality of transmission using two main metrics: bit error ratio (BER) and error vector magnitude (EVM).

BER is the fundamental signal quality metric which does not depend on the type of signal impairment and its low value is therefore the most clear indicator of the good system performance. However, in case of complex modulation signals that require post-processing, BER might not be practical, since it calls for long acquisition times and large memory depth of the recording device. This is due to the fact that a large number of errors must be recorded for a high confidence in the results.

We therefore sometimes turn to EVM for the quantification of our complex information symbols. The EVM, describing the deviation of the analyzed symbols from an ideal constellation diagram of the given modulation format, is defined as

$$EVM_m = \frac{\sigma_{error}}{|E_{t,m}|} = \frac{1}{|E_{t,m}|}\sqrt{\frac{1}{N}\sum_{i=1}^{N}|E_{r,i} - E_{t,i}|^2}, \tag{3.19}$$

where N is the number of sent/received symbols, E_r is the received and E_t the ideal transmitted symbol; $E_{t,m}$ is the longest ideal constellation vector and it serves for normalization [90].

Detuning mapping

Furthermore, when a high power is incident to the RRMs, thermal effects start to play a role. The closer the carrier biasing point is to the resonance, the more optical power is stored inside of the rings. This leads to the effect of self-heating [91],

where the refractive index of Si changes with the increased temperature and offsets the resonance towards the longer wavelengths (Figure 3.10(a)).

To correctly identify the exact detuning we compare the extinction at the given wavelength at higher input powers with the extinction at the lower input powers, where little to no thermal distortion is present, and apply detuning mapping accordingly. This is illustrated in Figure 3.10(b), which shows the recorded power at the chip output for the laser output power of -3 dBm (solid green line) along with the 6 dBm case, for which the resonance shape is slightly distorted (solid red line). The mapped resonance for the higher power setting is also shown in dashed red line. This phenomenon, however, is of low-speed nature and does not penalize the high-speed data transmission [92].

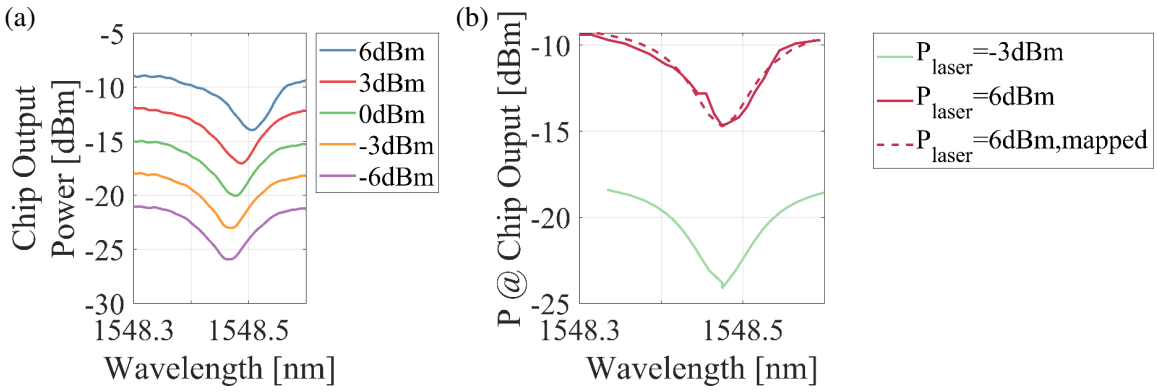

Figure 3.10: (a) Wavelength scans for different laser output power levels; (b) Illustration of detuning mapping at higher RRM input optical powers: resonance shape and extinction ratio at a given wavelength at low powers is used as the reference for mapping.

3.3.3 Link model

In addition to experiments, we perform numerical simulations of the described link, in which we include the laser phase noise to intensity noise conversion by the resonant modulators through our analytical model. Here we introduce the models used to describe the most important link components.

RA-MZM

The modulator behaviour is simulated by two blocks. The RC response of the diode is accounted for by a single-pole filter, whereas, as previously described, the resulting RRM modulation is simulated using the dynamic resonator equation (Equation 3.1). Here, the resonance frequency and photon lifetime are time-dependent and

change according to the modulating signal (Figure 3.11(b) and (c)). Modeled RRM transmission is shown in Figure 3.11(a).

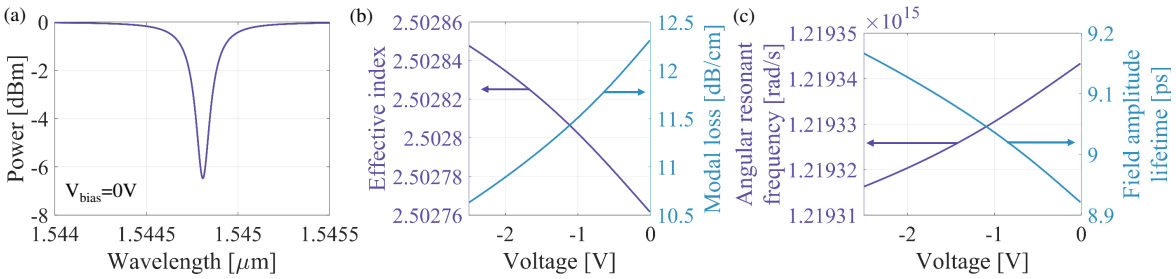

Figure 3.11: Properties of the modeled RRM: (a) Transfer function at 0 V bias voltage; (b) Modal effective index (left axis, in purple) and loss (right axis, in blue) for different PN bias voltages. (c) Angular resonant frequency (left axis, in purple) and field amplitude lifetime, τ_a, (right axis, in blue) for different PN bias voltages.

Laser model

In semiconductor lasers random photon and carrier recombination and generation processes cause fluctuations in the laser output power and lasing wavelength. More specifically, variations in photon density primarily contribute to the relative intensity noise (RIN) of the laser, whereas the carrier density fluctuations are responsible for the baseline laser frequency noise. Both of these noise sources are included in our numerical model of the laser as described in the following.

The optical power at the laser output can be represented as

$$P(t) = P_0 + \delta P(t), \tag{3.20}$$

where P_0 denotes the average value and $\delta P(t)$ the fluctuations with zero mean. RIN is defined as

$$RIN \equiv \frac{\langle \delta P(t)^2 \rangle}{P_0^2}. \tag{3.21}$$

In order to quantify the output power fluctuations we will look at the frequency domain. Relationship between the time and frequency domain variables is defined through Fourier transform pairs

$$\delta P(t) = \frac{1}{2\pi} \int_{-\infty}^{+\infty} \delta P(\omega) e^{i\omega t} d\omega \tag{3.22}$$

$$\delta P(\omega) = \int_{-\infty}^{+\infty} \delta P(t) e^{-i\omega t} dt. \tag{3.23}$$

Spectral density of noise is then defined as

$$\frac{RIN}{\Delta f} = \frac{2S_{\delta P}(\omega)}{P_0^2}, \tag{3.24}$$

where

$$S_{\delta P}(\omega) = \frac{1}{2\pi}\int_{-\infty}^{+\infty} \langle \delta P(\omega)\delta P(\omega')\rangle d\omega'. \tag{3.25}$$

Here, $\langle\rangle$ represents the statistical average, equivalent to the time average for stationary, ergodic processes. Δf is the bandwidth of the measurement apparatus, or in the case of our numerical model, simulation bandwidth.

In semiconductor lasers RIN spectral density takes the shape [93]

$$\frac{RIN}{\Delta f} = 16\pi\Gamma R'_{sp}/(4\pi N_p)\frac{1/\tau_{\Delta N}^2+\omega^2}{\omega_{ro}^4}|H(\omega)|^2 + \frac{2h\nu}{P_0}, \tag{3.26}$$

where

$$H(\omega) = \frac{\omega_{ro}^2}{\omega_{ro}^2-\omega^2+i\omega\gamma} \tag{3.27}$$

is called the modulation transfer function. $\tau_{\Delta N}$ is the differential carrier lifetime, related to spontaneous emission and non-radiative recombination processes, ω_{ro} the angular relaxation oscillation frequency, and γ the damping factor, proportional to the cavity photon lifetime. The second term corresponds to the shot noise level, the standard quantum limit for the minimum RIN of the laser, where h is the Planck's constant and ν the photon frequency. This expression represent the limit case for low powers, but it can, nevertheless, be used for moderate to high power levels with reasonable accuracy. It shows that the noise is amplified near the relaxation oscillation frequency, reaching its maximum at ω_{ro}.

In our considered link scenarios, laser RIN values are taken from the characterization measurements (Figure 3.5). The PSD of the DFB RIN is fitted using the model from [94], with the fitting function for the RIN PSD given as

$$RIN(\omega) = \frac{RZ^2(1+A\omega^2)}{Z^2+(Y^2-2Z)\omega^2+\omega^4}, \tag{3.28}$$

where ω is the baseband angular frequency. The fitting parameters R, Z, A and Y are summarized in Table 3.2 for all relevant DFB output power levels.

The Z parameter corresponds to $(2\pi f_{ro})^2$, where the relaxation oscillation frequency f_{ro} takes the value of 4.76, 6.48 and 8.79 GHz for DFB output power of 3, 6 and 9 dBm, respectively.

The frequency noise in semiconductor lasers has two main contributing factors (1) the electrical carrier noise, which causes change of the refractive index and therefore of the lasing frequency and (2) the noise of photons spontaneously emitted into

P [dBm]	$10log_{10}(R)$	Z	A	Y
3	-152	$8.958{\cdot}10^{20}$	$4.417 \cdot 10^{-20}$	$1.109{\cdot}10^{10}$
6	-160	$1.656{\cdot}10^{21}$	$4.514 \cdot 10^{-20}$	$1.595{\cdot}10^{10}$
9	-165	$3.051{\cdot}10^{21}$	$1.503 \cdot 10^{-20}$	$2.342{\cdot}10^{10}$

Table 3.2: Fitting parameters for DFB RIN PSD

the lasing mode, also called the inherent frequency noise. The frequency noise spectral density, $S_\nu(\omega)$ is given by

$$S_\nu(\omega) = \frac{1}{2\pi}\Delta\nu_{ST} \cdot \left(1 + \alpha_H^2 |H(\omega)|^2\right), \tag{3.29}$$

where $(\Delta\nu)_{ST} = \Gamma R'_{sp}/(4\pi N_p)$ is the modified Shawlow-Townes linewidth, corresponding to the spontaneous emission term, with Γ the confinement factor marking the overlap of the lasing optical mode with the active region, R'_{sp} the rate of spontaneous emission into the lasing mode, and N_p the photon density inside of the laser cavity. α_H is the linewidth broadening factor (or Henry parameter) which relates the rate of change of the real (n) and imaginary (n_i) parts of the active medium's refractive index with the changing carrier concentration (N) [95]

$$\alpha_H \equiv -\frac{dn/dN}{dn_i/dN}. \tag{3.30}$$

As can be seen from Equation 3.29, the fraction of the overall frequency noise related to spontaneous emission has a constant PSD. These inherent "baseline" laser frequency fluctuations are therefore assumed to follow a Wiener process and introduced through our analytical model at the end of the link. For proper scaling, power levels are adjusted according to laser output power, SOA gain and overall link losses.

However, a substantial part of the total laser frequency noise has its origin in the variation of electrical carrier densities in the active region, encompassed in the linewidth broadening factor (α_H)[95]. In part, these carrier variations are caused by the photon density fluctuations that ultimately constitute RIN at the laser output. Therefore, a correlation exists between RIN and a portion of frequency noise, which should be accounted for when combining different noise sources to calculate the overall system noise. To do this properly, we focus on the expressions that describe laser RIN and frequency noise spectra. According to Equation 3.26 RIN spectrum scales as $(1/\tau_{\Delta N} + i\omega)H(\omega)$. On the other hand, Equation 3.29 indicates that the frequency noise spectrum is proportional to $H(\omega)$. This lets us conclude that RIN and frequency noise resulting from RIN are essentially in quadrature for noise frequencies above $1/(2\pi\tau_{\Delta N})$, apart from the small phase error $atan(1/(\tau_{\Delta N}\omega_{off}))$. The differential carrier lifetime $\tau_{\Delta N}$ is in the order of 1.6 ns for typical edge emitting

semiconductor lasers (see e.g. Table 5.1 in [93]), leading to $1/(2\pi\tau_{\Delta N}) \sim 100\ MHz$. Since this is well below the 20-sub-carrier gap used in this work (1.25 GHz) and generally quite low, RIN and frequency noise can be assumed to be in quadrature. At the same time, the intensity noise generated by the RRM through phase noise conversion is proportional to phase noise increments, i.e. to the frequency noise itself. Therefore, the intensity noise induced by the RIN-correlated frequency noise is also in quadrature with RIN. Hence, despite the correlation, the two add as a sum of variances from the perspective of system-level modeling. Consequently, to the first order, we may expect that lumping all the frequency/phase noise into the Wiener process with parameters given by the (broadened) laser linewidth yields reasonable results.

However, the Wiener process only correctly reflects the frequency noise levels at low frequencies. Increase of the frequency noise at the relaxation oscillation frequency is not taken into account with this approach. Moreover, the assumption that the RRM converts the frequency noise into amplitude noise without a phase delay is no longer correct at increased noise frequencies. As described in Section 3.2, the spectral dependence of the frequency to intensity noise conversion is identical to the S_{21} of the RRM operated as a standalone amplitude modulator, which features a peaking response. The RRM, therefore, introduces a phase delay of $\sim \pi/4$ for the noise frequency of $f_{off} \sim 1/(2\pi\tau_a) = 8.7\ GHz$. Consequently, at the relaxation oscillation frequency at which the laser RIN reaches its maximum (between 4.6 and 8.8 GHz for output power levels ranging from 3 to 9 dBm, in our experiments), RIN and the intensity noise resulting from RRM-conversion of RIN-correlated frequency noise can no longer be added as a sum of variances.

In order to account for this, RIN-correlated frequency noise in the vicinity of the relaxation oscillation frequency is included into our model by introducing another frequency noise term at the output of the laser. Its PSD is obtained from the RIN spectrum by multiplying it by a constant proportionality factor $5.8{\cdot}10^{19}\ Hz^2$, obtained from a best match to the experimental results. Moreover, a Hilbert transform is applied to the resulting frequency noise in order to induce a 90-degree phase delay relative to RIN, in line with the previous analysis. This additional phase noise term is then fed through the numerical model of the RRM.

What might be striking is that we are seemingly including the RIN-correlated phase/frequency noise at low noise frequencies twice in our model: once by the linewidth broadening factor and second time in the newly added phase noise term. However, this proves not to be the case after closer inspection. Namely, the conversion factor between RIN and its correlated frequency noise PSD is, in reality, frequency dependent. This comes from a zero in the RIN spectrum, making the conversion factor about $\omega_{ro}^2\tau_{\Delta N}^2$ larger at DC than at the relaxation oscillation frequency. This dependency is, however, not taken into account when the additional

phase noise term is introduced into our numerical model. Here, the proportionality factor is kept constant for all noise frequencies. The RIN, which is much lower close to DC, does not significantly contribute to the low-frequency phase noise and does not, therefore, additionally influence the laser linewidth.

Semiconductor optical amplifier

Semiconductor optical amplifiers (SOAs) use electrically pumped semiconductor gain medium for light amplification. The carrier density, and therefore the gain of this medium, is coupled to the optical power present in the laser cavity as given by the following differential equation

$$\frac{dG(t)}{dt} = -\frac{G(t) - G_0}{\tau_c} - \frac{G(t)P_{in}(t)}{P_{sat,in} \cdot \tau_c}, \tag{3.31}$$

where G_0 is the small signal gain at low average input power, τ_c the gain relaxation time constant, and $P_{sat,in}$ the saturation power at the SOA input, defined as the input power at which gain reduces to half its small signal value [96].

The main noise source in SOAs is the broadband amplified spontaneous emission (ASE). The amount of noise introduced by an amplifier is usually specified by the noise figure, which is defined as the ratio of the SNRs at the input and the output of the component

$$F = 10log_{10}\left(\frac{SNR_{in}}{SNR_{out}}\right). \tag{3.32}$$

For SOAs F is always larger than 2, typically around 5 dB. ASE adds distortions both to the amplitude and the phase, which becomes relevant when the amplified signal propagates through dispersive media, such as optical fibers, after amplification and prior to direct detection. This converts part of the phase noise to the amplitude noise, additionally penalizing the signal integrity. For a shot noise limited signal at the amplifier input, the SNR_{in} is given as

$$SNR_{in} = \sqrt{\frac{P_{in}}{2h\nu\Delta f}}. \tag{3.33}$$

Here, Δf represents the bandwidth of the measurement equipment, or in our case the simulation bandwidth and it equals to $1/(2 \cdot dt)$, with dt being the time step used in simulations (here, $\sim 1\ ps$). Following the definitions for the noise figure and the SNR, the standard deviation of the noise at the amplifier output should amount to

$$\sigma_{out} = \sqrt{10^{F/10} \cdot G \cdot 2P_{in}h\nu \cdot \frac{1}{2dt}}. \tag{3.34}$$

In our model, the ASE is added as a random perturbation to the amplitude and the phase of the signal's electric field

$$E_{out}(t) = \sqrt{G} \cdot \Big[E_{in}(t) + E_{ASE}(t) \Big] = \sqrt{G} \cdot \Big[E_{in}(t) + B \cdot (F_1(t) + i \cdot F_2(t)) \Big], \quad (3.35)$$

where the electric fields are scaled such that their amplitude squared represents the power, and $F_{1,2}(t)$ are Gaussian random variables with zero mean value and a variance equal to unity.

The SOA output power fluctuation is therefore given as

$$P_{out}(t) \approx G \cdot \Big[P_{in}(t) + 2Re\Big\{ E_{in}(t) \cdot E_{ASE}(t) \Big\} \Big]. \quad (3.36)$$

Here, we neglect the ASE-ASE beat tone contribution to the overall noise. From this, in order for the standard deviation of the output power to satisfy Equation 3.34, factor B in the ASE field definition should equal to

$$B = \sqrt{\frac{1}{4} \cdot 10^{F/10} \cdot 2h\nu \cdot \frac{1}{2dt}}. \quad (3.37)$$

Since they rely on a semiconductor gain medium for amplification, most of the phenomena encountered in semiconductor lasers and described in the previous section is also present in SOAs. One of these is the Henry parameters that couples the change in the carrier density to the change of the refractive index of the medium. For a complete model of the amplifier this effect should be taken into account. However, we primarily base our model of the SOA on Equation 3.31.

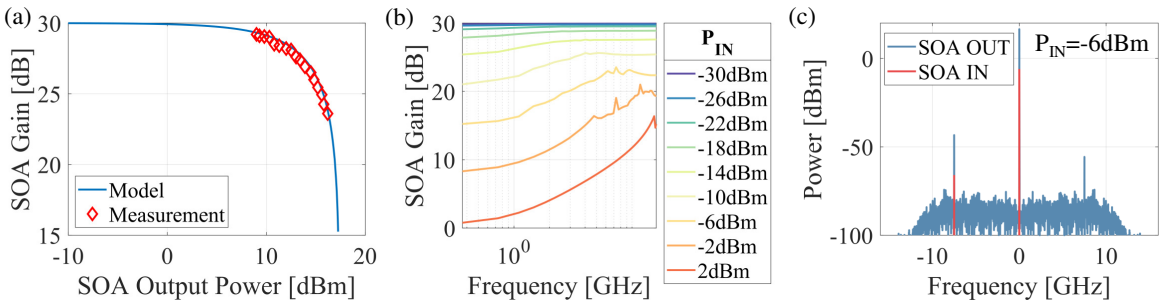

Figure 3.12: (a) Measured (in red) and modeled (in blue) gain saturation curve of the SOA; (b) Modeled gain dependence on frequency for different SOA input optical powers; (c) Modeled field spectrum at the input (in red) and output (in blue) of the SOA at -6 dBm input power; emergence of the initially suppressed sideband evident.

Moreover, when it is operated close to saturation, SOA shows high-pass behavior dictated by the gain relaxation time constant τ_c. Figure 3.12(a) shows measured (in red) and modeled (in blue) gain saturation curve, for the utilized SOA with the

specifications detailed in Table 3.1. Based on these parameters, modeled gain versus frequency curves are shown for different SOA input powers in Figure 3.12(b).

Regarding nonlinear distortions, four wave mixing (FWM) is of most significance in SOAs. In the SSB transmission studied here, the beating between the optical carrier and the signal sideband creates a modulation of the carrier densities in the gain medium, forming a mirror tone of the signal relative to the optical carrier. An example is shown in Figure 3.12(c), which shows the electric field spectrum at the input (in red) and the output (in blue) of the SOA, when the optical signal of -6 dBm is present at the amplifier input. The emergence of the unwanted sideband can be observed, thus altering the sideband suppression ratio. The quantitative analysis of this phenomenon in our system is studied in more detail in the next chapter.

Optical bandpass filter

Based on the parameters listed in Table 3.1, simulated OBPF transfer function used in the link model is shown in Figure 3.13.

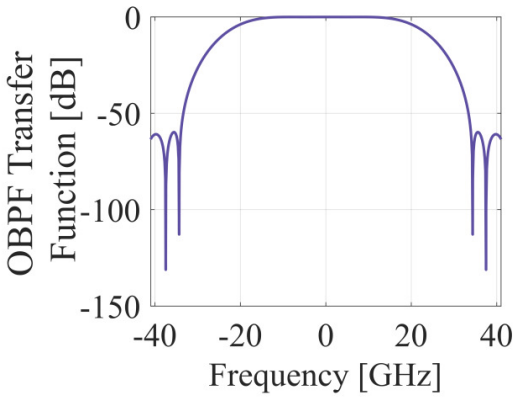

Figure 3.13: Modeled optical bandpass filter transfer function

It should be noted that the phase of the OBPF varies on the flanks of the transmission band. In our case, this happens sufficiently far from the frequencies occupied by the OFDM signal, leaving the signal unaffected.

Optical fiber

Fiber transfer function in frequency domain is given by [97]

$$H_F(f,L) = exp\left(i\frac{D\pi\lambda_0^2 L}{c_0}f^2\right), \tag{3.38}$$

where D is the dispersion coefficient (in $pm/(km\cdot nm)$), λ_0 the carrier wavelength, c the speed of light, L the fiber length and f the offset frequency from the carrier.

Figure 3.14 shows the phase transfer function of a fiber with the dispersion coefficient of 17 ps/km/nm, a typical value for an SMF, as well as for the fiber used in our experiments, for lengths of 10 and 20 km (blue and red lines, respectively). In addition to dispersion, fiber introduces losses, as listed in Table 3.1.

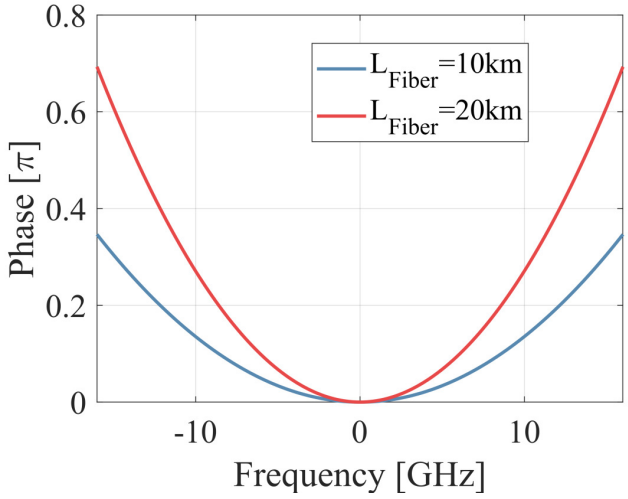

Figure 3.14: Phase transfer function of a 10 (blue line) and 20 (red line) km long dispersive fiber, described by parameters in Table 3.1.

3.3.4 Results and discussion

Finally, we compare the experimentally obtained data with the outputs of our numerical link model. In Figure 3.15, the measurement results are shown along with the model predictions. In sub-panels (a)-(e), the experimental data for the ECL and the DFB are respectively shown by star shaped and circular markers, while solid lines correspond to modeling results.

The overlap of modeled and measured chip output powers ensures that we are comparing the relevant metrics at the same carrier-to-resonance detuning points (Figure 3.15(a)). Similarly, the equivalence of the received power levels confirms that the SOA gain and the overall link insertion losses are modeled properly, as well as that the link conditions have remained unchanged between the two sets of experiments (Figure 3.15(b)). Overlay of the signals' standard deviation, measuring the signal strength, further confirms proper modeling of the RRMs (Figure 3.15(c)). It gives confidence that the modulator properties, such as modulation efficiency and bandwidth, are correctly taken into account in our numerical model.

At the lowest measured laser output power, -3 dBm, the bulk of the noise comes from the SOA's ASE and photoreceiver noise, allowing us to correctly include these

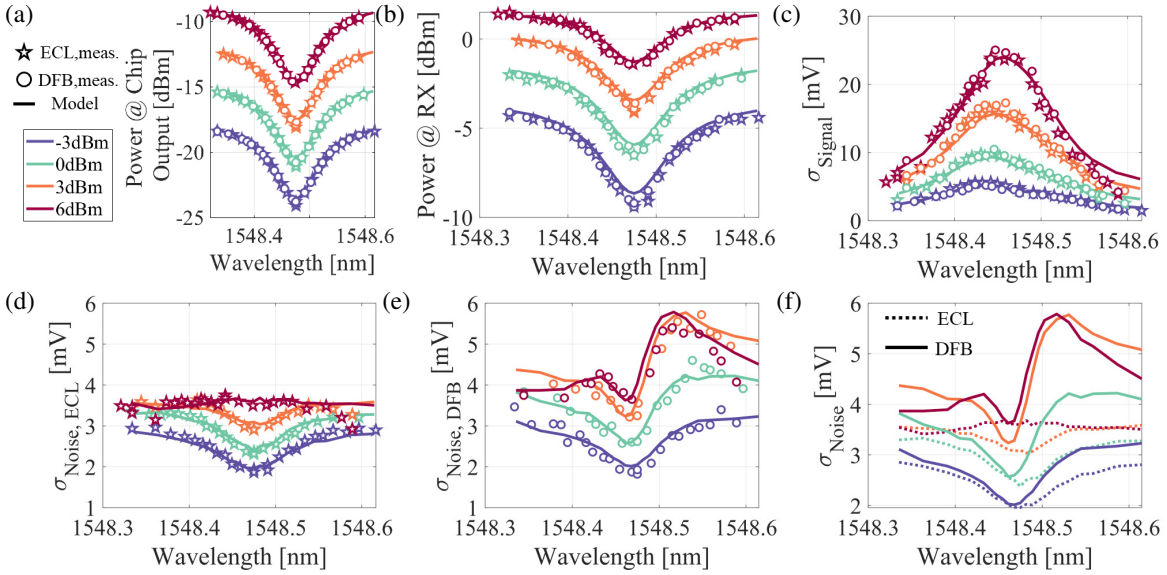

Figure 3.15: Comparison of experimental results with the ECL (star markers) and DFB (circles) with the modeling (solid and dashed lines) for different optical carrier bias points: (a) power at the chip output; (b) power at the receiver; (c) standard deviation of the average signal; measured and modeled standard deviation of noise when (d) ECL and (e) DFB is used as the optical source; (f) comparison between the modeled standard deviation of noise when ECL (dashed lines) and DFB (solid lines) is used as the source.

noise sources into the model.

The modeled wavelength dependent standard deviation of noise at the link end is in good agreement with experimental data for both the ECL and the DFB experiments, as can be seen in Figure 3.15(d) and (e). This in turn confirms the accuracy of our analytical expressions, which are used for the inclusion of RRM's phase-to-intensity noise conversion in the link model.

Let us now take a closer look at the noise standard deviation extracted from experiments with the DFB laser (Figure 3.15(e)). The measured curves show asymmetric features, unlike the standard deviation of the phase-to-intensity converted noise predicted by our model and shown in Figure 3.2(b), which is symmetric relative to the ring resonance. This asymmetry is caused by the correlation of part of the laser phase noise with the laser RIN, as explained in detail in the previous section. The intensity noise resulting from the RRM conversion of its correlated phase noise retains the correlation to the laser RIN. The sign of this correlation changes from negative to positive as the carrier biasing wavelength crosses the resonance. Therefore, the noise magnitude has its maximum value when the optical carrier is biased at wavelengths longer than the resonance. This effect comes from the dispersion induced by the RRM, which also has a different sign depending on whether the wavelength of

interest is shorter or longer than the resonant wavelength. Furthermore, the asymmetry reduces with the increase of the output laser power from 3 dBm (orange data in Figure 3.15(e)) to 6 dBm (red data in Figure 3.15(e)). The reason is the reduction of the overall laser RIN and, consequently, all its effects on the resulting noise (Figure 3.5).

Figure 3.15(f) compares the modeled noise standard deviation of the links that include the ECL (dotted line) and the DFB (solid line). From it, a better noise performance with the lower linewidth optical source is evident, more notably so for the wavelengths longer than the resonance.

Next, we wish to analyze to what extent the different noise sources contribute to the overall noise at the link end. We do this in simulation, assuming a DFB source with 6 dBm output power. This is practically implemented by turning on a single noise source at a time in the simulation and iterating through all the noise sources present in the system. The results of the noise partitioning are shown in Figure 3.16(a).

The photodetector input referred noise (thin dot-dashed orange line) does not depend on the received power, i.e. on the optical carrier biasing, as expected.

The intensity noise caused by the baseline laser phase noise (green dotted line) features the expected detuning dependent standard deviation predicted by our analytical model.

The same wavelength dependency is observed for the standard deviation of the intensity noise induced by the conversion of the RIN-correlated phase noise (dashed light blue line).

Furthermore, the expected wavelength dependence of the propagated RIN is a monotonous increase with the growing filtered carrier power, as the detuning from resonance increases. However, the recorded dependency deviates from this expectation (dashed dark blue line). This deviation is caused in part by RIN-to-phase noise conversion mediated by the RRM dispersion, leading to a reduction of RIN off-resonance. As for the converse phase-to-intensity noise conversion, this effect disappears at resonance. This is illustrated in Figure 3.16(c), which shows that the expected trend is recovered (red line) once the RRM dispersion is compensated for. The second cause of RIN reduction is the partial SOA saturation, that is more prominent at higher carrier-to-resonance detunings as a consequence of the higher SOA input power levels. The SOA gain at different carrier detunings is shown in Figure 3.16(d) (right axis, blue line), along with the chip output power (i.e. SOA input power) for the same detuning points (right axis, purple line).

The trend for the SOA's ASE contribution (dot-dashed yellow line) also has two determining factors: the overall ASE power increase with the increased detuning from the resonance and, similar to the case of RIN, the gain compression at higher

SOA input powers.

When examined individually, none of the noise standard deviation curves features the asymmetry relative to RRM resonance which is present in the wavelength dependency for the overall noise. To capture this effect in simulation, the laser RIN and its correlated phase noise must be turned on simultaneously in the model. From Figure 3.16(b), it can be observed that the asymmetry then appears (thick solid line), confirming that it indeed stems from the correlation of these two noise sources.

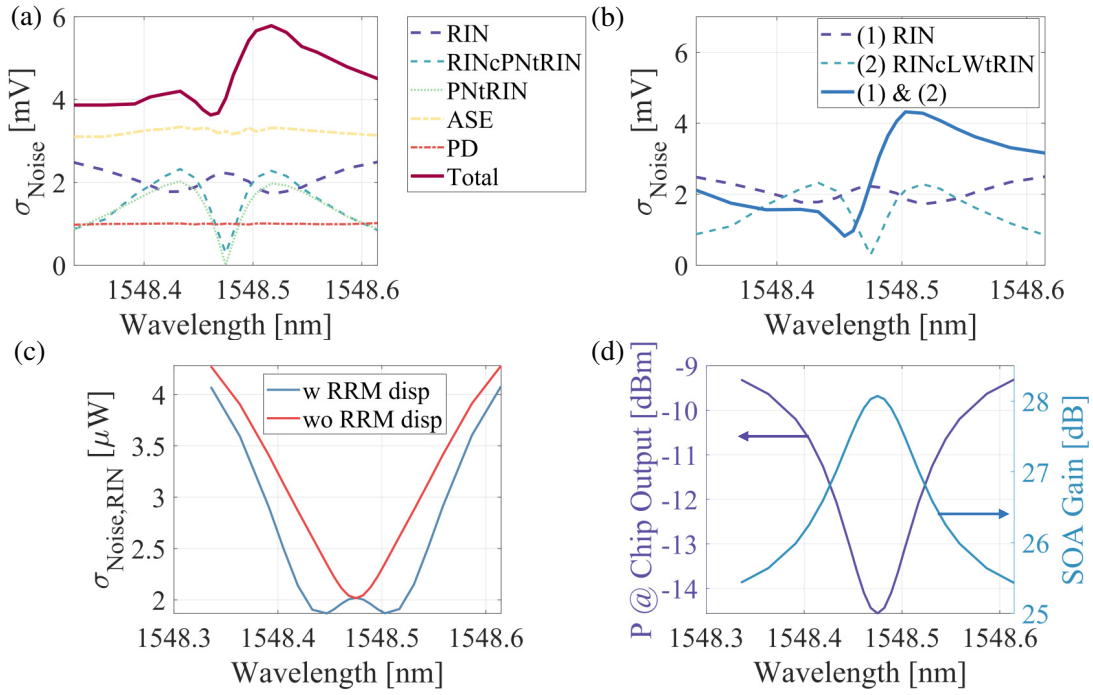

Figure 3.16: (a) Partitioning of the modeled noise into individual noise source contributions at the end of the link, with the DFB as the optical source and the output power setting of 6 dBm; (b) contribution of RIN (purple dashed line), intensity noise stemming from RIN-correlated phase noise (dashed light blue line), and their joint effect with the correlation considered (solid blue line); (c) RIN magnitude at the chip output when the modulator wavelength-dependent phase shift is considered (blue line) and compensated (red line); (d) power at the chip output (i.e. SOA input; left axis, purple line) and corresponding input power dependent SOA gain (right axis, blue line)

Furthermore, we want to examine if the choice of the sideband has an influence on the resulting noise curves. To this end, the experiments were conducted for both the lower frequency sideband (LSB) and upper frequency sideband (USB) loaded with information symbols, for all laser output settings of relevance. The comparison of all relevant metrics is shown in Figure 3.17, for both ECL (panels (a)-(c)) and DFB (panels (d)-(f)) experiments. Here, the results of the LSB and the USB loading are shown in dashed and solid lines, respectively. The maximum modulation effi-

ciency, reflected in the standard deviation of the mean signal, is achieved for LSB loading with the carrier biased at a wavelength shorter than the resonance (Figure 3.17(b)and (e)). On the other hand, the carrier has to be biased at a longer-than-resonant wavelength to reach maximum efficiency for the USB-loaded case. It can therefore be concluded, that the configurations that maximize the modulation efficiency leverage the amplification of the useful sideband through peaking enhancement of the ring. This is more graphically illustrated in Figure 3.18, where SSB signals are overlaid with the resonant transmission profile of the modulator. Nevertheless, the noise standard deviations from the two sets of experiments coincide, indicating that the choice of the modulated sideband has no bearing on the total noise in the system (Figure 3.17(c) and (d)).

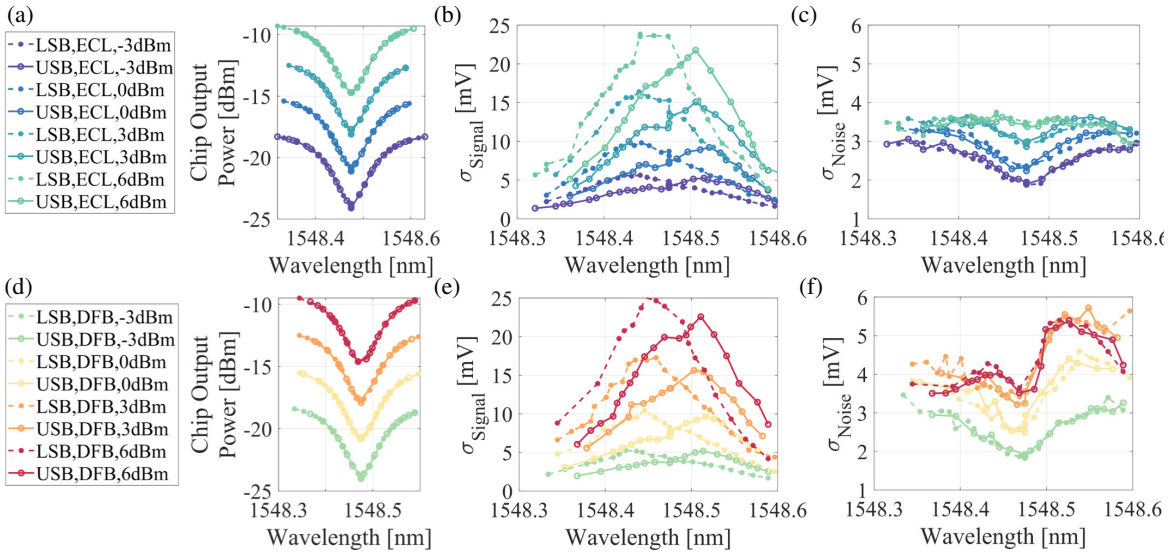

Figure 3.17: Comparison of measured values for LSB (dashed lines) and USB (solid lines) loaded data transmission with the ECL/DFB as the optical source: (a)/(d) power at the chip output; (b)/(e) standard deviation of the average signal at the end of the link; (c)/(f) noise standard deviation at the end of the link.

To qualitatively compare the performance of the two light sources, we examine the experimentally obtained cumulative EVM of all sub-carriers. Here, we focus on the experiments with the laser output power setting of 6 dBm. Moreover, we do this for two cases. First, the data is loaded onto the LSB (Figure 3.19(a)), same as for experimental and modeling results shown in Figures 3.15(a)-(f). In the second case, the data is loaded onto the USB (Figure 3.19(b)). The reported EVM is extracted from all the recorded signal traces after OFDM demodulation and single-tap equalization.

The data shows that the performance of the DFB based link is penalized at carrier wavelengths longer than the resonance, where the noise magnitude is the highest.

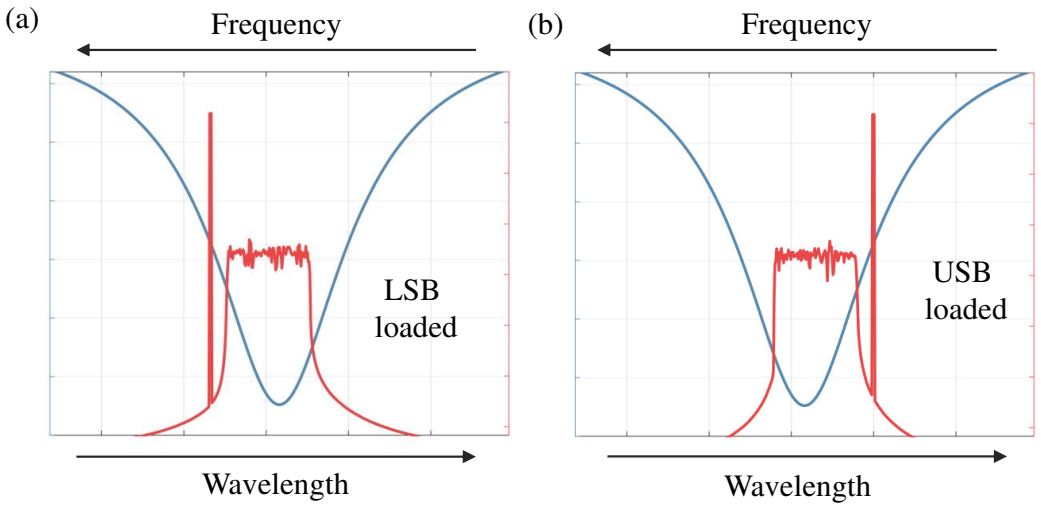

Figure 3.18: Overlay of the detuned signal and RRM resonance for (a) LSB and (b) USB loaded case.

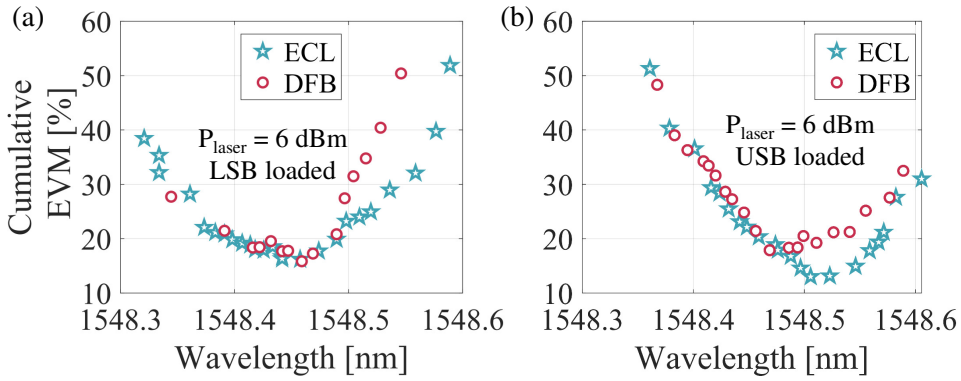

Figure 3.19: Error vector magnitude versus different optical carrier bias points, for transmission with a DFB (circular markers) and an ECL (star markers) when data is loaded onto the (a) lower frequency sideband (LSB) and (b) upper frequency sideband (USB); laser output power is set to 6 dBm in all instances.

As a consequence, when the USB is loaded with data, the difference in EVM between the optimal point for the ECL and the optimal point for the DFB amounts to ~7%. It is also worth noting that slightly better performance is obtained with the ECL when the USB is used for transmission and the optical carrier is biased at wavelengths longer than the resonance. The EVM then reduces from 15.8% to 13% for the best operating point compared to the LSB loaded transmission. Moreover, better performance is generally obtained when the loaded sideband is towards the resonance relative to the carrier, as the RRM peaking effect enhances the used sideband (see Equation 2.25 and Figure 3.18).

For the laser output power of 9 dBm, in adition to BtB experiments, we measured the transmission over 10 and 20 km of SMF. However, it proved to be difficult to consolidate experimental and simulation results when fiber transmission was considered. We believe that the discrepancies arise partially due to the incomplete modeling of the noise inside of the SOA. Namely, the phase to intensity noise conversion present in this gain medium, similarly as for the semiconductor lasers, is not included in our models.

3.4 Summary

In this chapter we studied in detail the phase to intensity noise conversion by resonant structures. We presented a full analytical model that describes statistical and spectral properties of this noise source. A closed form expression, dependent solely on laser linewidth, cavity lifetime, carrier to resonance detuning and coupling strength between the ring and the waveguide describes the wavelength dependent standard deviation of this noise source. Noise PSD takes the shape of to the small-signal EO S_{21} of the modulator at different carrier to resonance detunings.

Moreover, we include our analytical model as a part of the analysis of an RRM assisted SSB-OFDM link. Other noise sources included in the link simulation are laser RIN, SOA ASE and input referred noise of the photodetector. Apart from the correction for RIN-correlated phase noise which is introduced numerically, the noise behavior predicted by the analytical model matches closely the experimental results.

The experiments also clearly show better performance of the low linewidth source when optical carrier is biased at wavelengths longer than the resonance. For these biasing points, the correlation between RIN and a portion of frequency noise increases the total noise. This in turn penalizes the signal quality when a noisier DFB laser is employed.

Chapter 4

Full capacity measurements

Material in this chapter is partially published in [81], Section III C.

In this chapter we use the three channels of the RRM assisted SSB integrated transmitter to optimize its overall throughput for the case of OFDM data transmission. In these experiments, channels are run successively and DFB lasers are used as optical sources (Section 4.1). Afterwards, we look at effects that may cause a reduction in the suppression of the unused sideband (Section 4.2). This phenomenon is of high importance in fiber transmission since it influences dispersion mediated signal distortion.

4.1 Results

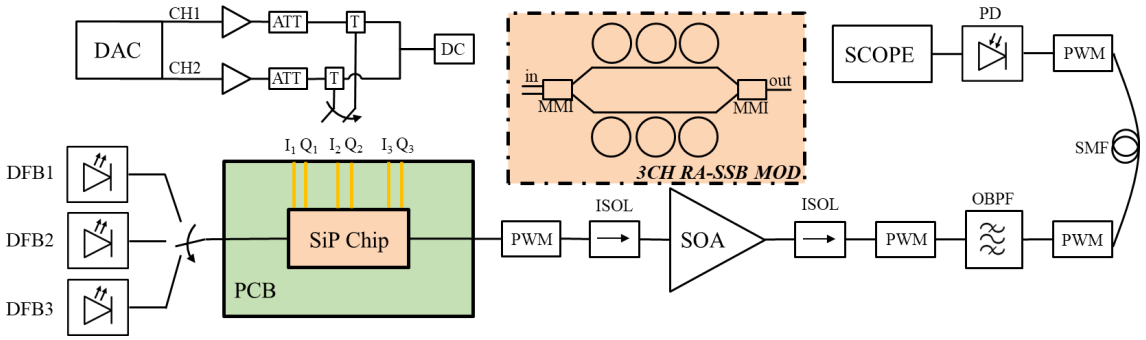

Figure 4.1: Setup for full capacity experiments. Three channels of the RA-SSB system are run sequentially with different DFB lasers.

The basic link configuration in these experiments looks similar to the one in the

previous chapter and is shown in Figure 4.1. In addition to BtB measurements, however, we transmit the data over up to 20 km of standard SMF. To better match the realistic scenario in DD links, we opted to use the DFB lasers as optical sources. The more expensive, lower linewidth sources such as ECLs are more typical for coherent optical transmission.

Each channel is tested using a different DFB module, with the optical carriers biased at 1547.05 nm for channel 1 (CH1), 1547.75 nm for channel 2 (CH2), and 1548.45 nm for channel 3 (CH3). In all experiments, the laser output power is set to 9 dBm. Such a high power at the RRM input causes thermal instability of the device, allowing us to stably bias the carrier only at the wavelengths shorter than the ring resonance. Incidentally, and to our advantage, the noise magnitude is also lower at these wavelengths for the high linewidth sources in use here, as can be seen in Figure 3.15. This means that the optimal biasing point is within our reach from the practical perspective and we use it for the following experiments.

Sub-carrier loading is optimized so that the worst-performing channel at the transmission distance of 20 km has its BER below the 20% hard-decision forward error correction (HD-FEC) limit ($1.5 \cdot 10^{-2}$) [98]. As before, the FFT size of 512 is used. Sub-carriers 2-121 of the lower frequency sideband (numbered from the optical carrier) are loaded with 8QAM symbols. Sub-carriers 122-180 carry QPSK symbols due to their lower signal-to-noise ratio, mostly dictated by the roll-off of the modulator. Consequently, considering the 62.5 MHz sub-carrier spacing, the signal occupies the frequency band from 62.5 MHz to 11.31 GHz. Furthermore, the raw data rate per channel amounts to 30 Gb/s. As before, a block of 128 symbols is sent through the link. Since the number of symbols is too low for a reliable per-sub-carrier statistics, cumulative BER for the entire transmitted sequence is calculated. The total number of transmitted bits, namely 61440, is nevertheless sufficient for accurate BER prediction on the order of 10^{-3}. The BERs at different propagation distances are summarized for all three channels in Figure 4.2(a). The results show that all three channels fulfill the imposed condition.

Moreover, exemplary constellation diagrams for 8QAM and QPSK for CH1 and transmission distance of 20 km are shown in Figure 4.3. CH1 shows the best performance and its spectral efficiency, considering a 3% CP and 7% FEC overhead, is ~2.4 b/s/Hz. The other two channels, CH2 and CH3, exhibit a somewhat worse performance, requiring a larger 20% FEC overhead for error-free transmission. This, together with the same 3% CP, leads to a spectral efficiency of ~2.1 b/s/Hz for these two channels. Performance degradation with the increased reach can mostly be attributed to the additional loss of 5.2 dB introduced by the interposed fiber. To reduce this influence, the attenuation at the SOA output could have been adjusted.

To rule out the influence of dispersion on signal degradation, we compare the

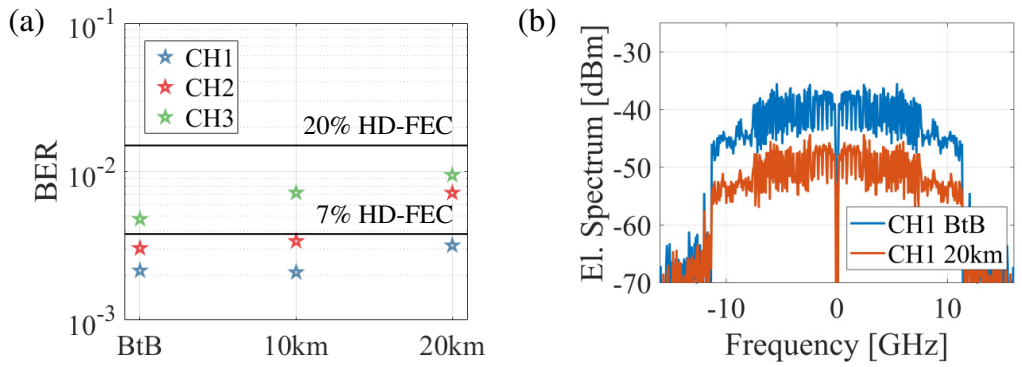

Figure 4.2: (a) Bit error ratio for the three channels of the system for varying propagation distance; (b) received electrical spectra of CH1 for back-to-back and 20 km propagation.

received electrical spectra for the BtB configuration and transmission over 20 km fiber stretch (Figure 4.2(b)). The recorded electrical spectrum after fiber propagation features no obvious distortion, indicating that the dispersion does not have a notable influence on signal degradation in the given link. However, it should be noted that the signal itself is still narrowband due to the limitations of the link components, primarily the RRM used in the system so that the influence of the fiber dispersion should not be large for the distances considered in this work.

To benchmark OFDM against the more commonly utilized OOK, we qualitatively examine what the transmission of 30 Gbit/s OOK signal over 20 km of dispersive fiber would look like if the RRM used for modulation is identical to the one in our system. For this, we turn to simulation, in which only the ring modulation and the propagation through a lossless fiber are considered, to highlight the interplay between the RRM chirp and fiber dispersion. The detuning point that leads to the highest eye opening at the modulator output is chosen. Received eye diagrams are show for BtB, 10 km and 20 km fiber transmission in Figure 4.4(a), (b), and (c), respectively. It is evident that at 20 km the eye is heavily distorted due to ISI caused by the propagation of the chirped signal through the dispersive channel, even in the absence of noise. To recover it, one must either propagate the signal through a stretch of a dispersion compensating fiber (DCF) or employ a time-domain equalization technique. The first solution carries with it high infrastructure costs and lacks flexibility. The second one becomes increasingly difficult as signaling rates increase. Moreover, the OOK signal's spectrum is wider than that of the SSB-OFDM signal. Therefore, a larger guard band between the WDM channels is required, further reducing spectral efficiency. These results, therefore, show the benefits of SSB-OFDM over OOK modulation scheme when RRMs are used in WDM systems for data transmission over dispersive fiber links.

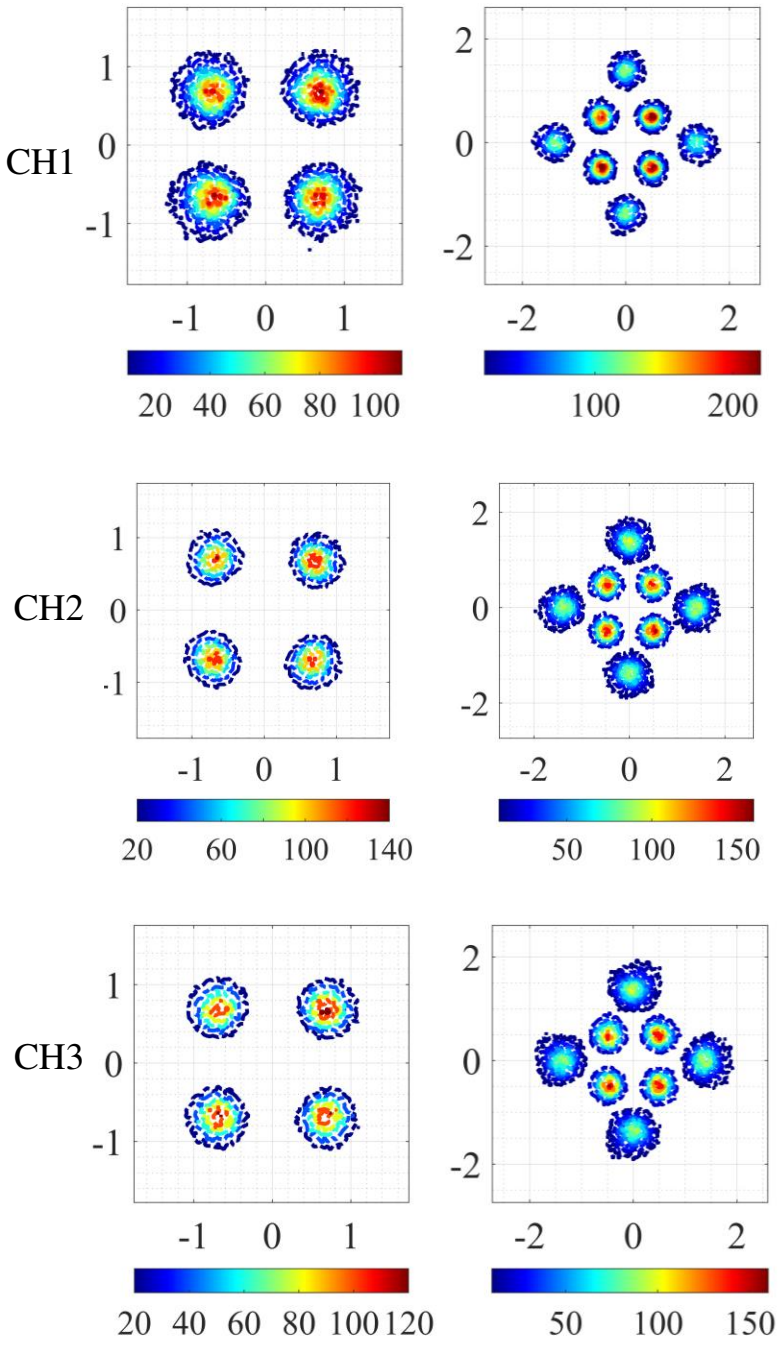

Figure 4.3: Constellation diagrams for sub-carriers loaded with QPSK (left panels) and 8QAM (right panels) for the three channels at propagation distance of 20 km.

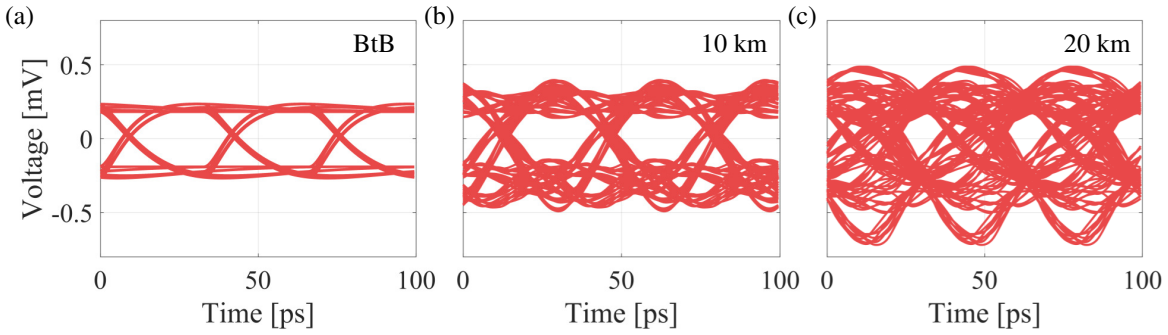

Figure 4.4: Simulated eye diagrams of a 30 Gbit/s signal for (a) back-to-back, (b) 10 km and (c) 20 km transmission. Only modulation by our RRM and the propagation in a dispersive lossless fiber are considered in the link.

4.2 Sideband suppression

Sufficiently high suppression of the unwanted sideband is essential for mitigating frequency fading caused by dispersion in each individual WDM channel. Moreover, in order to maximize the throughput of a multi-channel system achieved by tightly packing the WDM channels, suppression of the unused sideband must be high enough not to incur any penalties to the neighboring channels. In this section, therefore, we analyze the influence of some link components on the unwanted sideband suppression ratio (SSR). In particular, we focus on their associated nonlinearities, as well as their operating conditions.

To do this, we once again turn to simulation. We use the sub-carrier loading from Chapter 3 (i.e. sub-carriers 21-100 are loaded with randomly generated QPSK symbols) and the laser power setting of 9 dBm, when not otherwise specified, and look at the BtB link configuration. Moreover, we mostly deal with the noiseless propagation through the link, unless otherwise noted. The optical carrier to resonance detuning is also fixed and it is marked with a red circle in Figure 4.5, which shows the power levels at the modulator chip output versus wavelength. This detuning also corresponds to the one used in the full capacity data transmission experiments from the previous section.

Modulator

First, we look at the influence of the integrated RRM assisted SSB modulator. The first source of SSR degradation comes from the nonlinear electro-optical transfer function of the RRMs when large amplitude signals are applied to the modulator. This effect is illustrated in Figure 4.6. In this and all the following spectral representations, the signal PSDs are smoothed and normalized so that the used sideband

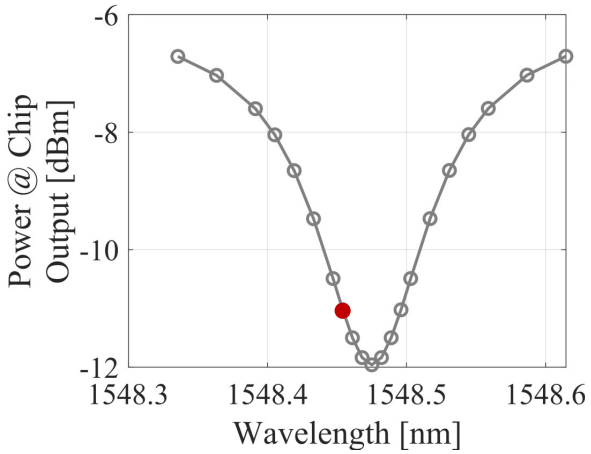

Figure 4.5: Optical power at the chip output when laser power is set to 9 dBm. Red dot marks the carrier biasing point for full capacity measurements and the discussion about the sideband supression ratio.

is at 0 dBc/Hz. This facilitates easier comparison between the signals recorded at different points of the link, which intrinsically have different magnitudes.

When a signal of low amplitude (100 mV peak-to-peak) is used for modulation, the optical signal at the modulator chip output has the same SSR as the applied electrical signal (Figure 4.6(a)). As mentioned previously, the electrical signal itself also does not feature infinite extinction outside of the used sideband due to the insertion of a non-zero CP. However, when the modulating signal amplitude is increased to 2 V peak-to-peak, identical to the signal strength in all our experiments, the SSR is reduced by 10 dB at 2 GHz (from 33.6 to 23.6 dB), relative to the SSR of the electrical signal (Figure 4.6(b)). Nevertheless, the remaining SSR is practically high enough to enable distortion-free DD reception of the SSB signal.

Next, we look at how the SSR is affected when the phase difference between the I and the Q branches of the SSB modulator deviates from $\pi/2$, i.e. from quadrature. Quadrature condition is in general a key prerequisite for complete suppression of the unused sideband. Figure 4.7(a) shows the signal PSD for varying phase offsets from quadrature. As the offset increases, the unwanted sideband becomes more prominent. The SSR reduction trend with the increasing phase offset is depicted in Figure 4.7(b), showing a decrease in SSR of roughly 3 dB per 5 degrees of offset. Moreover, if we want the RA-MZI to operate as an IQ modulator for all WDM channels, the quadrature condition needs to hold across the full wavelength span of interest. The conventional 2-by-2 MMI at the MZI input introduces a wavelength dependent phase shift variation of less than $\pm 1\%$ of the targeted 90° across the whole C-band. This can be even further improved by employing subwavelength structures [99]. Moreover,

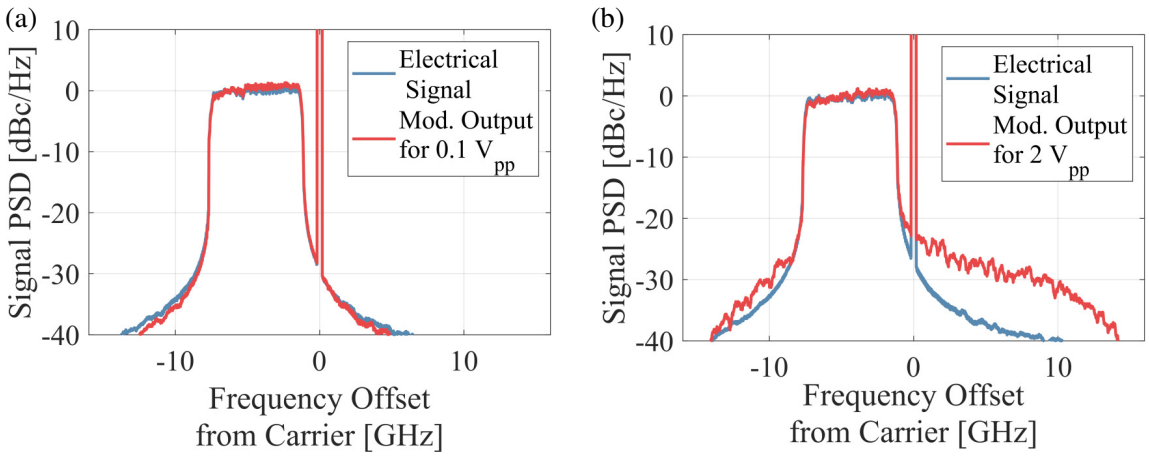

Figure 4.6: Spectra of the electrical IQ signal (in blue) and optical signal at the modulator output (in red) for modulating signal strength of (a) 0.1 V peak-to-peak and (b) 2 V peak-to-peak.

any phase offset caused by fabrication induced variations can be compensated for at the central wavelength using the on-chip thermal tuners. Nevertheless, the phase shift induced by the tuner varies by ±1% over the C-band. Moreover, fabrication induced phase shift varies by ±2% of its value at the central wavelength, leading to a total of ±3% across the C-band. With the 70° phase error that needed to be corrected at system startup together with the MMI error, we end up with the variation of ±3°. This can in turn lead to an SSR reduction of less than 2 dB, which is still modest and does not degrade the performance of the system across all channels.

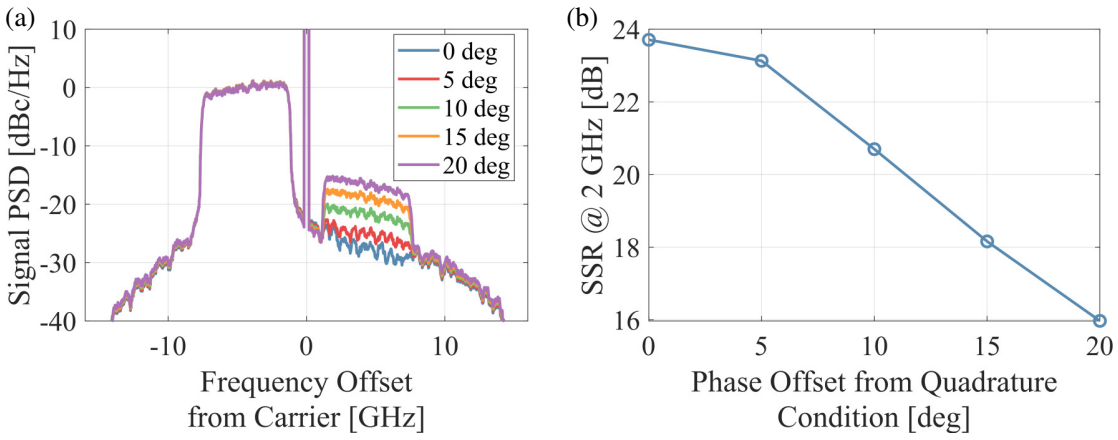

Figure 4.7: (a) Power spectrum of the noiseless optical signal at the chip output and (b) sideband supression ratio at 2 GHz for different offsets from the quadrature condition.

Another important source of SSR reduction is the misalignment between the resonances of the RRMs in the I and Q arms of the MZI (further denoted as I-RRM and Q-RRM). To quantify its influence, the resonance of the I-RRM is kept fixed in the simulation, with its transmission shown in solid black line in Figure 4.8(a). On the other hand, the resonance of the Q-RRM is shifted, with its transmission shown in colored dashed lines in Figure 4.8(a) for different levels of resonance misalignment. Figure 4.8(b) shows the optical signal PSD at the modulator output for all these configurations. It can be seen that even a small misalignment equaling a fraction of the resonance full width half maximum (FWHM) results in a notable reduction of the SSR. More specifically, for a misalignment of 6.8% FWHM (9.5 pm) the reduction equals 5.8 dB, while the misalignment of 13.6% FWHM (19 pm) reduces the SSR by 11.4 dB. This amount of penalty in combination with, for example, the one incurred by the modulator nonlinearity can lead to a high degradation of the signal upon fiber propagation and DD. Therefore, a special care needs to be taken to avoid this scenario. In practice, ensuring the resonances are well aligned can be achieved by monitoring the ER of the resonance profile at the SSB modulator output. Namely, if the alignment is good, the resulting extinction should be equal to that of the isolated I-RRM and Q-RRM resonances. Furthermore, this extinction should remain unchanged with the variation in the biasing point between the two MZI arms. On the other hand, even at quadrature the ER of the SSB modulator resonance profile differs from that of the isolated RRM resonances when the misalignment is present. More specifically, the final ER is smaller when the relative offset between I-RRM resonance and Q-RRM resonance is negative and higher when it is positive (Figure 4.8(c)). Moreover, the SSB modulator resonance profile changes considerably with a changing phase offset between the arms of the MZI when the I-RRM and Q-RRM resonances are misaligned (Figure 4.8(d)) .

SOA

Furthermore, a large contribution to the reduction of the SSR in the link originates from the nonlinear behavior of the amplifier when the high power is present at its input. FWM process creates an image of the used sideband on the other side of the optical carrier. Figure 4.9(a) and (b) show the signal PSD at the receiver and the values of SSR at 2 GHz, respectively, for different laser output power levels (i.e. different power levels at the SOA input). For a laser power setting of 9 dBm, equivalent to our full capacity experimental setup, the SOA's FWM penalty to the SSR at 2 GHz totals 10.8 dB, leading to a final SSR of 12.8 dB at this frequency. It should be noted that in our SOA model waveguide dispersion is not considered and phase matching is assumed, which may overestimate the FWM contribution even at the wavelength

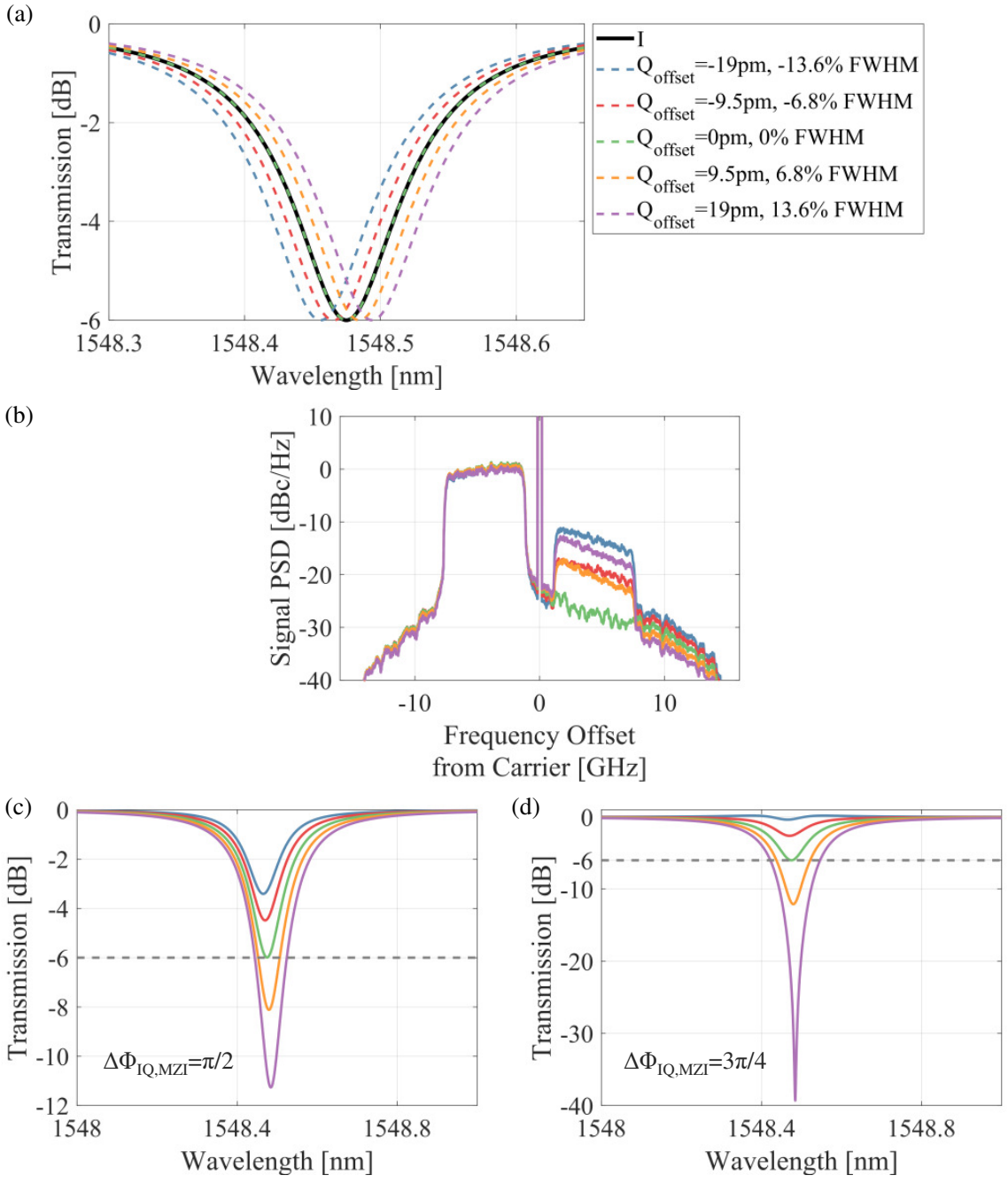

Figure 4.8: (a) Transmission of the individual RRMs in the I (solid black line) and the Q (dotted colored lines) branch. Differently colored dotted lines show scenarios with varying misalignment between the resonance in of the I-branch RRM (kept fixed) and the one in the Q-branch (varied) of the SSB modulator. (b) Optical signal PSD at the SSB modulator output. Normalized transmission of the SSB modulator (c) at quadrature and (d) away from quadrature condition between the two MZI branches for varying I-branch and Q-branch RRM resonance misalignement (color coding as in panel (a)).

separation as small as the one between the optical carrier and the signal.

To largely reduce the undesirable effect of FWM, the SOA can be replaced by an erbium doped fiber amplifier (EDFA). Alternatively, one could use a lower laser output power setting in the 0 to 3 dBm range, where the effect of the nonlinearity is still not as pronounced (Figure 4.9(b)). However, this would negatively affect the signal SNR, so a trade-off between the two effects on the overall signal quality should be studied in more detail.

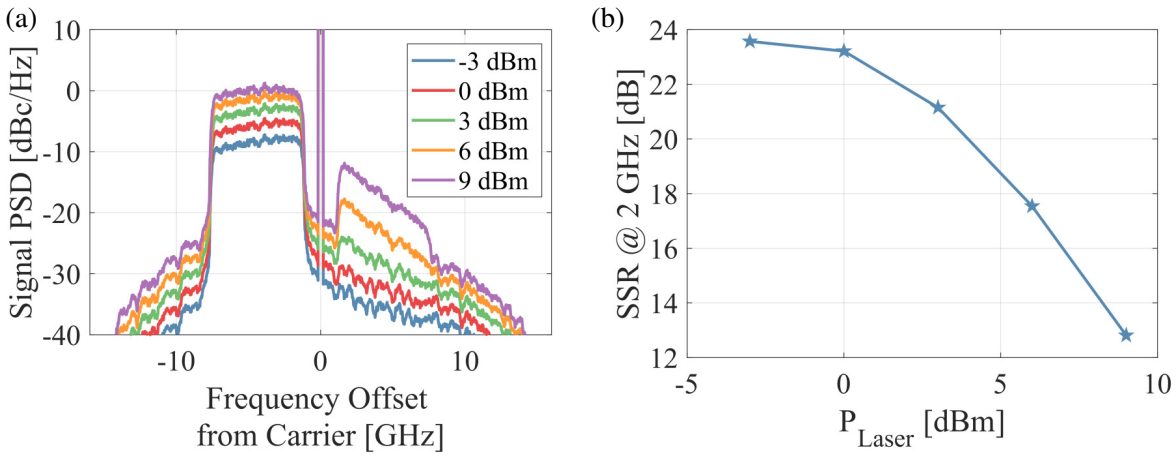

Figure 4.9: (a) Power spectrum of the noiseless optical signal at the receiver and (b) sideband supression ratio at 2 GHz for varying laser ouptut power (i.e. varying power levels at the SOA input).

Laser noise

Finally, we take a look at the signal at the receiver with all the noise sources considered. The blue curve in Figure 4.10 shows the signal PSD at the link end, while the red one is recorded when no modulation is present, marking the noise floor in the system. Far from the carrier, the noise floor is dictated by the ASE and receiver noise, whereas at the carrier proximity, the bulk of the noise comes from the laser RIN and the laser phase noise induced RIN. To handle the influence on the neighboring channels, one could insert a guard of ~5 GHz, so that the noise is reduced to the background level. However, this would also reduce the overall system spectral efficiency.

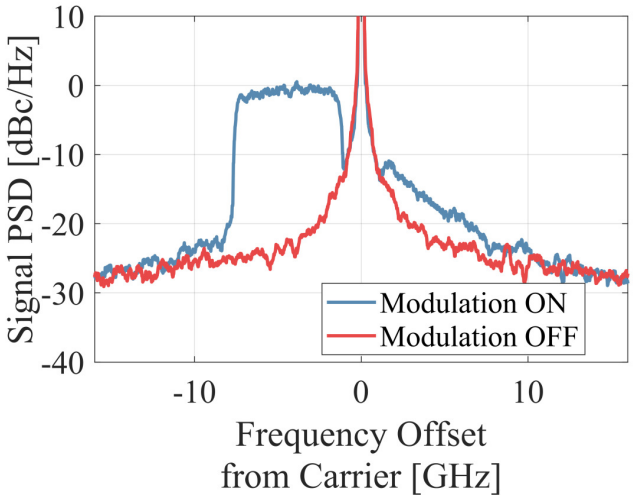

Figure 4.10: Optical signal PSD at the receiver end of the link with all the noise sources in the system turned on and modulation turned on (blue line) and off (red line).

4.3 Summary

In this chapter we have shown the results of the full capacity measurements of the three-channel RA-SSB modulator in the case of the OFDM transmission. All three channels achieve a 30 Gb/s raw data rate for transmission over up to 20 km of SMF, with the BER below the 20% HD-FEC limit. Achieved spectral efficiency for CH1 (at 1547.05 nm) is ~2.4 b/s/Hz, while for the lower performing CH2 (at 1547.75 nm) and CH3 (at 1548.45 nm) is ~2.1 b/s/Hz.

Moreover, we analyzed the influence of link components on SSR. As other sources of SSR reduction can be addressed by a careful adjustment of the operating point by means of the on-chip thermal tuners, nonlinearity remains its main cause in our link. Regarding the modulator, nonlinearity causes a reduction of up to 10 dB, leading to an SSR of 23 dB. Nonetheless, this value is in practice sufficient for distortion-free transmission of high speed signals through 20 km of dispersive fiber. Another major contributor is the nonlinearity of the SOA. With an additional penalty of ~11 dB introduced by the SOA, the resulting value of the SSR after modulation and amplification is 12 dB. Although in our specific link scenario this did not pose a major limitation on our signal, it might become a problem for longer reach and/or higher speed signals. This is why the employment of an EDFA might prove necessary in high-speed, long distance SSB links.

Chapter 5

Polarization diverse WDM receiver with a reduced number of OADMs

Most of the content of this chapter is published in [100]. Static device characterization and system measurements were performed by Dominik Schoofs, in the scope of his Master thesis project work at the Institute of Integrated Photonics [101].

5.1 Introduction

Data transmission through inexpensive standard single mode fibers is inevitably followed by polarization scrambling, resulting in the random polarization state at the receiver (RX) end of the link. Receivers therefore need to show a high degree of polarization insensitivity to prevent loss of data. To handle this, some methods involve coherent recombination of polarizations, where thermal tuners are used to correct for the phase offset between the orthogonal states [102]. The tuners used to this purpose are in general capable of introducing a 2π phase shift, sufficient to correct for any phase difference at initial setup, introduced between the two polarizations through propagation and/or chip coupling elements. Nonetheless, with the fluctuating environmental conditions and system component instabilities during operation, a situation may emerge in which the tuners meet the limit of their dynamic range. This in turn can lead to a temporary loss of service. To mitigate this, incoherent summation of electrical signals is preferred. This can, however, lead to the undesired doubling of electronics if the photocurrents are not added before amplification.

Here we investigate an integrated, polarization-transparent RX system implemented in SiP platform and aimed for WDM applications. A single RX channel consists of a double-sided optical add-drop multiplexer (OADM) and a double-sided integrated germanium (Ge) photodiode. These enable simultaneous filtering and detection of both polarizations. Moreover, we focus here on transmission of intensity

modulated, directly detected (IM-DD) signals with the data initially modulated onto a single polarization state.

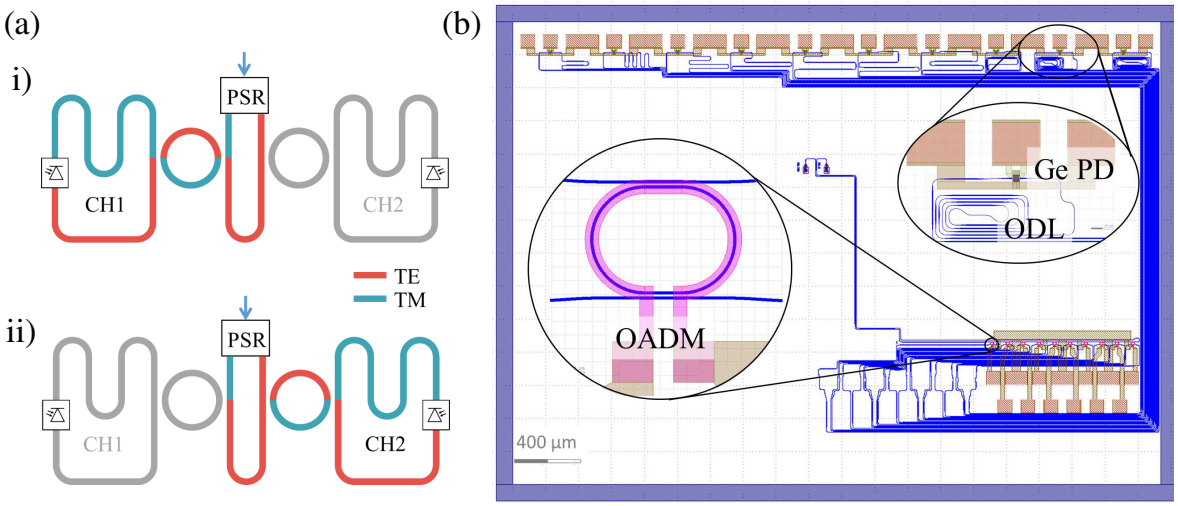

Figure 5.1: (a) Schematic of a balanced polarization diverse receiver, i) and ii) showing the balancing scheme for two channels (CH1 and CH2). Paths for TE and TM polarizations shown in red and blue, respectively; (b) Layout of a 10-channel balanced polarization diverse WDM system. Insets show a layout an OADM and a Ge photodiode with a channel specific on-chip ODL.

In a single channel RX, polarization diversity can be handled elegantly by routing the two polarizations to the opposite ends of a waveguide photodiode, where they sum up incoherently after the opto-electrical conversion. In some previous applications of this idea to multi-channel systems [103–105], each channel required two filtering elements - one for each polarization - before sending both signals to a double-sided Ge photodiode for detection. In addition to that, we here extend the same concept to OADMs, using them in a dual-sided configuration and thus reducing the number of filtering elements per channel. This in turn not only reduces the total footprint of the RX system, but also calls for a lower number of control signals, lowering thereby the overall RX complexity and power consumption. The to-be-detected signal is first split in two based on polarization, either by using an on-chip integrated polarization splitting element, such as a polarization splitter rotator (PSR) or polarization selective grating coupler (PSGC), or an external element prior to coupling to the RX chip. The resulting two signals are then routed to a single waveguide from its opposite ends (i.e. in the opposite propagation directions). An array of OADMs is coupled along the waveguide to independently drop each WDM channel. OADM picks up both signals that belong to the same WDM channel, sending them to a drop waveguide, once more in the opposite directions. The two filtered signals are fur-

ther routed to the opposite ends of the double-sided Ge photodiode where they get convered into photocurrents and add up. In the first implementation of this scheme [106] the transmission speed was limited to 10 Gb/s by the on-chip imbalance of the paths traversed by the two signals. This introduces a different group delay to the two signals that essentially carry the same information, causing distortion when the corresponding photocurrents are summed up at the photodiode.

To address this, we introduce an optical delay line (ODL) in a form of a waveguide loop between the OADM and the photodiode for balancing. This is illustrated in Figure 5.1(a) for the case of two WDM channels. For channel 1 (CH1, subpannel i)) signal originating from the transverse magnetic (TM) polarization traverses a shorter path (blue path in the schematic) than the one from transverse electric (TE) polarization (red path in the schematic) prior to filtering by the OADM. Therefore, a compensating ODL is introduced in the TM path after the OADM. The converse is true for channel 2 (CH2, subpannel ii)), so the compensation is performed for the TE polarization. ODLs mostly consist of multi-mode waveguides to minimize the influence of fabrication variations. The RX chip was fabricated at the A* STAR Institute of Microelectronics (IME), Singapore, in a standard multi-project wafer (MPW) run.

In this chapter we first look into the isolated performance of the components that comprise our RX system (Section 5.2). These include Ge photodiodes, OADMs and thermal tuners used to align the OADM resonance to the optical carrier. Then, we investigate the ten-channel WDM RX system performance, with the main goal of testing the efficacy of the employed on-chip balancing scheme under high-speed operation (Section 5.3).

5.2 Component characterization

5.2.1 Ge waveguide photodiode

The cross-section and the layout of the Ge waveguide photodiode are shown in Figure 5.2(a) and (b), respectively. The most relevant performance metrics of a photodiode are the dark current, which is the reverse bias current when no light is incident to the device, responsivity and EO bandwidth.

To measure the first two, laser light at varying power levels is routed to the device and diode's current-voltage characteristic (i.e. I-V curve) is recorded. Example curves for CH1 of our system are given in Figure 5.3(a). The dependence of the reverse bias current on the incident optical power shows linear behavior, with the responsivity (in A/W) given by the slope of the curve and the dark current given by its intersection with the y-axis. The same experiment is repeated for all ten channels. The recorded responsivities (right axis, in red) and dark currents (left axis, in blue) are shown for

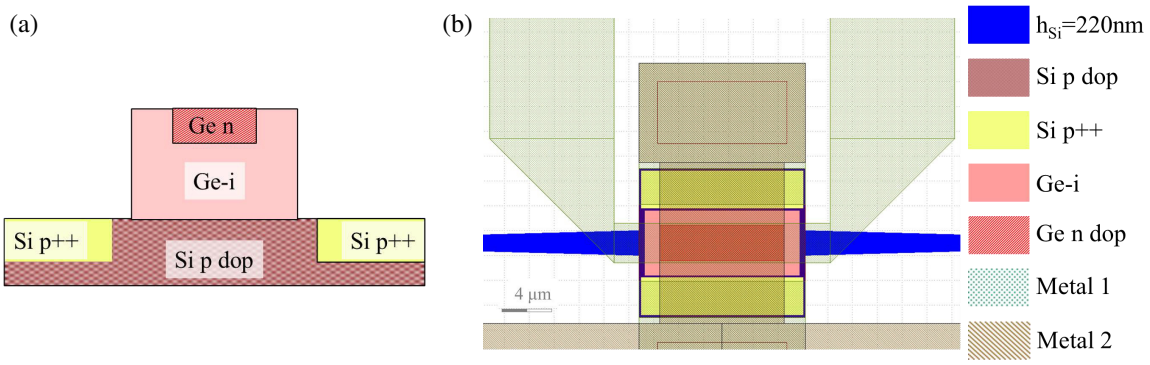

Figure 5.2: (a) Cross-section and (b) layout of the double-sided Ge waveguide photodiode.

all channels in Figure 5.3(b).

Next, high-speed performance of the Ge photodiode is evaluated using the setup shown in Figure 5.3(c). To determine the bandwidth of the isolated device, a test structure consisting only of a GC for optical input and a photodiode, identical to ones used in the system, is measured. The optical signal is supplied by a tunable external cavity laser. A sinusoidal signal up to 50 GHz is applied from a PNA to a commercial Mach-Zehnder modulator. The modulated optical signal is further coupled through the GC to the photodiode under test. The electrical current from photodiode terminals is picked up by a ground-signal-ground (GSG) high-speed probe and sent to another port of the PNA. The measurement is repeated for different reverse bias voltages. Calibrated EO S_{21} curves are shown in Figure 5.3(d). The curves feature a double roll-off, with the 3 dB bandwidth (relative to 3 GHz reference point) above 20 GHz achieved for a diode bias voltage of -2 V.

5.2.2 Optical add-drop multiplexers

The layout of the OADMs used in this work, along with the relevant geometrical parameters, is shown in Figure 5.4(a). The inset shows the cross-section of the directional coupler between the ring and bus waveguide. OADMs have a racetrack configuration. They consist of 430 nm wide and 220 nm thick fully etched waveguides, both in the ring and the bus section. The directional couplers are in a form of a racetrack, with a 5.5 µm long straight waveguide section and a gap between the ring and the bus waveguides of 310 nm. The bent sections of the OADM have a radius of ~ 7.8 µm, resulting in an average FSR of 9.3 nm, sufficient to support parallel reception of ten channels with a 100 GHz spacing. This OADM design was aimed to make the device more tolerant to fabrication induced geometry variation, such as waveguide width variation. This is well reflected in the measured coupling coefficient of 0.28 being very close to the design value (0.26). The measured value is

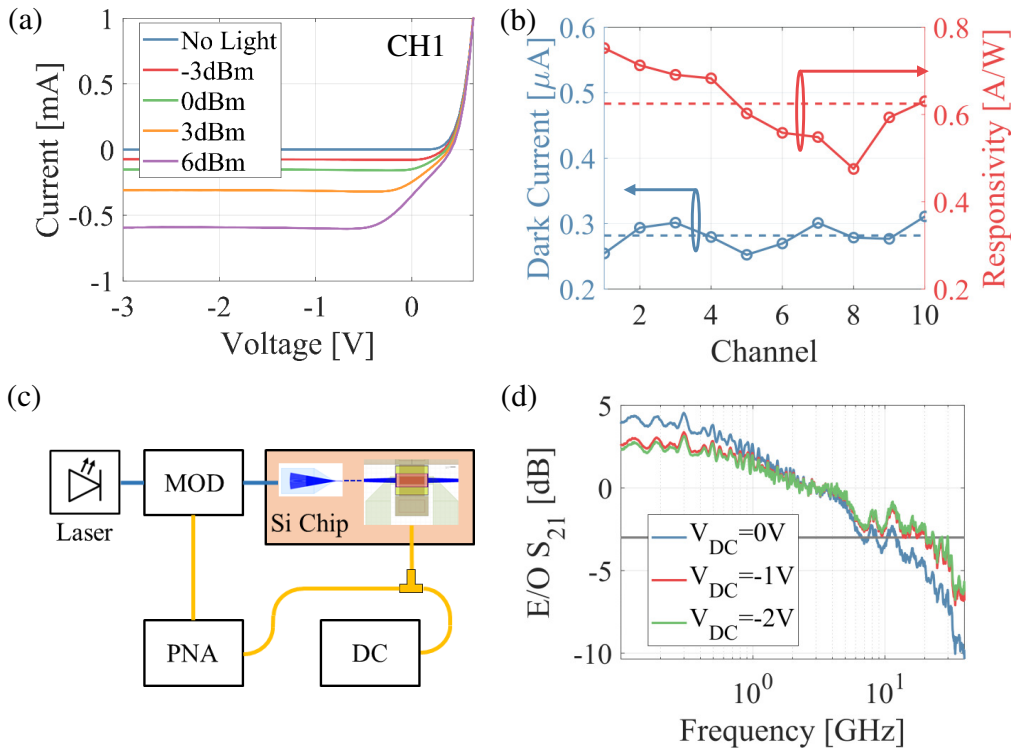

Figure 5.3: (a) I-V curves for CH1 at different laser powers; (b) Dark current (in blue) and responsivity (in red) values for all 10 channels of the Rx system; average values are marked with dotted lines; (c) S_{21} measurement setup; (d) Calibrated EO response for Ge diode test structure (identical to ones in the system) for different reverse bias voltages.

an average extracted by resonance fitting of multiple test structures, using a method described in Chapter 1 for RRMs. Moreover, OADMs show an IL ~1 dB when the optical carrier is biased at resonance.

The OADM bandwidth can also be estimated from the resonance fittings, and it is on average ~ 17 GHz. We proceeded to confirm this with high-speed device characterization, using a setup shown in Figure 5.4(b). Similarly as before, the optical carrier, supplied by a tunable laser source, is modulated by the PNA signal with a commercial modulator and filtered by the OADM test structure. The filtered signal is further received by a commercial photodetector, and finally routed back to the PNA. To provide the calibration curve, the same measurement is repeated without the OADM interposed in the signal path. The resulting calibrated OADM's EO S_{21} responses are shown in Figure 5.4(c). They reveal the average OADM bandwidth of ~ 17 GHz when optical carrier is biased at resonance, as expected from the passive measurements. To increase the device bandwidth, OADMs can be biased away from the resonance to leverage the peaking response of the resonant structure. This, however, brings with itself additional losses, thus reducing the SNR at the link end. Red,

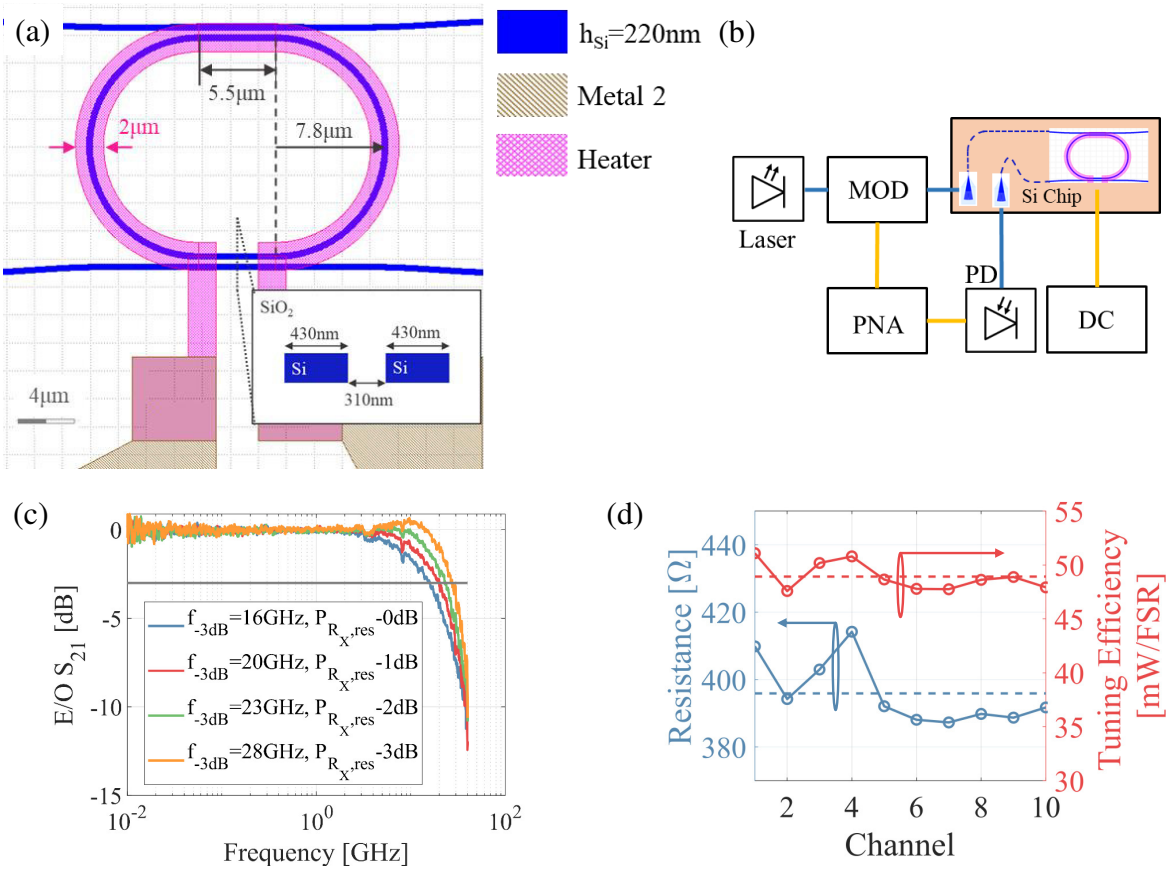

Figure 5.4: (a) OADM layout with marked geometrical parameters; inset shows the directional coupler cross-section; (b) setup for high speed characterization; (c) calibrated OADM electro-optical response at multiple carrier to resonance bias points; (d) heater resistance (in blue) and tuning efficiency (in red) for all 10 channels of the Rx system

green, and yellow curves in Figure 5.4(c) correspond to the optical carrier biasing at which power at the receiver is reduced by 1, 2, and 3 dB, respectively, compared to the at-resonance biasing.

OADMs also include thermal tuners, used for adjusting the spectral position of their resonant wavelengths. They are 2 µm wide TiN metal patches located above the waveguides that cover 80% of the OADM circumference, forming a resistor. By sweeping the voltage applied to the tuner terminals, the resonant wavelength of the OADM shifts, letting us determine the tuning efficiency. The index change is directly proportional to the thermal power being dissipated inside of the waveguide core. The same experiment is repeated for all the channels of the WDM system. Measurement results of heater resistances (left axis, in blue) and tuning efficiencies (right axis, in red) are shown in Figure 5.4(d), with the average values for the system shown in dashed curves.

5.3 System measurements

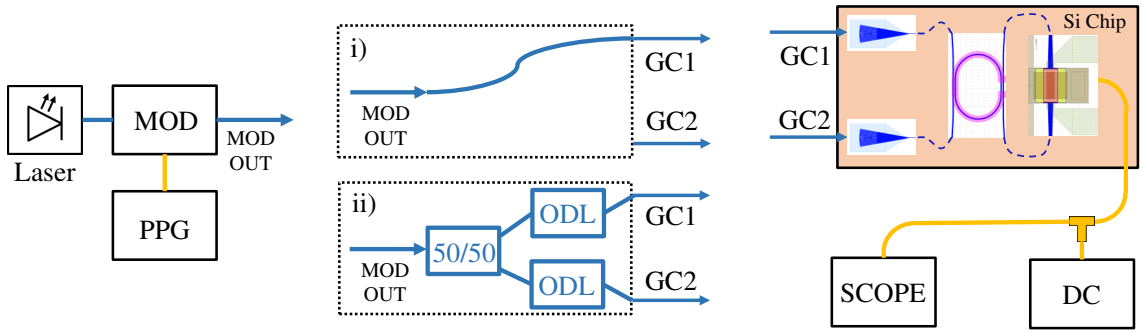

Figure 5.5: Setup for data transmission experiments. i) signifies the configuration for reference measurements, configuration ii) allows for (im)balancing of the external optical paths of the two polarizations, for all WDM channels simultaneously.

Next, we performed system data transmission measurements. The measurement setup is shown in Figure 5.5. In all experiments, the carrier of 12.8 dBm optical power is supplied by a tunable external cavity laser (Agilent 81960A). Light is further modulated by a 30 GHz commercial Mach-Zehnder modulator driven by a 2 V peak-to-peak signal, with 8 dB IL (at the maximum transmission point), and 7.7 dB extinction ratio. A non-return-to-zero (NRZ) pseudo-random bit sequence is generated by the Anritsu MU183020A pulse pattern generator (PPG). The OADMs are tuned to resonance to extract maximum optical power for each channel. Finally, signal detected by the Ge photodiodes (biased at -2 V) is captured by the Agilent DSA-X-92004A real-time oscilloscope with a 20 GHz analog bandwidth. We performed three sets of experiments described in the following.

The first set of measurements serves as a reference. The modulated signal is inserted to the chip through a single GC (configuration i) in Figure 5.5), emulating thus the ideal case in which the entire useful signal is in a single polarization state. The eye diagrams for channel 4 (CH4) are shown in Figure 5.6, for modulation speeds of (a) 10, (b) 20 and (c) 28 Gb/s. All other channels show similar performance.

The next set of experiments was performed to illustrate the detrimental effect of imbalancing on the signal quality at high signaling speeds. Now, the signal after the modulator is split using a 50/50 splitter (configuration ii) in Figure 5.5). This emulates the worst-case scenario in which equal signal power is present in the two polarization states. Moreover, external tunable ODLs are inserted in both signal paths, allowing us to control the off-chip (im)balancing common to all WDM channels. The signals are further routed each to one of the GCs at the RX input. Figure 5.6(d)-(f) shows the averaged eye diagrams (in blue) when a 35-40 ps imbalancing between the two polarization paths is introduced for transmission speeds of 10, 20,

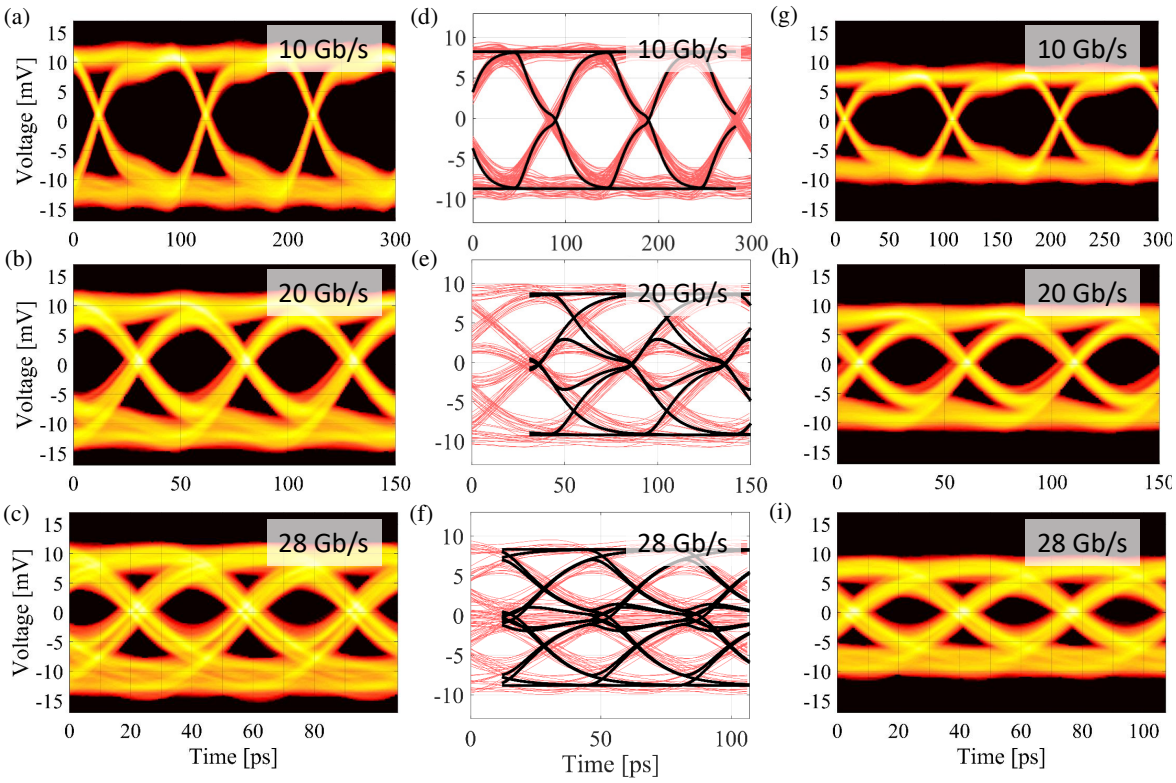

Figure 5.6: Real-time reference (single-polarization) eye diagrams of C4 at (a) 10 Gb/s, (b) 20 Gb/s and (c) 28 Gb/s. Averaged polarization-diverse eye diagrams of C4 (in red) with 40 ps group delay imbalancing at (d) 10 Gb/s, (e) 20 Gb/s and (f) 28 Gb/s overlaid by modeled traces (in black). Real-time polarization-diverse eye diagrams of C4 with balancing at (g) 10 Gb/s, (h) 20 Gb/s and (i) 28 Gb/s.

and 28 Gb/s, respectively. As confirmed by our modeling (black traces overlaid with experimental data in Figure 5.6(d)-(f)), the signal quality, reflected in the eye opening, degrades rapidly with the increasing data rate, completely scrambling the signal already at 20 Gb/s. Although it is generated off-chip in our case, the same level of imbalancing is reported in [106] for a 4-channel system. An imbalacing of 44 ps is present for the worst performing channel, leading to a notable BER penalty already at 10 Gb/s , for the case of equal power split among the two polarizations. Assuming the same geometry as in [106], the most affected channel in of our ten-channel RX would experience a 116 ps delay imbalance, making the data transmission challenging even at very low speeds. Having in mind the constraints posed on the chip layouting by the testing environment and/or packaging requirements, the situation would quickly become unmanageable if no on-chip rebalancing were implemented after each OADM on a channel-by-channel basis.

In the final, third set of experiments the off-chip imbalancing was removed. Eye

diagrams for CH4 are shown in Figure 5.6 for transmission speed of (g) 10, (h) 20, and (i) 28 Gb/s. All other channels perform similarly, thus evidencing the efficacy of the on-chip balancing scheme.

To describe the signal quality, we use a commonly used metric for on-off keyed (OOK) data transmission, the signal quality factor (signal-Q, Q_{sig}). Signal-Q is defined as

$$Q_{sig} = \frac{u_1 + u_0}{\sigma_1 + \sigma_0}, \tag{5.1}$$

where $u_{1/0}$ and $\sigma_{1/0}$ are voltage levels and standard deviation of noise, respectively, associated with the logical 1/0 level.

For a clearer comparison, in Figure 5.7 we show signal-Qs for all channels in the case of the reference, single-polarization (dotted lines) and balanced, polarization-diverse (solid lines) measurements for data rates of 10 (green), 20 (red), and 28 Gb/s (blue). Data shows that the signal quality of the reference measurements was largely recovered in the balanced experiments. A small reduction in signal-Qs for 28 Gb/s can be attributed to the attenuation of the additional elements present in the link in the balanced experimental configuration (~0.3 dB insertion loss of ODLs). It should be noted that the maximum achieved transmission speed was not imposed by the group delay imbalance between the two polarizations, but rather by the bandwidth limitation of the constituting link components.

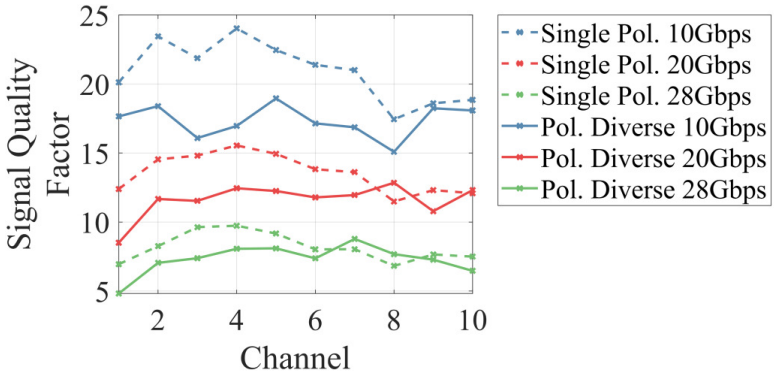

Figure 5.7: Signal quality factors of all channels for single-polarization (dashed lines) and polarization-diverse (solid lines) measurements at 10, 20, and 28 Gb/s.

5.4 Summary

In this chapter we have introduced a ten-channel polarization-diverse integrated WDM RX system. Individual channels of the system consist of double-sided OADMs and Ge photodiodes, that allow for simultaneous filtering and detection of both polarizations. In addition, we introduce ODLs after the OADM for balancing the signal paths and canceling the detrimental group delay between the two polarizations. Speed up to 28 Gb/s is achieved for all channels of the system, limited primarily by the bandwidth of the devices. No degradation due to polarization-diverse configuration is observed, as apparent from the comparison with the reference, single-polarization measurements.

Chapter 6

Conclusions and Outlook

In this thesis we studied integrated SiP resonantly assisted WDM transceiver systems aimed for SSB signal generation and DD.

First, we looked at the performance of an integrated SiP RRM assisted SSB transmitter system, applied for transmission of OFDM signals.

On a more general note, we analyzed in detail the conversion of phase into intensity noise by the resonant modulator. We presented for the first time, to the best of our knowledge, a full analytical description of this noise source. A closed form expression was derived that enables calculation of the wavelength dependent noise standard deviation, when the laser frequency noise follows a Wiener process. This expression is a function of four parameters: laser linewidth, cavity photon lifetime, optical carrier to resonance detuning and coupling strength between the ring and the waveguide. Moreover, noise PSD follows the shape of the detuning dependent small-signal S_{21} of the modulator. This equivalence of the two dynamic processes further enables estimation of the phase-to-intensity converted noise PSD when laser frequency noise deviates from the Wiener process. The resulting PSD is shaped both by the initial frequency noise PSD and RRM's EO S_{21}.

To test the validity of our model, we conducted experiments in which an SiP RA-SSB modulator was used for generation of OFDM signals in the optical domain. The link was also modeled numerically, apart from the phase to intensity noise conversion by the RRM that was introduced through the analytical expressions at the link end. The modeling and the experiments were performed for both the ECL and the DFB as the optical source, in an otherwise identical link setup. The good agreement between the modeled and experimental data confirms the accuracy of our analytical prediction. Nevertheless, when the noisier DFB was employed, a numerical correction was necessary to take into account a portion of phase noise correlated to laser RIN. This correlation leads to a different noise magnitudes for positive and negative carrier-to-resonance detunings, with the noise standard deviation peaking at wave-

lengths longer than the resonance. At these detunings, quality of signals obtained from the ECL experiments is evidently superior to the DFB-assisted ones. Moreover, these experiments indicate that the configuration that yields the best signal quality when a DFB is utilized includes LSB loaded transmission with the optical carrier biased at wavelengths shorter than the RRM resonance.

Next, we pushed the performance of the three-channel RA-SSB system for the case of OFDM data transmission. All three channels achieve a raw data rate of 30 Gb/s over up to 20 km of SMF, with their BER less than the 20% HD-FEC limit. The best-performing channel, CH1, achieves a spectral efficiency of 2.4 b/s/Hz, given that it only requires a 7% FEC overhead for error-free transmission. The other two worse-performing channels, CH2 and CH3, require a 20% FEC overhead, resulting in the spectral efficiency of 2.1 b/s/Hz. According to our simulations, signal of that speed could not be transmitted over such a long fiber stretch if RRMs were used as simple amplitude modulators due to device's chirp. The intrinsic drawback of the resonant modulator is therefore well handled with the SSB configuration.

We also studied the influence of different link components on the SSR. The set-point of the modulator, which includes the phase offset between the MZI arms and the alignment of I-RRM and Q-RRM resonances, can significantly influence the resulting SSR at the modulator output. Nevertheless, these detrimental effects can be alleviated by careful adjustment of the operating point using on-chip thermal tuners. What remains as the main cause of SSR reduction is the nonlinearity of link components. The nonlinearity of our RRMs reduces the SSR by up to 10 dB at 2 GHz, leading to an SSR still high enough for the particular link scenario. Nevertheless, linearity should be one of the main figures of merit when designing RRMs for high-speed SSB signal generation and fiber transmission. In the SOA, FWM further reduces the SSR by 11 dB at 2 GHz, because of the high power at its input and partial saturation of the amplifier. Therefore, it would be beneficial, if not necessary to use EDFAs for signal amplification in high-speed SSB-OFDM links.

Furthermore, according to Equation 3.17, higher tuning efficiency of the modulator would increase the SNR dictated by the phase-to-intensity converted noise. To this end, higher doping can be used to boost the tuning efficiency. This was, however, not available in the used MPW process which had a fixed doping profile. The doping could, nevertheless, be utilized as an additional degree of freedom in future RRM designs. The same equation indicates that the improvement in the SNR could also be achieved with a higher drive voltage. However, this would also exacerbate SNR reduction that originates from RRM nonlinearity.

On the receiver side, we studied a ten-channel WDM system that handles polarization scrambling in SMF links. Each channel consists of a double-sided OADM and double-sided Ge photodiode that enable simultaneous filtering and detection of

both orthogonal polarization states. Moreover, on-chip ODLs are employed to eliminate the detrimental group delay between the two signals. All ten channels achieve 28 Gb/s in a polarization-diverse configuration, with no notable signal degradation when compared to the single-polarization reference experiments. The maximum achievable speed is limited here by the bandwidth of the devices that comprise the system and not by the path imbalance between the two polarizations.

Appendix A

More on derivation of Equations 3.12 and 3.13

Here we present step-by-step derivations of Equations 3.12 and 3.13, which give expressions for the variance of the phase to intensity converted noise at the resonator output.

First, we detail the derivation of the variance of the phase error $\sigma^2_{\delta\theta}$. It is given as follows

$$\begin{aligned}
\sigma^2_{\delta\theta} &= \int_0^\infty \left[Re\left\{-e^{-t/\tau_a - i(\omega-\omega_0)t}\right\}\right]^2 2\pi\Delta\nu dt \\
&= 2\pi\Delta\nu \cdot \int_0^\infty e^{-2t/\tau_a} cos^2\left((\omega-\omega_0)t\right) dt \\
&= 2\pi\Delta\nu \cdot \int_0^\infty e^{-2t/\tau_a} \frac{1+cos\left(2\cdot(\omega-\omega_0)t\right)}{2} dt \\
&= \pi\Delta\nu \cdot \int_0^\infty e^{-2t/\tau_a} dt + \pi\Delta\nu \cdot Re\left\{\int_0^\infty e^{-2t/\tau_a + 2(\omega-\omega_0)t} dt\right\} \\
&= 2\pi\Delta\nu \cdot \frac{\tau_a}{4} + 2\pi\Delta\nu \cdot \frac{1}{2} Re\left\{\frac{1}{2/\tau_a - i2(\omega-\omega_0)}\right\} \\
&= 2\pi\Delta\nu \cdot \frac{\tau_a}{4} + 2\pi\Delta\nu \cdot \frac{1}{4} Re\left\{\frac{\tau_a}{1+\tau_a^2(\omega-\omega_0)^2} + i\cdot\frac{\omega-\omega_0}{1+\tau_a^2(\omega-\omega_0)^2}\right\} \\
&= 2\pi\Delta\nu\frac{\tau_a}{4}\left(1+\frac{1}{1+\tau_a^2(\omega-\omega_0)^2}\right),
\end{aligned} \tag{A.1}$$

which is the final expression given in Equation 3.8.

In a similar fashion, by using appropriate trigonometric manipulations (i.e. $sin^2(x) = (1-cos(2x))/2$ and $sin(x)cos(x) = sin(2x)/2$) and Euler's identity for complex numbers (i.e. $cos(x) = Re\{exp(ix)\}$ and $sin(x) = Im\{exp(ix)\}$), the expressions for $\sigma^2_{\delta\eta}$ and $\sigma_{\delta\theta\delta\eta}$ can be easily derived.

Next, from Equation 3.11 we can express the intensity noise at the resonator output as

$$\delta I = -2Im\{T\}\delta\theta + 2\Big(Re\{T\}Re\{T-1\} + Im\{T\}^2\Big)\delta\eta. \tag{A.2}$$

Here, $\delta\theta$ and $\delta\eta$ are random variables marking the phase error and amplitude noise of the coupled-back field, respectively. Given the expression for the variance of the sum of two random variables X and Y

$$Var(aX + bY) = a^2 \cdot Var(X) + b^2 \cdot Var(Y) + 2ab \cdot Covar(X, Y), \tag{A.3}$$

where a and b are constants and $Var()$ and $Covar()$ mark the variance and the covariance of the variables, respectively, we readily arrive at the Equation 3.12

$$\begin{aligned}\sigma_{\delta I}^2 =& 4\Big[\big|Im\{T\}\big|^2\sigma_{\delta\theta}^2 \\ &+ \big|Re\{T\}Re\{T-1\} + Im\{T\}^2\big|^2\sigma_{\delta\eta}^2 \\ &- 2Im\{T\}\big(Re\{T\}Re\{T-1\} + Im\{T\}^2\big)\sigma_{\delta\theta\delta\eta}\Big].\end{aligned} \tag{A.4}$$

Furthermore, to start the derivation of the Equation 3.13 we first repeat here some of the equations we will need in the process, for better overview. Apart from the already listed ones for $\sigma_{\delta\theta}^2$ (Equation A.1) and $\sigma_{\delta I}^2$ (Equation A.4), we will also use the following expressions

$$\sigma_{\delta\eta}^2 = 2\pi\Delta\nu\frac{\tau_a}{4}\left(1 - \frac{1}{1+\tau_a^2(\omega-\omega_0)^2}\right). \tag{A.5}$$

$$\sigma_{\delta\theta\delta\eta} = 2\pi\Delta\nu\frac{\tau_a^2}{4}\frac{\omega-\omega_0}{1+\tau_a^2(\omega-\omega_0)^2}. \tag{A.6}$$

$$T = 1 - \frac{\mu^2\tau_a}{1+i(\omega-\omega_0)\tau_a} \tag{A.7}$$

We introduce substitutions for the normalized coupling strength ($\tilde{\mu}^2$) and the normalized detuning ($\Delta\tilde{\omega}$)

$$\tilde{\mu}^2 = \mu^2\tau_a \tag{A.8}$$

$$\Delta\tilde{\omega} = (\omega-\omega_0)\tau_a. \tag{A.9}$$

Using this, the previous expressions can be written as

$$\frac{\sigma_{\delta\theta}^2}{2\pi\Delta\nu\tau_a} = \frac{1}{4}\left(1 + \frac{1}{1+\Delta\tilde{\omega}^2}\right) = \frac{1}{4}\frac{2+\Delta\tilde{\omega}^2}{1+\Delta\tilde{\omega}^2} \tag{A.10}$$

$$\frac{\sigma_{\delta\eta}^2}{2\pi\Delta\nu\tau_a} = \frac{1}{4}\left(1 - \frac{1}{1+\tilde{\Delta\omega}^2}\right) = \frac{1}{4}\frac{\Delta\tilde{\omega}^2}{1+\Delta\tilde{\omega}^2} \tag{A.11}$$

$$\frac{\sigma_{\delta\eta}^2}{2\pi\Delta\nu\tau_a} = \frac{1}{4}\frac{\Delta\tilde{\omega}}{1+\Delta\tilde{\omega}^2} \tag{A.12}$$

$$T = 1 - \frac{\mu^2\tau_a}{1+\tau_a^2(\omega-\omega_0)^2} + i\cdot\frac{\mu^2\tau_a\cdot(\omega-\omega_0)\tau_a}{1+\tau_a^2(\omega-\omega_0)^2} \tag{A.13}$$

$$Re\{T\} = 1 - \frac{\tilde{\mu}^2}{1+\Delta\tilde{\omega}^2} = \frac{1+\Delta\tilde{\omega}^2-\tilde{\mu}^2}{1+\Delta\tilde{\omega}^2} \tag{A.14}$$

$$Im\{T\} = \frac{\tilde{\mu}^2\Delta\tilde{\omega}}{1+\Delta\tilde{\omega}^2} \tag{A.15}$$

Let us first simplify the term in parenthesis in the second and third row of Equation A.4

$$\begin{aligned} Re\{T\}Re\{T-1\} + Im\{T\}^2 &= -\frac{1+\Delta\tilde{\omega}^2-\tilde{\mu}^2}{1+\Delta\tilde{\omega}^2}\cdot\frac{\tilde{\mu}^2}{1+\Delta\tilde{\omega}^2} + \frac{\tilde{\mu}^4\Delta\tilde{\omega}^2}{\left(1+\Delta\tilde{\omega}^2\right)^2} \\ &= \frac{\tilde{\mu}^2\left(-1+\tilde{\mu}^2-\Delta\tilde{\omega}^2+\tilde{\mu}^2\Delta\tilde{\omega}^2\right)}{\left(1+\Delta\tilde{\omega}^2\right)^2} \\ &= \frac{\tilde{\mu}^2\left(\tilde{\mu}^2-1\right)\left(1+\Delta\tilde{\omega}^2\right)}{\left(1+\Delta\tilde{\omega}^2\right)^2} \\ &= \frac{\tilde{\mu}^2\left(\tilde{\mu}^2-1\right)}{1+\Delta\tilde{\omega}^2} \end{aligned} \tag{A.16}$$

Lastly, we apply these substitutions to the overall expression for the phase noise induced intensity noise variance at the resonator output

$$\frac{\sigma_{\delta I}^2}{2\pi\Delta\nu\tau_a} = \frac{\tilde{\mu}^4\Delta\tilde{\omega}^2}{\left(1+\Delta\tilde{\omega}^2\right)^2}\cdot\frac{2+\Delta\tilde{\omega}^2}{1+\Delta\tilde{\omega}^2} + \frac{\tilde{\mu}^4\left(\tilde{\mu}^2-1\right)^2}{\left(1+\Delta\tilde{\omega}^2\right)^2}\cdot\frac{\Delta\tilde{\omega}^2}{1+\Delta\tilde{\omega}^2} - 2\cdot\frac{\tilde{\mu}^2\Delta\tilde{\omega}}{1+\Delta\tilde{\omega}^2}\cdot\frac{\tilde{\mu}^2\left(\tilde{\mu}^2-1\right)}{1+\Delta\tilde{\omega}^2}\cdot\frac{\Delta\tilde{\omega}}{1+\Delta\tilde{\omega}^2} \tag{A.17}$$

$$\begin{aligned} \frac{\sigma_{\delta I}^2}{2\pi\Delta\nu\tau_a\frac{\tilde{\mu}^4\Delta\tilde{\omega}^2}{\left(1+\Delta\tilde{\omega}^2\right)^3}} &= 2+\Delta\tilde{\omega}^2+\tilde{\mu}^4-2\tilde{\mu}^2+1-2\tilde{\mu}^2+2 \\ &= 1+\Delta\tilde{\omega}^2+4-4\tilde{\mu}^2+\tilde{\mu}^4 \\ &= 1+\Delta\tilde{\omega}^2+\left(2-\tilde{\mu}^2\right)^2 \end{aligned} \tag{A.18}$$

$$\sigma_{\delta I}^2 = 2\pi\Delta\nu\tau_a\cdot\Delta\tilde{\omega}^2\cdot\tilde{\mu}^4\cdot\left[\frac{1}{\left(1+\Delta\tilde{\omega}^2\right)^2} + \frac{\left(2-\tilde{\mu}^2\right)^2}{\left(1+\Delta\tilde{\omega}^2\right)^3}\right] \tag{A.19}$$

Substituting back for $\tilde{\mu}$ and $\Delta\tilde{\omega}$ leads us finally to the closed-form expression of Equation 3.13.

$$\sigma_{\delta I}^2 = 2\pi\Delta\tau_a \cdot (\omega-\omega_0)^2\tau_a^2 \cdot \mu^4\tau_a^2 \cdot \left[\frac{1}{\left(1+(\omega-\omega_0)^2\tau_a^2\right)^2} + \frac{(2-\mu^2\tau_a)^2}{\left(1+(\omega-\omega_0)^2\tau_a^2\right)^3}\right]. \tag{A.20}$$

Bibliography

[1] *Cisco annual internet report (2018-2023)*, 2020. [Online]. Available: https://www.cisco.com/c/en/us/solutions/collateral/executive-perspectives/annual-internet-report/white-paper-c11-741490.pdf.

[2] J. Hecht. "Future photonics: 5g—optics will be indispensable for 5g networks." (2020), [Online]. Available: https://www.laserfocusworld.com/fiber-optics/article/14074687/optics-will-be-indispensable-for-5g-networks.

[3] GSMA. "Mobile backhaul: An overview." (2019), [Online]. Available: https://www.gsma.com/futurenetworks/wiki/mobile-backhaul-an-overview/.

[4] Ericsson, Lumentum, S. Electric, Nokia, and II-VI. "Mobile optical pluggables (mopa)." (2021), [Online]. Available: https://resource.lumentum.com/s3fs-public/technical-library-items/mopa_technical_paper.pdf?null=.

[5] J. Witzens, "High-speed silicon photonics modulators," *Proceedings of the IEEE*, vol. 106, no. 12, 2018.

[6] A. Rahim *et al.*, "Taking silicon photonics modulators to a higher performance level: State-of-the-art and a review of new technologies," *Advanced Photonics*, vol. 3, no. 2, pp. 1 –23, 2021.

[7] G. Dehlinger, S. Koester, J. Schaub, J. Chu, Q. Ouyang, and A. Grill, "High-speed germanium-on-soi lateral pin photodiodes," *IEEE Photonics Technology Letters*, vol. 16, no. 11, 2004.

[8] D. Benedikovic *et al.*, "High-speed germanium p-i-n avalanche photodetectors on silicon," in *Integrated Optics: Design, Devices, Systems and Applications VI*, International Society for Optics and Photonics, vol. 11775, SPIE, 2021.

[9] F. Horst, W. M. Green, S. Assefa, S. M. Shank, Y. A. Vlasov, and B. J. Offrein, "Cascaded mach-zehnder wavelength filters in silicon photonics for low loss and flat pass-band wdm (de-)multiplexing," *Opt. Express*, vol. 21, no. 10, 2013.

[10] T. Fukazawa, F. Ohno, and T. Baba, "Very compact arrayed-waveguide-grating demultiplexer using si photonic wire waveguides," *Japanese Journal of Applied Physics*, vol. 43, no. 5B, 2004.

[11] B. Little, S. Chu, H. Haus, J. Foresi, and J.-P. Laine, "Microring resonator channel dropping filters," *Journal of Lightwave Technology*, vol. 15, no. 6, 1997.

[12] Q. Deng, R. Zhang, L. Liu, X. Li, J. Michel, and Z. Zhou, "Athermal and cmos-compatible flat-topped silicon mach-zehnder filters," in *2016 IEEE 13th International Conference on Group IV Photonics (GFP)*, 2016, pp. 172–173.

[13] S. Romero-García, A. Moscoso-Mártir, J. Müller, B. Shen, F. Merget, and J. Witzens, "Wideband multi-stage crow filters with relaxed fabrication tolerances," *Opt. Express*, vol. 26, no. 4, pp. 4723–4737, 2018.

[14] M. R. Watts and H. A. Haus, "Integrated mode-evolution-based polarization rotators," *Opt. Lett.*, vol. 30, no. 2, 2005.

[15] D. Dai and J. E. Bowers, "Novel concept for ultracompact polarization splitter-rotator based on silicon nanowires," *Opt. Express*, vol. 19, no. 11, 2011.

[16] D. Taillaert, H. Chong, P. Borel, L. Frandsen, R. De La Rue, and R. Baets, "A compact two-dimensional grating coupler used as a polarization splitter," *IEEE Photonics Technology Letters*, vol. 15, no. 9, 2003.

[17] F. Van Laere, W. Bogaerts, P. Dumon, G. Roelkens, D. Van Thourhout, and R. Baets, "Focusing polarization diversity gratings for silicon-on-insulator integrated circuits," in *2008 5th IEEE International Conference on Group IV Photonics*, 2008.

[18] L. Carroll, D. Gerace, I. Cristiani, S. Menezo, and L. C. Andreani, "Broad parameter optimization of polarization-diversity 2d grating couplers for silicon photonics," *Opt. Express*, vol. 21, no. 18, 2013.

[19] T. Komljenovic, D. Huang, P. Pintus, M. A. Tran, M. L. Davenport, and J. E. Bowers, "Photonic integrated circuits using heterogeneous integration on silicon," *Proceedings of the IEEE*, vol. 106, no. 12, 2018.

[20] Y. Wang *et al.*, "Monolithic quantum-dot distributed feedback laser array on silicon," *Optica*, vol. 5, no. 5, 2018.

[21] H. Yu *et al.*, "400gbps fully integrated dr4 silicon photonics transmitter for data center applications," in *2020 Optical Fiber Communications Conference and Exhibition (OFC)*, 2020.

[22] B. Marzban, J. Nojić, D. Stange, D. Buca, and J. Witzens, "Design of a waveguide-coupled gesn disk laser," in *2020 IEEE Photonics Society Summer Topicals Meeting Series (SUM)*, 2020.

[23] O. Moutanabbir *et al.*, "Monolithic infrared silicon photonics: The rise of (si)gesn semiconductors," *Applied Physics Letters*, vol. 118, no. 11, 2021.

[24] R. Chopra. "Co-packaged optics and an open ecosystem." (2021), [Online]. Available: https://blogs.cisco.com/sp/co-packaged-optics-and-an-open-ecosystem.

[25] N. Margalit, C. Xiang, S. M. Bowers, A. Bjorlin, R. Blum, and J. E. Bowers, "Perspective on the future of silicon photonics and electronics," *Applied Physics Letters*, vol. 118, no. 22, 2021.

[26] Q. Xu, B. Schmidt, J. Shakya, and M. Lipson, "Cascaded silicon micro-ring modulators for wdm optical interconnection," *Opt. Express*, vol. 14, no. 20, 2006.

[27] L. Chen, C. R. Doerr, P. Dong, and Y. kai Chen, "Monolithic silicon chip with 10 modulator channels at 25 gbps and 100-ghz spacing," *Opt. Express*, vol. 19, no. 26, 2011.

[28] M. Pantouvaki *et al.*, "8×14gb/s si ring wdm modulator array with integrated tungsten heaters and ge monitor photodetectors," in *OFC 2014*, 2014.

[29] R. Ding *et al.*, "A compact low-power 320-gb/s wdm transmitter based on silicon microrings," *IEEE Photonics Journal*, vol. 6, no. 3, 2014.

[30] J. Müller *et al.*, "Silicon photonics wdm transmitter with single section semiconductor mode-locked laser," *Advanced Optical Technologies*, vol. 4, no. 2, 2015.

[31] A. Moscoso-Mártir *et al.*, "8-channel wdm silicon photonics transceiver with soa and semiconductor mode-locked laser," *Opt. Express*, vol. 26, no. 19, 2018.

[32] S. Pitris *et al.*, "A 400 gb/s o-band wdm (8×50 gb/s) silicon photonic ring modulator-based transceiver," in *2020 Optical Fiber Communications Conference and Exhibition (OFC)*, 2020, pp. 1–3.

[33] M. Moralis-Pegios *et al.*, "4-channel 200 gb/s wdm o-band silicon photonic transceiver sub-assembly," *Opt. Express*, vol. 28, no. 4, 2020.

[34] X. Guan, W. Shi, and L. A. Rusch, "Ultra-dense wavelength-division multiplexing with microring modulator," *Journal of Lightwave Technology*, vol. 39, no. 13, 2021.

[35] W. Shieh and I. Djordjevic, *OFDM for Optical Communications*. Burlington, MA 01803, USA: Academic Press, 2010.

[36] P. Chow, J. Cioffi, and J. Bingham, "A Practical Discrete Multitone Transceiver Loading Algorithm for Data Transmission over Spectrally Shaped Channels," *IEEE Transactions on Communications*, vol. 43, no. 2/3/4, 1995.

[37] Q. Yang, W. Shieh, and Y. Ma, "Bit and power loading for coherent optical ofdm," in *OECC/ACOFT 2008 - Joint Conference of the Opto-Electronics and Communications Conference and the Australian Conference on Optical Fibre Technology*, 2008.

[38] J. M. Tang, P. M. Lane, and K. A. Shore, "High-speed transmission of adaptively modulated optical ofdm signals over multimode fibers using directly modulated dfbs," *J. Lightwave Technol.*, vol. 24, no. 1, 2006.

[39] H. Bulow, F. Buchali, and A. Klekamp, "Electronic dispersion compensation," *Journal of Lightwave Technology*, vol. 26, no. 1, 2008.

[40] J. Armstrong, "OFDM for Optical Communications," *Journal of Lightwave Technology*, vol. 27, no. 3, 2009.

[41] R. W. Chang, "Synthesis of band-limited orthogonal signals for multichannel data transmission," *The Bell System Technical Journal*, vol. 45, no. 10, 1966.

[42] N. Jolley, H. Kee, P. Pickard, J. Tang, and K. Cordina, "Generation and propagation of a 1550 nm 10 gbit/s optical orthogonal frequency division multiplexed signal over 1000m of multimode fibre using a directly modulated dfb," in *OFC/NFOEC Technical Digest. Optical Fiber Communication Conference, 2005.*, vol. 5, 2005.

[43] S. Dimitrov, S. Sinanovic, and H. Haas, "Clipping noise in ofdm-based optical wireless communication systems," *IEEE Transactions on Communications*, vol. 60, no. 4, 2012.

[44] I. B. Djordjevic, "Ldpc-coded ofdm transmission over graded-index plastic optical fiber links," *IEEE Photonics Technology Letters*, vol. 19, no. 12, 2007.

[45] K. Muramoto, A. Inoue, and Y. Koike, "Noise and distortion reduction in ofdm radio-over-fiber link by graded-index plastic optical fiber," *IEEE Photonics Technology Letters*, vol. 32, no. 13, 2020.

[46] W. Shieh, H. Bao, and Y. Tang, "Coherent optical ofdm: Theory and design," *Opt. Express*, vol. 16, no. 2, 2008.

[47] X. Wu, C. Huang, K. Xu, C. Shu, and H. K. Tsang, "128-gb/s line rate ofdm signal modulation using an integrated silicon microring modulator," *IEEE Photonics Technology Letters*, vol. 28, no. 19, 2016.

[48] P. Dong, J. Lee, K. Kim, Y.-K. Chen, and C. Gui, "Ten-channel discrete multitone modulation using silicon microring modulator array," in *Optical Fiber Communication Conference*, Optical Society of America, 2016.

[49] C. Y. Wong *et al.*, "Silicon iq modulator for next-generation metro network," *Journal of Lightwave Technology*, vol. 34, no. 2, 2016.

[50] B. J. C. Schmidt, A. J. Lowery, and J. Armstrong, "Experimental Demonstrations of Electronic Dispersion Compensation for Long-Haul Transmission Using Direct-Detection OFDM," *Journal of Lightwave Technology*, vol. 26, no. 1, 2008.

[51] L. A. Rusch, X. Guan, M. Lyu, and W. Shi, "Silicon photonics for 5g communications," in *2020 IEEE Photonics Conference (IPC)*, 2020.

[52] M. Lyu, W. Shi, and L. A. Rusch, "Silicon photonics to add 5g rof services to pons employing carrier reuse," in *2020 Optical Fiber Communications Conference and Exhibition (OFC)*, 2020.

[53] X. Guan, R. Dubé-Demers, W. Shi, and L. A. Rusch, "Heterogeneous optical access networks: Enabling low-latency 5g services with a silicon photonic smart edge," *Journal of Lightwave Technology*, vol. 39, no. 8, 2021.

[54] Y. Tong, C.-W. Chow, G.-H. Chen, C.-W. Peng, C.-H. Yeh, and H. K. Tsang, "Integrated silicon photonics remote radio frontend (rrf) for single-sideband (ssb) millimeter-wave radio-over-fiber (rof) systems," *IEEE Photonics Journal*, vol. 11, no. 2, 2019.

[55] B.-M. Yu, J.-M. Lee, C. Mai, S. Lischke, L. Zimmermann, and W.-Y. Choi, "Single-chip si optical single-sideband modulator," *Photon. Res.*, vol. 6, no. 1, 2018.

[56] M. Lyu, Y. Xu, L. A. Rusch, and W. Shi, "Single-sideband ofdm transmission via a silicon microring iq modulator," *IEEE Photonics Technology Letters*, vol. 31, no. 2, 2019.

[57] X. Zhang, Z. Babar, P. Petropoulos, H. Haas, and L. Hanzo, "The evolution of optical ofdm," *IEEE Communications Surveys Tutorials*, vol. 23, no. 3, 2021.

[58] R. Soref and B. Bennett, "Electrooptical Effects in Silicon," *IEEE Journal of Quantum Electronics*, vol. QE-23, no. 1, 1987.

[59] L. Chrostowski and M. Hochberg, *Silicon Photonics Design*. University Printing House, Cambridge CB2 8BS, United Kingdom: Cambridge Academic Press, 2015.

[60] T. Baba, S. Akiyami, M. Imai, N. Hirayama, H. Takahashi, and T. Usuki, "Efficient 50-Gb/s silicon microring modulator based on forward-biased pin diodes," in *10th International Conference on Group IV Photonics*, 2013.

[61] Q. Xu, S. Manipatruni, B. Schmidt, J. Shakya, and M. Lipson, "12.5 Gbit/s carrier-injection-based silicon microring modulators," *Optics Express*, vol. 5, no. 2, 2007.

[62] J. Sun, R. Kumar, M. Sakib, J. B. Driscoll, H. Jayatilleka, and H. Rong, "A 128 gb/s pam4 silicon microring modulator with integrated thermo-optic resonance tuning," *Journal of Lightwave Technology*, vol. 37, no. 1, 2019.

[63] S. Abel *et al.*, "Large pockels effect in micro- and nanostructured barium titanate integrated on silicon," *Nature Materials*, vol. 18, no. 1, 2019.

[64] R. Li *et al.*, "High-speed low-chirp PAM-4 transmission based on push-pull silicon photonic microring modulators," *Optics Express*, vol. 25, no. 12, 2017.

[65] X. Wu, B. Guan, Q. Xu, C. Doerr, and L. Chen, "Low-chirp push-pull dual-ring modulator with 144 gb/s pam-4 data transmission," *Opt. Express*, vol. 28, no. 18, 2020.

[66] A. Moscoso-Mártir *et al.*, "Co-integration of a temperature tolerant low impedance resonantly enhanced silicon photonics modulator," in *2017 IEEE 14th International Conference on Group IV Photonics (GFP)*, 2017.

[67] J. Müller *et al.*, "Optical Peaking Enhancement in High-Speed Ring Modulators," *Scientific Reports*, vol. 4, no. 6310, 2014.

[68] L. Zhang, Y. Li, J.-Y. Yang, M. Song, R. G. Beausoleil, and A. E. Willner, "Silicon-Based Microring Resonator Modulators for Intensity Modulation," *IEEE Journal of Selected Topics in Quantum Electronics*, vol. 16, no. 1, 2010.

[69] J. Heebner, R. Grover, and T. Ibrahim, *Optical Microresonators: Theory, Fabrication, and Applications*. Springer Series in Optical Sciencies, 2008.

[70] S. S. Azadeh *et al.*, "Low Vπ Silicon photonics modulators with highly linear epitaxially grown phase shifters," *Optics Express*, vol. 23, no. 18, 2015.

[71] S. S. Azadeh, J. Nojić, A. Moscoso-Mártir, F. Merget, and J. Witzens, "Power-efficient lumped-element meandered silicon Mach-Zehnder modulators," in *Silicon Photonics XV*, International Society for Optics and Photonics, vol. 11285, SPIE, 2020.

[72] K. Padmaraju, D. F. Logan, J. J. Ackert, A. P. Knights, and K. Bergman, "Microring resonance stabilization using thermal dithering," in *2013 Optical Interconnects Conference*, 2013.

[73] S. A. T. Mashayekh, "Tuning and controlling optical tellecomunication channels based on ring resonator modulators," M.S. thesis, RWTH Aachen University, 2017.

[74] S. Romero-García *et al.*, "Passively biased resonantly enhanced silicon photonics modulator with high optical bandwidth," in *Silicon Photonics XII*, vol. 10108, SPIE, 2017.

[75] S. Romero-Garcia, A. Moscoso-Martir, S. S. Azadeh, J. Müller, B. Shen, and J. Witzens, "High-speed resonantly enhanced silicon photonics modulator with a large operating temperature range," *Optics Letters*, vol. 42, no. 1, 2017.

[76] S. Romero-García *et al.*, "Broadband, temperature tolerant and passively biased resonantly enhanced mach-zehnder modulators," in *2018 IEEE 13th Annual International Conference on Nano/Micro Engineered and Molecular Systems (NEMS)*, 2018.

[77] J.-D. Fischbach, "Design of robust directional coupler for photonic microring resonators," Bachelor's thesis, RWTH Aachen University, 2020.

[78] S. S. Azadeh, "Integrated silicon electro-optical modulators for data/telecom applications," Ph.D. dissertation, RWTH Aachen University, 2019.

[79] J. Nojić, S. S. Azadeh, J. Müller, F. Merget, and J. Witzens, "Fabrication tolerant high-speed SiP ring modulators and optical add-drop multiplexers for WDM applications," in *Silicon Photonics XV*, International Society for Optics and Photonics, vol. 11285, SPIE, 2020.

[80] W. R. McKinnon *et al.*, "Extracting coupling and loss coefficients from a ring resonator," *Optics Express*, vol. 17, no. 21, 2009.

[81] J. Nojić *et al.*, "Laser phase noise in ring resonator assisted direct detection data transmission," *IEEE Journal of Selected Topics in Quantum Electronics*, vol. 27, no. 3, 2021.

[82] J. Nojić, S. S. Azadeh, J. Müller, X. Sun, F. Merget, and J. Witzens, "Theoretical investigation of a si rrm assisted ssb-ofdm modulator operated with a semiconductor mll," in *2019 Conference on Lasers and Electro-Optics (CLEO)*, 2019.

[83] V. Vujicic, P. M. Anandarajah, R. Zhou, C. Browning, and L. P. Barry, "Performance investigation of im/dd compatible ssb-ofdm systems based on optical multicarrier sources," *IEEE Photonics Journal*, vol. 6, no. 5, 2014.

[84] C. Calò *et al.*, "Single-section quantum well mode-locked laser for 400 gb/s ssb-ofdm transmission," *Opt. Express*, vol. 23, no. 20, 2015.

[85] R. Rosales *et al.*, "High performance mode locking characteristics of single section quantum dash lasers," *Opt. Express*, vol. 20, no. 8, 2012.

[86] S. Yamamoto, N. Edagawa, H. Taga, Y. Yoshida, and H. Wakabayashi, "Analysis of laser phase noise to intensity noise conversion by chromatic dispersion in intensity modulation and direct detection optical-fiber transmission," *Journal of Lightwave Technology*, vol. 8, no. 11, 1990.

[87] T. Septon *et al.*, "Large linewidth reduction in semiconductor lasers based on atom-like gain material," *Optica*, vol. 6, no. 8, 2019.

[88] F. A. Gutiérrez *et al.*, "WDM Orthogonal Subcarrier Multiplexing Based on Mode-Locked Lasers," *Journal of Lightwave Technology*, vol. 35, no. 14, 2017.

[89] A. Moscoso-Martir, J. Müller, E. Islamova, F. Merget, and J. Witzens, "Calibrated Link Budger of a Silicon Photonics WDM Transceiver with SOA and Semiconductor Mode-Locked Laser," *Scientific Reports*, vol. 7, no. 1, 2017.

[90] R. Schmogrow *et al.*, "Error Vector Magnitude as a Performance Measure for Advanced Modulation Formats," *IEEE Photonics Technology Letters*, vol. 24, no. 1, 2012.

[91] M. J. Shin, Y. Ban, B.-M. Yu, J. Rhim, L. Zimmermann, and W.-Y. Choi, "Parametric characterization of self-heating in depletion-type si micro-ring modulators," *IEEE Journal of Selected Topics in Quantum Electronics*, vol. 22, no. 6, 2016.

[92] X. Zheng *et al.*, "Enhanced optical bistability from self-heating due to free carrier absorption in substrate removed silicon ring modulators," *Opt. Express*, vol. 20, no. 10, 2012.

[93] L. A. Coldren, S. W. Corzine, and M. L. Mašanović, *Diode Lasers and Photonic Integrated Circuits*. Hoboken, New Jersey: John Wiley and Sons, Inc., 2012.

[94] I. Fatadin, D. Ives, and M. Wicks, "Numerical Simulation of Intensity and Phase Noise From Extracted Parameters of CW DFB Lasers," *IEEE Journal of Quantum Electronics*, vol. 42, no. 9, 2006.

[95] C. H. Henry, "Theory of the Linewidth of Semiconductor Lasers," *IEEE Journal of Quantum Electronics*, vol. QE-18, no. 2, 1982.

[96] G. P. Agrawal and N. A. Olsson, "Self-Phase Modulation and Spectral Broadening of Optical Pulses in Semiconductor Laser Amplifiers," *IEEE Journal of Quantum Electronics*, vol. 25, no. 11, 1989.

[97] T. Xu *et al.*, "Equalization enhanced phase noise in Nyquist-spaced superchannel transmission systems using multi-channel digital back-propagation," *Scientific Reports*, vol. 5, no. 13990, 2015.

[98] B. Li, K. J. Larsen, D. Zibar, and I. T. Monroy, "Over 10 db net coding gain based on 20decision forward error correction in 100g optical communication systems," in *2011 37th European Conference and Exhibition on Optical Communication*, 2011.

[99] A. Maese-Novo *et al.*, "Wavelength independent multimode interference coupler," *Opt. Express*, vol. 21, no. 6, 2013.

[100] J. Nojic, D. Schoofs, S. S. Azadeh, F. Merget, and J. Witzens, "Polarization-diverse silicon photonics wdm receiver with a reduced number of oadms and balanced group delays," in *2020 Optical Fiber Communications Conference and Exhibition (OFC)*, 2020.

[101] D. Schoofs, "Characterization of a polarization-insensitive integrated high-speed silicon photonics receiver system," M.S. thesis, RWTH Aachen University, 2019.

[102] A. Mekis, A. Narasimha, and J. Witzens, "Method and system for integrated power combiners," pat. US9417466B2, 2011.

[103] C. R. Doerr and T. F. Taunay, "Silicon Photonics Core-, Wavelength-, and Polarization-Diversity Receiver," *IEEE Photonics Technology Letters*, vol. 23, no. 9, 2011.

[104] P. Dong, Y.-K. Chen, and L. L. Buhl, "Reconfigurable Four-Channel Polarization Diversity Silicon Photonics WDM Receiver," in *Optical Fiber Communication Conference*, 2015, W3A.2.

[105] R. Gatdula, K. Kim, A. Melikyan, Y.-K. Chen, and P. Dong, "Simultaneous four-channel thermal adaptation of polarization insensitive silicon photonics wdm receiver," *Opt. Express*, vol. 25, no. 22, 2017.

[106] A. H. K. Park, H. Shoman, M. Ma, S. Shekhar, and L. Chrostowski, "Ring resonator based polarization diversity WDM receiver," *Optics Express*, vol. 27, no. 5, 2019.

[107] B. Shen *et al.*, "Reconfigurable frequency-selective resonance splitting in chalcogenide microring resonators," *ACS Photonics*, vol. 7, no. 2, 2020.

List of publications

[22] B. Marzban, J. Nojić, D. Stange, D. Buca, and J. Witzens, "Design of a waveguide-coupled gesn disk laser," in *2020 IEEE Photonics Society Summer Topicals Meeting Series (SUM)*, 2020.

[31] A. Moscoso-Mártir *et al.*, "8-channel wdm silicon photonics transceiver with soa and semiconductor mode-locked laser," *Opt. Express*, vol. 26, no. 19, 2018.

[66] A. Moscoso-Mártir *et al.*, "Co-integration of a temperature tolerant low impedance resonantly enhanced silicon photonics modulator," in *2017 IEEE 14th International Conference on Group IV Photonics (GFP)*, 2017.

[71] S. S. Azadeh, J. Nojić, A. Moscoso-Mártir, F. Merget, and J. Witzens, "Power-efficient lumped-element meandered silicon Mach-Zehnder modulators," in *Silicon Photonics XV*, International Society for Optics and Photonics, vol. 11285, SPIE, 2020.

[74] S. Romero-García *et al.*, "Passively biased resonantly enhanced silicon photonics modulator with high optical bandwidth," in *Silicon Photonics XII*, vol. 10108, SPIE, 2017.

[76] S. Romero-García *et al.*, "Broadband, temperature tolerant and passively biased resonantly enhanced mach-zehnder modulators," in *2018 IEEE 13th Annual International Conference on Nano/Micro Engineered and Molecular Systems (NEMS)*, 2018.

[79] J. Nojić, S. S. Azadeh, J. Müller, F. Merget, and J. Witzens, "Fabrication tolerant high-speed SiP ring modulators and optical add-drop multiplexers for WDM applications," in *Silicon Photonics XV*, International Society for Optics and Photonics, vol. 11285, SPIE, 2020.

[81] J. Nojić *et al.*, "Laser phase noise in ring resonator assisted direct detection data transmission," *IEEE Journal of Selected Topics in Quantum Electronics*, vol. 27, no. 3, 2021.

[82] J. Nojić, S. S. Azadeh, J. Müller, X. Sun, F. Merget, and J. Witzens, "Theoretical investigation of a si rrm assisted ssb-ofdm modulator operated with a semiconductor mll," in *2019 Conference on Lasers and Electro-Optics (CLEO)*, 2019.

[100] J. Nojic, D. Schoofs, S. S. Azadeh, F. Merget, and J. Witzens, "Polarization-diverse silicon photonics wdm receiver with a reduced number of oadms and balanced group delays," in *2020 Optical Fiber Communications Conference and Exhibition (OFC)*, 2020.

[107] B. Shen *et al.*, "Reconfigurable frequency-selective resonance splitting in chalcogenide microring resonators," *ACS Photonics*, vol. 7, no. 2, 2020.